UPC - Universitat Politècnica de Catalunya

Doctoral Thesis

A versatile source of light-matter quantum states based on laser-cooled atoms

Author:
Pau Farrera Soler

Supervisor:
Prof. Dr. Hugues de Riedmatten

A thesis submitted in fulfilment of the requirements for the degree of Doctor of Philosophy

in the

QPSA - Quantum Photonics with Solids and Atoms Group
ICFO - The Institute of Photonic Sciences

June 2018

"How wonderful that we have met with a paradox. Now we have some hope of making progress."

Niels Bohr

Abstract

Quantum information is a fascinating field that studies situations in which information is encoded as quantum states. This encoding is affected by quantum physical effects (such as superposition or entanglement) and its study has led to exciting discoveries from both fundamental and applied perspectives. An interesting system within this field is a quantum light-matter interface, able to interface quantum states encoded in light and those encoded in matter. These systems can combine the long distance transmission advantage of photonic states with the storage and processing capabilities of matter states.

The main goal of this thesis was to develop a quantum light-matter interface able to distribute the photonic state to other interfaces based on different platforms. This versatility could open new possibilities that combine the advantages of the different platforms. In this thesis we studied the challenges to make these hybrid connections possible and we performed two examples of such connections.

Our quantum light-matter interface is based on a cloud of rubidium atoms that are laser-cooled in a magneto-optical trap. We operate the atomic system using the Duan-Lukin-Cirac-Zoller scheme in order to generate pairs consisting of a single photon and an atomic collective spin excitation (so-called spin-wave). Spin-waves can later be mapped efficiently into a second single photon, which allows for synchronization capabilities. We use this scheme to generate different types of quantum states, such as heralded on-demand single photons and photonic qubits, photon-photon correlated states, or entanglement between photonic and atomic qubits.

Firstly, we studied two capabilities needed in order to perform the mentioned hybrid connections: the frequency and temporal tunability of the photonic states. In the first one we studied the frequency conversion of the single photons paired with spin-waves in the atomic medium. We could

convert their wavelength from 780 nm to 1552 nm using a nonlinear crystal waveguide, while still showing quantum statistics of the field. In the second one we showed a temporal tunability of the single photons with durations ranging from around 10 ns to 10 μs. The studied statistics of the fields indicate that the photons are close to Fourier-transform-limited, allowing for photon bandwidth tunability.

In the third work we studied the generation of a light-matter entangled state in which the photonic state is encoded as a time-bin qubit. Two key ingredients enabled this experiment: a magnetic-field-induced atomic dephasing that allows to create spin-waves in two distinguishable temporal qubit modes, and largely imbalanced Mach-Zehnder interferometers that enabled the qubit analysis. Photonic time-bin encoding has the advantages of low decoherence in optical fibers and direct suitability for frequency conversion.

Finally, we took advantage of these studied capabilities in order to transfer photonic quantum states generated by our laser-cooled atomic system to two different types of light-matter interfaces. The first one was a laser-cooled rubidium cloud able to transfer single photons into Rydberg excitations. We showed that the quantum statistics of our photonic fields are preserved after the Rydberg storage, which represents a first step for future studies of quantum nonlinear effects using the long range Rydberg interaction. The second one was a crystal doped with praseodymium ions. In this work the photonic quantum state transfer happened between systems with different atomic species, being a truly hybrid example that was enabled by quantum frequency conversion.

These results show a quantum light-matter interface where the properties of the photonic states can be tuned for an optimal interaction with other matter platforms. The proof-of-principle photonic quantum state transfers to the Rydberg and doped-crystal systems open the way to study new experiments that combine advantages of different platforms.

Resum

La informació quàntica estudia situacions en les que la informació està codificada en estats quàntics. Aquesta codificació és afectada per efectes de la física quàntica (com ara superposició o entrellaçament) i el seu estudi ha portat a descobriments i noves aplicacions fascinants. Uns sistemes interessants dins d'aquest camp son les interfícies quàntiques de llum-matèria, les quals interconnecten estats quàntics codificats en llum i en matèria. Aquests sistemes combinen els avantatges dels estats fotònics (bona transmissió a llarga distància) amb els dels estats en matèria (bon emmagatzematge i processament).

L'objectiu principal de la tesis era desenvolupar una interfície llum-matèria quàntica que pogués distribuir l'estat fotònic a altres interfícies basades en altres plataformes. Aquesta versatilitat podria obrir noves possibilitats que combinen els avantatges de les diferents plataformes. En aquesta tesis hem estudiat les dificultats que apareixen en aquestes connexions híbrides i hem realitzat dos exemples d'aquestes connexions.

La nostra interfície llum-matèria quàntica està basada en un núvol d'àtoms de Rubidi que estan refredats en una trampa magneto-òptica. Operem aquest sistema atòmic utilitzant l'esquema Duan-Lukin-Cirac-Zoller per tal de generar parelles que consisteixen en un fotó individual i una excitació atòmica d'espín col·lectiva (anomenada ona-d'espín). Nosaltres utilitzem aquest esquema per tal de generar diferents tipus d'estats quàntics, com ara fotons individuals o qubits fotònics, estats correlacionats de fotó-fotó o entrellaçament entre qubits fotònics i atòmics.

Primerament vam estudiar dues capacitats que es necessiten per tal de fer possible les connexions híbrides mencionades: la flexibilitat de la freqüència i el perfil temporal dels estats fotònics. En el primer vam estudiar la conversió de la freqüència dels fotons individuals aparellats amb ones-d'espín en el medi atòmic. Vam poder convertir la seva longitud d'ona de 780 nm a 1552 nm utilitzant una guia d'ones amb un cristall no-lineal. En el segon

vam mostrar la flexibilitat en la duració temporal de fotons individuals amb duracions que van de 10 ns a 10 μs. Les propietats estudiades dels fotons indiquen que el seu espectre està limitat per la transformada de Fourier, la qual cosa permet la flexibilitat del seu espectre.

En el tercer treball vam estudiar la generació d'un estat entrellaçat entre llum i matèria en el que l'estat fotònic està codificat en un time-bin qubit. Dos ingredients claus van permetre aquest experiment: un desfasament atòmic induït per un camp magnètic que permet crear ones-d'esín en dos modes temporals distingibles, i interferòmetres de Mach-Zehnder que van permetre l'anàlisi dels qubits. La codificació fotònica de time-bin té els avantatges de baixa decoherència en fibres òptiques i una compatibilitat directa per efectuar conversió de freqüència.

Finalment, vam aprofitar aquestes capacitats estudiades per tal de transferir estats quàntics fotònics cap a dos tipus diferents d'interfícies llum-matèria. La primera va ser una altre núvol fred d'àtoms de Rubidi en el que és possible transferir fotons individuals cap a excitacions de Rydberg. Aquest experiment representa el primer pas per a futurs estudis d'efectes quàntics no-lineals utilitzant les interaccions Rydberg de llarga distància. Els segon va ser un cristall dopat amb ions de Praseodimi. En aquest treball la transferència de l'estat quàntic va passar entre sistemes amb diferents espècies atòmiques, sent un veritable exemple híbrid fet possible per la conversió de freqüència quàntica.

Aquests resultats mostren una interfície llum-matèria quàntica en la que les propietats dels estats fotònics poden ser optimitzades per obtenir una interacció òptima amb altres plataformes materials. Les transferències fotòniques d'estats quàntics als sistemes de Rydberg i de cristalls obren la porta a l'estudi de nous experiments que combinin els avantatges de les diferents plataformes.

Acknowledgements

I would like to start by thanking my thesis supervisor Hugues, for starting such interesting scientific projects in Barcelona and giving me the opportunity to join them. His wise guiding, teaching, support and promotion of a very nice atmosphere in the group, have been priceless to reach this thesis culminating point.

Secondly I would like to thank Georg, who has been involved in all the projects described in the thesis and is the person with whom I spent the most time working. He is surely the person from whom I learnt the most in the group and it was a great privilege to work all this long time with him.

The next persons I want to thank are Boris and Matteo. They started with the project some years before I joined it and taught me really a lot. The start of the PhD can be a tough time in some situations, but this was not my case. This is thanks to their patient teachings and explanations, and also to their amazing job in the design and initial years of the project.

I would also like to thank Lukas, who became in charge of the experiment when I started writing the thesis. He brought new motivation and ideas to the project and I am very happy to see that the next challenges of the project will be in very good hands.

During my PhD I had the opportunity to collaborate with many people inside and outside the group. It was exciting to work with The Rydberg team (Emanuele, Auxi and David) and we had many nice experiences and interesting conversations while sharing the lab. With Nicolas we worked together in two experiments, and it was also nice to share the office. One of these experiments was done together with Kutlu and Margherita, and was a big pleasure to combine our setups for such an interesting project. Outside ICFO we did a very nice collaboration with the theory group of Prof. Nicolas Sangouard. I also want to thank the rest of the people involved

(Melvyn, Matías and Colin) for their enthusiasm and effort in bringing the collaboration to a successful point. It was also a very interesting experience to be part of the Big Bell Test collaboration led by Prof. Morgan Mitchell and Carlos Abellan.

I also want to thank all the present and former group members with whom I had the privilege to share lunches, dinners, group meetings, football matches, volleyball matches, hikes and other events. The present members that I still did not mention Alessandro, Bernardo, Darío, Chetan, Dario, Céline and the past members Mustafa, Patrick, Daniel, Andreas, Marco, Joachim, Chiara, Julia, all contributing to the very nice atmosphere in the group. This made our daily work life very pleasant and also enabled a nice and productive exchange of ideas.

At ICFO we have the privilege to be surrounded by many people who support us in order that we can focus on the purely scientific research work as much as possible. The support of the electronic and mechanical workshops were key to find fast and smart solutions to our mechanical and electronic challenges. The human resources, purchasing or travel departments made the bureaucracy part of our projects extremely easy. The efficient working of theses departments is thanks to the people working there but also thanks to the direction and academic boards for their wise and perfectionist leading.

I also want to thank Prof. Gerherd Rempe and Stephan Ritter from the Quantum Dynamics Division at MPQ for hosting me some weeks during the PhD. It was very motivating and interesting to join and learn from the research projects of Bastian, Stephan, Manuel, Dominik and Joseph.

The support of the International PhD-fellowship program "la Caixa"-Severo Ochoa @ ICFO was also very important. I want to thank the program for supporting young scientists as me.

Finally I would like to thank my friends, my family and anyone else whose positive impact on me contributed to reach this thesis culminating point.

List of publications

1. Pau Farrera*, Nicolas Maring*, Boris Albrecht, Georg Heinze and Hugues de Riedmatten, *Nonclassical correlations between a C-band telecom photon and a stored spin-wave*, Optica, 3(9), 1019–1024 (2016) (Chapter 3).

2. Pau Farrera, Georg Heinze, Boris Albrecht, Melvyn Ho, Matías Chávez, Colin Teo, Nicolas Sangouard and Hugues de Riedmatten, *Generation of single photons with highly tunable wave shape from a cold atomic ensemble*, Nature Communications, 7, 13556 (2016) (Chapter 4).

3. Pau Farrera, Georg Heinze and Hugues de Riedmatten, *Entanglement between a photonic time-bin qubit and a collective atomic spin excitation*, Physical Review Letters, 120, 100501 (2018) (Chapter 5).

4. Emanuele Distante*, Pau Farrera*, Auxiliadora Padrón-Brito, David Paredes-Barato, Georg Heinze and Hugues de Riedmatten, *Storing single photons emitted by a quantum memory on a highly excited Rydberg state*, Nature Communications, 8, 14072 (2017) (Chapter 6).

5. Nicolas Maring, Pau Farrera, Kutlu Kutluer, Georg Heinze, Margherita Mazzera and Hugues de Riedmatten, *Photonic quantum state transfer between a cold atomic gas and a crystal*, Nature, 551(7681), 485–488 (2017) (Chapter 6).

Publications not included in this thesis:

6. Boris Albrecht, Pau Farrera, Xavier Fernandez-Gonzalvo, Matteo Cristiani and Hugues de Riedmatten, *A waveguide frequency converter connecting rubidium-based quantum memories to the telecom C-band*, Nature Communications, 5, 3376 (2014)

7. Boris Albrecht, Pau Farrera, Georg Heinze, Matteo Cristiani, and Hugues de Riedmatten, *Controlled rephasing of single collective spin excitations in a cold atomic quantum memory*, Physical Review Letters, 115(16), 160501 (2015)

8. The BIG Bell Test Collaboration, *Challenging local realism with human choices*, Nature, 557(7704), 212-216 (2018)

* Equal contribution to the work

Table of Contents

Abbreviations

AOM	**A**cousto-**O**ptic **M**odulator
APD	**A**valanche **P**hoto**D**etector
DFG	**D**ifference **F**requency **G**eneration
DLCZ	**D**uan **L**ukin **C**irac **Z**oller
FWM	**F**our **W**ave **M**ixing
FSR	**F**ree **S**pectral **R**ange
FWHM	**F**ull **W**idth **H**alf **M**aximum
MOT	**M**agneto-**O**ptical **T**rap
PPLN	**P**eriodically **P**oled **L**ithium **N**iobate
QFC	**Q**uantum **F**requency **C**onversion
QFCD	**Q**uantum **F**requency **C**onversion **D**evice
QM	**Q**uantum **M**emory
SNR	**S**ignal-to-**N**oise **R**atio
SPD	**S**ingle **P**hoton **D**etector

Chapter 1

Introduction

1.1 Quantum physics and quantum information

Quantum physics emerged around one century ago to describe some non-intuitive phenomena that happen in the regime of small scales and low energies. The development of this theory started with the quantization of the electromagnetic field proposed by Max Planck, which allowed him to theoretically describe the black body radiation spectrum. The field followed with the study of other effects that differ from "classical physics", such as the introduction of the energy and momentum quantization in the atomic model, the fact that physical entities have properties of both particles and waves (wave-particle duality), or the fundamental precision limits in the knowledge of some quantities (Heisenberg uncertainty limit).

Apart from the huge fundamental interest of all these non-intuitive phenomena, their study also enabled the development of technologies that currently have a tremendous impact in our society. Two of the most prominent examples are semiconductors (used for example in the form of transistors in

computing devices) or lasers (with a vast range of applications in medicine, material processing or metrology).

One fascinating field within quantum physics is quantum information. This field aims at studying the interesting effects that happen when information is encoded in elementary entities such as photons or electrons. Some of these effects include quantum superposition, entanglement or teleportation, and apart from their huge fundamental interest, they could also enable the rise of new technologies such as quantum cryptography [1], computation [2], simulation [3] and metrology [4].

There is currently a lot of research taking place in the field of quantum information, and there are many different platforms used for both fundamental experiments and the development of applications. Quantum states can be encoded in light fields such as single photons, or matter platforms such as atomic gasses, crystals, single atoms or superconducting circuits. Each platform is usually particularly good for specific quantum information tasks. In this context quantum light-matter interfaces are very interesting systems, since they can combine the individual advantages offered by quantum states encoded in light and those encoded in matter platforms.

1.2 Quantum light-matter interfaces

Quantum light-matter interfaces are systems in which quantum states encoded in light and those encoded in matter can be connected. Apart from the fascinating physics that one can study in these interfaces, they also have a more practical interest. They can be used to combine the advantages of photonic and matter quantum states, which are mainly the following:

Photonic (flying) quantum states: Since light can travel long distances in a fast and costless way (either through free space or optical fibers), encoding quantum states in light is very suitable for their remote distribution. This is beneficial for both long distance quantum communication (with potential use in quantum key distribution or remote quantum computing), or just to distribute quantum states along different systems in a laboratory for fundamental science purposes.

Matter (stationary) quantum states: There are two main advantages of storing quantum states in matter systems. (1) With the proper control of decoherence effects, the lifetime of the quantum states can be extended to very long times. This allows both long term storage and synchronization capabilities. (2) Certain matter systems exhibit a strong and tunable interaction between the particles in which the states are encoded. This interaction can be used for the processing of the quantum states (e.g. to build multi-qubit quantum gates).

The combination of photonic and matter quantum states allows to combine the mentioned advantages of each system, which is important in many situations. Some of these include the synchronization of photonic quantum states, the connection of eventual future quantum computers or situations of remote quantum metrology (such as a quantum network of clocks [5]).

1.2.1 Different platforms

In the recent decades there are several platforms that have been investigated as quantum light-matter interfaces. Each of them offers certain advantages and peculiarities and some of the most studied ones are listed in Fig. 1.1. They are here classified according to two relevant characteristics: (1) whether they consist of a single emitter or an atomic ensemble,

and (2) whether they are surrounded by a free environment or a solid state one. In the next paragraphs we compare the advantages and disadvantages of the different platforms according to these characteristics.

	Single emitters	Atomic ensembles
Free environment	Single neutral atoms Single ions	Warm atomic vapours Laser cooled atomic gases
Solid state environment	Quantum dots Defects in diamond	Rare-earth-ion doped crystals

FIGURE 1.1: Table listing different types of quantum light-matter interfaces. They are classified according to the characteristics that are mentioned in the coloured boxes.

Single emitters vs atomic ensembles

Single emitters are very good at generating deterministically single photons as their name indicates. They also can store quantum states using internal degrees of freedom, which are easy to manipulate using electromagnetic radiation. In order to interact efficiently with light they need to be surrounded by high finesse cavities, which is experimentally challenging. If the photon-atom interaction is strong, single emitters can act as quantum nonlinear systems and mediate photon-photon interactions [6]. One can see this considering that a single atom cannot absorb or emit more than one photon at a given time, which means that the absorption of a photon drastically changes the atom's response to a second arriving photon.

Atomic ensembles can couple efficiently with light without the need of optical cavities. They can store photonic quantum states in the form of collective atomic excitations, which can be later mapped back to photons very efficiently. However, manipulating these collective excitations is more challenging, since all the atoms forming the collective state have to be manipulated in the same way. Atomic ensembles can also be used to mediate

photon-photon interactions. One way to do this is to map the photons into atomic excitations with high principal quantum number (Rydberg excitations). The strong long-range interaction between two Rydberg atoms can then be used to mediate the quantum nonlinear optical response.

Free vs solid state environment

Having atoms in a free environment has the advantage that in this situation there are typically no decoherence mechanisms related to phonons or other interactions of the atoms with the surrounding medium. However since they are free they can move and change position, which can be a source of decoherence. This means that one typically has to cool and control their motion in order to have long coherence times.

In solid state devices the optically active atoms are typically fixed on the crystal lattice, and therefore there are no problems related to the atomic motion. However one has to carefully consider decoherence mechanisms related to phonon interaction and other types of interactions between the optically active atoms and the surrounding.

In order to have long coherence time these systems are sometimes cooled. Cooling atoms in a free environment can be done using laser cooling. This technique allows one to cool down to few tens of μK with standard techniques and to the nK range with further evaporative cooling. The cooling process affects the internal electronic state of the atoms and therefore sometimes one has to alternate the operation of the system with the cooling stages. In order to prepare the atoms in the desired state after each cooling stage, one can use optical pumping.

Cooling solid states systems requires a cryostat. These devices are commercially available reaching temperatures of around few degrees above the

absolute zero for standard cryostats or few tens of mK for dilution fridges. In theory the cryogenic cooling does not affect the operation of the system, but in practice one has to consider that these cooling devices may induce vibrations to the system.

1.2.2 Optical quantum memories

Photonic quantum memories are one type of quantum light-matter interfaces. They are systems able to store (and later retrieve) quantum states encoded in photonic modes. They offer the possibility of long term storage or synchronization of quantum states encoded in light. According to their basic operation, there are two kinds of optical quantum memories: the read-write type and the read-only one [7].

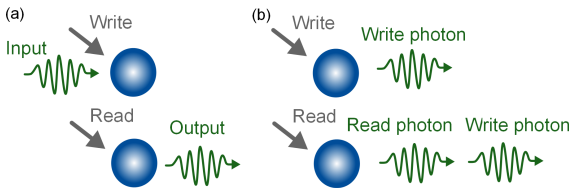

FIGURE 1.2: Schematic representation of the read-write (a) and the read-only (b) types of optical quantum memories.

Read-write memory: In this kind of memory an input quantum state encoded in light is "written" into a matter system. It is then stored in the system encoded in some internal degree of freedom of the atoms. Some time after the writing process one can map back the quantum state into another photonic field in what is called the reading process. This type of memory is sometimes also called "absorptive memory".

Read-only memory: In this kind of memory there is no input photonic quantum state. In this case the memory starts with a write process in which the system generates an entangled state between an emitted single

photon and a matter internal degree of freedom. This matter component of the entangled state can be stored for some time before being released in the read process encoded into another single photon. Read-only memories are particularly interesting for situations that require synchronized operations with entangled states, such as quantum repeaters. This type of memory is sometimes also called "emissive memory".

1.2.3 Quantum repeaters

One particular application that the synchronization of photonic quantum states using quantum memories could enable is quantum repeaters [8, 9]. The aim of these repeater architectures is to distribute quantum states over very long distances. Currently the best way to do this is to encode quantum states in single photons and distribute them through optical channels (e.g. optical fibres [10] or free space [11]). However, since the photon transmission decreases exponentially with the distance, this approach limits the distribution distance to a few hundreds of kilometres. To overcome this problem the concept of a quantum repeater was proposed. A simple schematic drawing of the idea behind this concept is shown in Fig. 1.3 (a) and (b). A one dimensional array of quantum nodes covers the distribution distance with the goal of entangling the two outer nodes. In this situation ones starts by creating entanglement between all the pairs of neighbouring nodes. Once two pairs of neighbouring nodes have been entangled, this entanglement can be extended to the outer nodes of the group by means of entanglement swapping operations. This process can be iterated until the outer nodes of the array are successfully entangled. Because of photon losses and other technical imperfections, the entanglement generation

within each elementary link is probabilistic and does not happen simultaneously for all the links. Therefore it is important to store the entangled states until adjacent links get entangled, which is the reason that the nodes should be quantum memories.

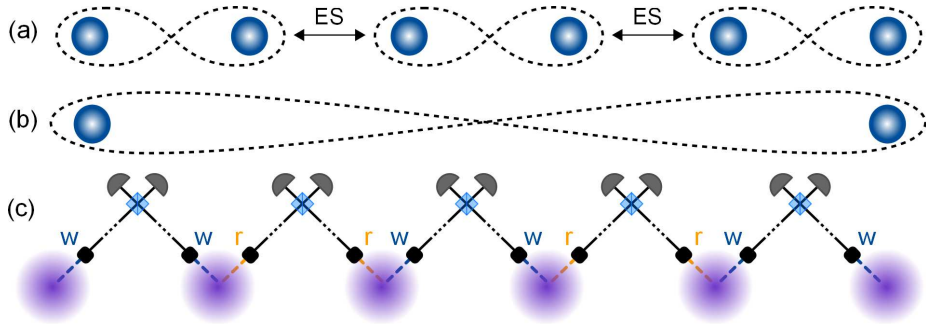

FIGURE 1.3: (a) Schematic drawing describing the basic idea of a quantum repeater architecture. The ∞-shaped dashed curves represent the entanglement between nodes, which is initially generated between neighbouring ones. Using entanglement swapping (ES) operations, the entanglement can be extended to the two outer distant nodes as represented in (b). (c) Schematic description of the DLCZ quantum repeater protocol. It is based on the use of atomic ensembles, beam splitters and single photon detectors for the entanglement generation, storage and swapping operations. w denotes the write photons and r the read photons.

The advantage when using such a repeater architecture is that the quantum state distribution time scales polynomially with the distance, instead of the exponential scaling of direct transmission. This comes however together with one main drawback: the errors and losses that will happen in the entanglement generation, storage and swapping operations. This issue is the main challenge to transform quantum repeaters from a theoretical proposal to an experimentally feasible implementation. The realisation of a quantum repeater would make quantum state transfer feasible to a much longer distance than it is now possible. The first theoretical proposal for a practical implementation of a quantum repeater was done by L.M. Duan, M. Lukin, J.I. Cirac and P. Zoller in [12] and is commonly referred as the DLCZ scheme. This is explained in the next section.

1.2.4 The DLCZ scheme

The Duan-Lukin-Cirac-Zoller (DLCZ) scheme was originally proposed as a practical implementation of a quantum repeater for creating long distance entanglement. The idea is to create long lived spin excitations in an atomic ensemble correlated with single "write" photons. Combining the write photonic modes generated by two different ensembles at a beam-splitter, allows the creation of entanglement between two atomic ensembles. This entangled state could be stored for some time encoded in the long lived spin excitations, which can be later converted into "read" photons once two neighbouring pairs of nodes are successfully entangled. Combining these read photon modes in another beam splitter allows the entanglement swapping operation. This repeater architecture is schematically represented in Fig. 1.3c.

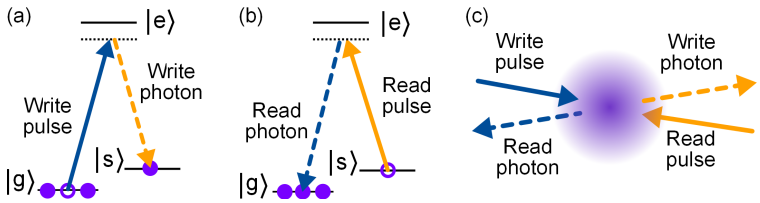

FIGURE 1.4: Schematic representation of the DLCZ scheme. (a) Write process in which a write pulse generates probabilistically a write photon correlated with a spin-wave. (b) Read process in which a read pulse converts the spin excitation into a single read photon. (c) Possible spatial configuration of the light fields involved in the DLCZ scheme.

The schematic description of how a DLCZ node works can be seen in Fig. 1.4. The scheme requires an ensemble of atoms that exhibits a Λ level scheme with two metastable ground states ($|g\rangle$ and $|s\rangle$) and one excited state $|e\rangle$. The operation starts with a "write" pulse that is off-resonant with the $|g\rangle \rightarrow |e\rangle$ transition and interacts with the ensemble of atoms, that is initially optically pumped in state $|g\rangle$ (see Fig. 1.4a). This process can generate, through spontaneous Raman scattering, single photons on

the $|e\rangle \rightarrow |s\rangle$ transition (so-called write photons). In this situations the write photons are correlated with atomic spin excitations (e.g. atoms in $|s\rangle$). Since the write pulse and photon modes interact with many atoms from the ensemble, the excitation is collective. This means that this conditional state can be represented by a quantum superposition involving many atoms, one of them being excited, with the form

$$|\Psi_{\mathrm{a}}\rangle = \frac{1}{N}\sum_{j=1}^{N} e^{i(\mathbf{k}_{\mathrm{W}}-\mathbf{k}_{\mathrm{w}})\cdot\mathbf{r}_j}\,|g_1 \ldots s_j \ldots g_N\rangle \tag{1.1}$$

where N is the number of atoms involved in the process, $\mathbf{k}_{\mathrm{W(w)}}$ is the wavevector of the write pulse (photon) mode and $\mathbf{r}_j$ is the position of the atom that is excited. This collective spin excitation is also commonly called "spin-wave".

After some time (usually called storage time) a "read" pulse couples resonantly the $|\mathrm{s}\rangle \rightarrow |\mathrm{e}\rangle$ transition (see Fig. 1.4b). If the phases of the state described by Eq. (1.1) are preserved during the storage time, then the read pulse converts the spin-wave into a single read photon that is emitted with a high read-out efficiency in a very well defined spatial mode given by the phase matching condition $\mathbf{k}_{\mathrm{r}} = \mathbf{k}_{\mathrm{W}} - \mathbf{k}_{\mathrm{w}} + \mathbf{k}_{\mathrm{R}}$. This directional emission comes from the collective behaviour of the process, which involves many atoms. This phenomena leads to the constructive interference in a particular direction of the read photon emission process. If the write and read pulses are counter-propagating and the spin-wave coherence is preserved, then the write and read photons are emitted in counter-propagating directions, as shown in Fig. 1.4c.

In the previous paragraphs we have focused on the emission of a single

write photon into the mode of interest. However, since there is an ensemble of atoms, there are also amplitudes for the emission of two or more write photons, accompanied by the creation of the same number of atomic excitations in $|\mathrm{s}\rangle$. This process can be described by the following Hamiltonian [9, 13]:

$$H = \chi(a_{\mathrm{w}}^{\dagger} s^{\dagger} + a_{\mathrm{w}} s) \tag{1.2}$$

where $a_{\mathrm{w}}^{\dagger}$ is the creation operator for a write photon, $s^{\dagger}$ the creation operator for a spin-wave and χ is a coupling constant that depends on the laser power and detuning of the write pulse, the transition strengths or the number of atoms. This Hamiltonian is formally equivalent to the one that describes the non-linear optical process of parametric down-conversion, except that here one of the modes is atomic. Starting from a vacuum state for both modes a_{w} and s, it can be calculated [9] that after and interaction time t this Hamiltonian creates the following two-mode state

$$|\Psi\rangle = \sqrt{1 - |\xi|^2} \left(\sum_{k=0}^{\infty} \xi^k \, |k_{\mathrm{w}}, k_{\mathrm{s}}\rangle \right) \tag{1.3}$$

where $\xi = -\mathrm{i}\tanh(\chi t)$ and $k_{\mathrm{w(s)}}$ denotes the number of write photons (spin-waves). The probability to create at least one pair of write photon and spin-wave is given by $p = |\xi|^2$, and it is typically tuned by changing the write pulse power. As it is explained in Appendix A and Appendix B the state described by Eq. (1.3) can lead to photonic non-classical statistics (i.e. statistics that can not be described by classical light fields).

To summarize, the DLCZ scheme is a method to generate atomic spin excitations paired with single photons, that can be latter mapped into another single photon in a well defined spatial mode. The careful manipulation of the photonic and atomic degrees of freedom allows for the generation of

entangled states between the write photon and the spin-wave (see subsection 1.3.1). Therefore, this type of system is an example of a read-only quantum memory (cf. subsection 1.2.2). These kind of sources can be used for instance as heralded on-demand single photon sources, quantum repeater nodes or synchronizable sources of entangled photon pairs.

1.3 Generation and distribution of atom-photon quantum states

Using the DLCZ scheme one can generate single photons which are correlated and/or entangled with long lived atomic spin excitations. These atom-photon quantum states open possibilities to distribute entanglement over remote matter systems or to generate on-demand single photons and photonic qubits. The DLCZ scheme with atomic ensembles is not the only approach that can be used to generate this kind of states. In this section I will talk about the state of the art experiments that generate similar states, the work that has been done using the DLCZ scheme, and the motivation for the new experiments that are described in this thesis.

1.3.1 State of the art

There are many systems that have been used to generate atom-photon quantum states. The generation of entanglement between a photon and an atomic excitation has been achieved in systems like single trapped ions and neutral atoms [14–16], laser-cooled atomic ensembles [17, 18], ion-doped crystals [19, 20], vacancy centres in diamond [21] or quantum dots [22, 23]. And the remote distribution of the photonic part of the state has enabled the realization of many interesting experiments. Some examples

are the distribution of entanglement over remote matter systems [24–29], the teleportation of matter quantum states [30–32], the demonstration of elementary links from a quantum repeater [33, 34], or closing Bell inequality loopholes [35, 36].

From a general prespective, quantum light-matter interfaces are now moving towards different directions. One goal is to increase the light-matter interaction by placing the systems around optical cavities [27, 37], or coupling them to nano-photonic systems [38–41]. Apart from increasing efficiencies, this enhancement of the light matter coupling can also enable atom-atom interactions mediated by photons [42] or vice-versa, photon-photon interactions mediated by atoms [43]. These photon-photon interactions are also being investigated using Rydberg atoms [44, 45]. Other interesting parameters of such systems that are being studied are the coherence time of the atomic excitations [46, 47], the operation bandwidth [48, 49], exploring the use of different photonic degrees of freedom [50, 51] or the operation at telecom wavelengths[52, 53]. Telecom frequencies are attractive because they exhibit a very low loss in optical fibers, and another way to reach this wavelength is by means of quantum frequency conversion [54–61].

Focusing on the DLCZ scheme, the first experimental demonstrations were performed in 2003 using a laser-cooled atomic ensemble in a magneto-optical trap (MOT) [62] and using an atomic vapour cell [63]. Since the initial experiments many techniques were developed to improve the coherence time of the atomic excitation or the conversion efficiency into a single read photon, among other aspects. The coherence time of the atomic excitation was improved from the original $\tau \approx 150\,\mathrm{ns}$ [64] to $\tau \approx 10\,\mu\mathrm{s}$ by switching off the MOT magnetic field [65]. Later it was extended to $\tau > 1\,\mathrm{ms}$ by using magnetic field insensitive transitions and reducing the

effect of atomic motion (either through an optical lattice [66] or using a collinear beam configuration [67]). And finally, by compensating the light shifts induced by the lattice beams it was possible to achieve $\tau > 100\,\mathrm{ms}$ [54, 68]. Other optical memory protocols managed to extend the storage lifetime to the minute regime by using the dynamical decoupling protocol [69, 70], but this was done with classical light states and has yet to be demonstrated with photonic quantum states. Regarding the emission efficiency of the read photon, it has been improved from the original works by surrounding the atomic ensembles by optical cavities [71–73]. This improvement led to intrinsic retrieval efficiencies of $p_{\mathrm{r|w}} > 80\,\%$. An alternative way would be to increase the optical depth as it has been studied in [74–76] for other optical memory protocols.

As mentioned in the previous section, the DLCZ scheme can be used to generate entanglement between light and matter. Several experiments have demonstrated this capability using different degrees of freedom for the photonic qubit. The degrees of freedom used so far are polarization [17, 18, 77], spatial mode [78] or orbital angular momentum [79].

Other remarkable advances of the DLCZ scheme include its combination with different multiplexing techniques [80–82], the frequency conversion of the generated photons to telecom frequencies [55, 57], or studying its implementation in systems different from laser-cooled atomic ensembles, such as warm atomic gases [83, 84], doped crystals [85, 86] and optomechanical systems [87].

1.3.2 Motivation for our work

As mentioned in the previous sections, there are currently many different types of quantum light-matter interfaces being investigated in different

research laboratories. In general it is difficult to say which system shows a better global performance than the other, because they all come with individual advantages. One of the central goals of this thesis was to develop and characterize a quantum light-matter interface capable to interconnect with other interfaces based on different types of matter systems. The motivation is that in this situation one could combine the advantages of the different platforms, which could lead to new interesting experiments and applications. Fig. 1.5 shows pictures and representations of different systems and our motivation to transfer quantum states from our laser-cooled atomic ensemble.

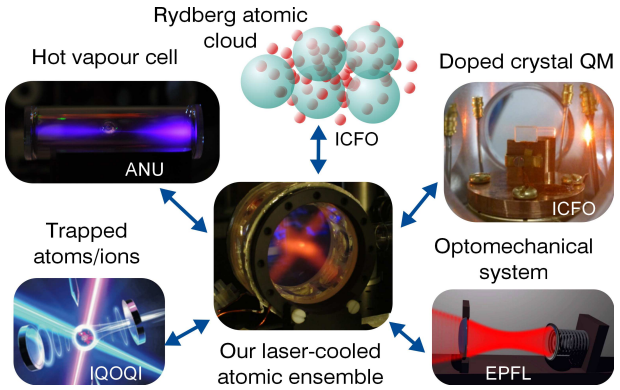

FIGURE 1.5: (a) Pictures and drawings representing different types of light-matter interfaces, and our goal to distribute to other systems photonic quantum states generated by our laser-cooled atomic ensemble.

The idea was to use a photonic channel to transfer quantum states between the different types of matter systems. In this situation there are two main challenges that need to be faced. (1) Typically different types of matter systems have an optimal interaction with light of different frequencies. (2) Apart form the light central frequency, its optical spectrum also has an important impact on the light-matter interaction efficiency. Spectral bandwidths that give the optimal operation can go from the GHz range in hot atomic vapours [49, 88] to below the 100 KHz range in the case

of trapped ions coupled to cavities [37]. Issue (1) is studied in chapter 3, where we study the frequency conversion of single photons using a nonlinear crystal waveguide. In particular we use the nonlinear process difference frequency generation (DFG) in a periodically poled crystal. Adjusting the frequency of the pump laser involved in the process and the poling period of the crystal, one can choose the frequency of the output photons. This allows us to translated the frequency of the single photons emitted by our laser-cooled atomic ensemble into the desired one.

In order to address issue (2) we studied the tunability of the temporal waveform of our generated single photons. The temporal width of any light pulse is inversely proportional to its spectral width, providing that the light pulse is Fourier-transform limited. For Gaussian-shaped light pulses the limit on the temporal Δt and spectral $\Delta\nu$ widths (considering the Full Width Half Maximum) is given by $\Delta t \Delta\nu = 0.44$. This motivated us to the study the limits in the temporal tunability of our photons, which is explained in chapter 4.

One type quantum states that are interesting to transfer between matter objects are entangled states. This motivated us to study the generation of entanglement between photons and collective excitations in our system, which is covered in chapter 5. In particular we studied the situation in which the photonic qubit is encoded in the time-bin degree of freedom, which has three main advantages. Firstly, it shows a low decoherence when being transmitted through optical fibers, and is therefore suitable for long distance transmission. Secondly, it is also suitable for standard frequency conversion, which would enable its distribution to different types of systems. And finally, it is naturally stored in quantum memories based

on rare-earth-ion doped crystals and the atomic frequency comb (AFC) protocol [89, 90].

After these studies we took advantage of these developed capabilities in order to transfer photonic quantum states between different types of matter systems. In particular we transferred photonic quantum states from our laser-cooled atoms to two different systems (see chapter 6): highly excited Rydberg excitations in another laser-cooled atomic system, and a crystal doped with praseodymium ions. Each of these two projects had a specific motivation. For the first experiment, we would like to use the strong and long range interaction between atoms with Rydberg excitations in order to mediate efficient photon-photon interactions. This capability would be very interesting in the context of quantum nonlinear optics and photonic quantum information processing. For the second experiment, the photonic quantum states transfer from our rubidium 87 atomic cloud to a praseodymium ion-doped crystal represents a demonstration of a photonic quantum link between hybrid and long lived light-matter interfaces. This type of hybrid connections could be used to combine advantages of light-matter interfaces implemented with different platforms.

Chapter 2

Experimental setup

The experiments performed during my PhD involved the combination of several devices and setups such as lasers, vacuum systems, photon filtering and detection setups or interferometers, among others. In this section I will describe the ones that are more relevant in the context of the experiments that we performed. Fig. 2.1 shows an overview of the optical table with the main part of the experiment.

The central part of the experiment was a trapped cloud of laser-cooled atoms inside a vacuum chamber. Laser light was used for different purposes: cooling, manipulating and preparing the atomic cloud or generating the atom-photon quantum states, among others. The single photons generated by the atoms were sent to optical filters that separate them from light noise, and measured by single photon detectors later. In some of the experiments the single photons were processed or analyzed by other devices, such as the quantum frequency converter or the Mach-Zehnder interferometers. The atom trap and laser system were mainly built by

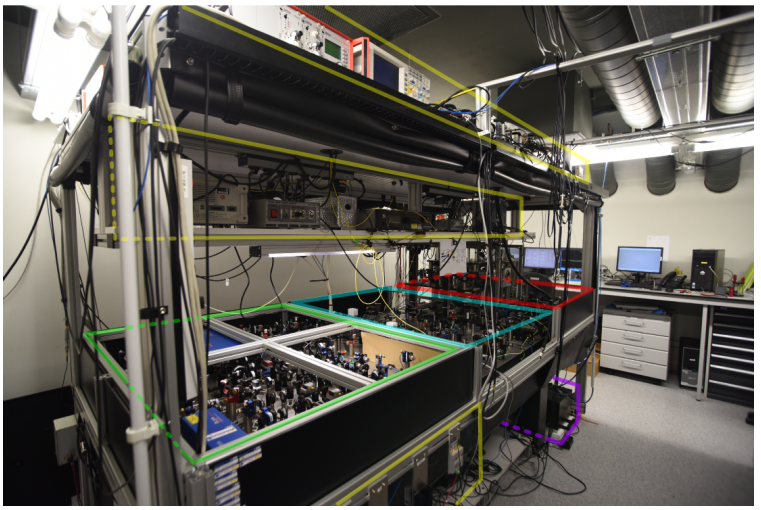

FIGURE 2.1: Picture showing the optical table where most of the experimental devices used during my PhD are installed. The green-line area represents the laser system section of the optical table, in the blue-line area we have the quantum frequency converter device and the filtering optical cavities, in the purple region we have the boxes that contain the Mach-Zehnder interferometers, the red-line area is the central part of the experiment with the magneto-optical trap, and the yellow-line area is mainly occupied by electronic devices.

previous PhD student Boris Albrecht together with research fellow Matteo Cristiani. The quantum frequency converter was mainly developped by master students Giacommo Corrielli and Xavier Fernandez, and PhD student Nicolas Maring. All the above mentioned devices are described in the following pages. A particularly detailed explanation is given for the description of the Mach-Zehnder interferometers, since this was the main part of the setup that was constructed and optimized as part of this thesis.

2.1 Laser systems

Our experiments rely on the interaction of atoms with light, and therefore the laser light preparation part of our experiment is very important. There

are two lasers that we typically use in the experiments, both addressing the transition of ^{87}Rb $5^2S_{1/2} \leftrightarrow 5^2P_{3/2}$ ($\lambda = 780.2\,\text{nm}$). Considering the nuclear spin of ^{87}Rb ($I = 3/2$), state $5^2S_{1/2}$ is splitted in the hyperfine levels with F=1 and F=2 (with $\Delta\nu = 6.83\,\text{GHz}$), and each laser couples the transitions given by each of these levels. The lasers are the models DL Pro and TA Pro from Toptica. Both are diode lasers with a grating stabilized external cavity. The difference between the two lasers is that for the TA Pro model, the output of the external cavity diode laser is amplified by a tapered amplifier diode. The DL Pro and TA Pro lasers can give ouput powers of around 0.1 W and 1.5 W respectively, and exhibit spectral linewidths of few hundreds of kHz.

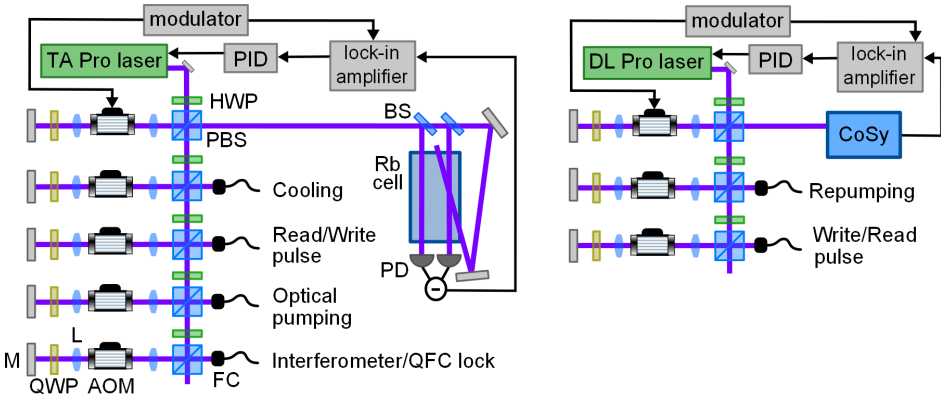

FIGURE 2.2: Main laser setups with the corresponding optics. M, mirror; QWP, quarter-wave plate; HWP, half-wave plate L, lens; AOM, acousto-optic modulator; PBS, polarizing beam splitter; BS, beam splitter; FC, fiber coupler; PID, proportional-integral-derivative controller; PD, photodiode; CoSy, Compact Saturation Spectroscopy module.

During our experiments we need to adjust the power and frequency of several laser beams, and this is done by the laser setup that is schematically drawn in Fig. 2.2. By means of half-wave plates and PBSs we direct an adjustable amount of light to different beam lines with acousto-optic modulators (AOMs). AOMs contain a piece of glass in which sound waves are created by a piezo-electric transducer. These sound waves produce

a spatial modulation in the refraction index of the glass which induces a diffraction of a light beam that passes through it. The frequency and amplitude of the diffracted light depends on those of the sound wave, which can be controlled by the voltage signal applied to the piezo-electric transducer. The light beam is retro-reflected and passes twice through the AOM in order to have a larger frequency tunability. A quarter-wave plate rotates the polarization so that the retro-reflected light is transmitted through the PBS. At this point the light beams are coupled into single mode fibers and distributed to any required location in the optical table for different purposes.

The light in one of the AOM lines is used to lock the frequency of the laser light to a fixed value. This is done using the saturated absorption spectroscopy technique in a cell with rubidium 87 atoms [91]. In order to obtain the frequency derivative signal of the Doppler-free absorption lines, the light frequency is modulated by an AOM and the signal that comes out from the differential photodiode is demodulated by the lock-in amplifier. This frequency derivative signal is used as an error signal that we send to a proportional-integral-derivative (PID) controller. The PID controller then determines and gives out the feedback electronic signal that we apply to the current of the laser diode in order to correct the laser frequency fluctuations. For the TA Pro laser we use a compact module for Doppler-free absorption spectroscopy (the CoSy module from Toptica), which contains a cell with ^{87}Rb atoms and the detection system required to obtain the Doppler-free absorption lines.

2.2 Magneto-optical trap

The central part of our experiments is a trapped cloud of laser-cooled rubidium 87 atoms. This cloud is prepared in a magneto-optical trap (MOT), a technique which was developed around the 1980s and led to the 1997 Nobel Prize awarded to physicists Steven Chu, Claude Cohen-Tannoudji, and William D. Phillips [92–94]. The "ingredients" that are needed to produce these atomic systems include mainly a vacuum chamber, an atomic dispenser, 3 pairs of counter-propagating laser beams, and a magnetic field gradient. These ingredients are combined to engineer an optical absorption of the atoms that is dependent on the velocity and position of the atoms. And this phenomena can be used to trap and cool neutral atoms through the processes named Doppler cooling and magneto-optical trapping.

Doppler cooling: This technique requires that the frequency of the laser beams is slightly lower than the frequency corresponding to an electronic transition of the atoms. In this situation, due to the Doppler effect, a moving atom will experience a higher absorption probability of light propagating in the opposite direction than of light propagating in the same direction. Because of the momentum that light transfers to the atoms in the absorption process, in this situation the atoms experience a force in the opposite direction of their movement. The atoms will therefore slow down and lose energy, which translates into a decrease of their temperature.

Magneto-optical trapping: A magnetic gradient quadrupole field induces a Zeeman shift of the magnetic field sensitive m_F sublevels. This shift increases with the radial distance to the centre of the trap. Because of this, atoms that are not in the centre of the trap have an atomic resonance that is closer to the frequency of the red-detuned laser beams. Therefore

these atoms that are away from the centre have a higher probability to receive photon kicks from the laser light. In order to direct this kick towards the centre of the trap, the polarization of the laser beams has to be correctly adjusted. In particular all the beams need to have circular polarization: for each pair of counter-propagating beams one of the beams has to couple σ^+ atomic transitions and the other one the σ^- transitions.

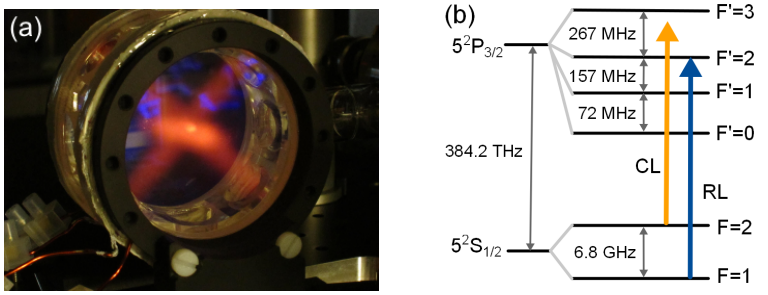

FIGURE 2.3: (a) Picture of our magneto-optical trap setup. One can see the glass vacuum chamber, three pairs of counter-propagating laser beams (orange colour), the support for the anti-Helmholtz coils (holded by black circular mounts) and the atomic cloud (bright spot in the centre of the picture). (b) Atomic structure of the D2 line in ^{87}Rb. The orange and blue arrows represent the frequencies of the cooling (CL) and repumping (RL) laser beams, respectively.

Fig. 2.3 shows a picture of our MOT setup, which has the following technical details. We use three retro-reflected cooling beams with a power $P \approx 10\,\mathrm{mW}$ and a beam waist around 1 cm. They have a red detuning of $\Delta\nu = 22\,\mathrm{MHz}$ with respect to the $\left|5^2\mathrm{S}_{1/2}, \mathrm{F} = 2\right\rangle \rightarrow \left|5^2\mathrm{P}_{3/2}, \mathrm{F}' = 3\right\rangle$ transition. To bring the atoms that fall in $\left|5^2\mathrm{S}_{1/2}, \mathrm{F} = 1\right\rangle$ back to the cooling transition, we have a repumper beam with a power of around 5 mW and waist around 3 mm that couples resonantly the $\left|5^2\mathrm{S}_{1/2}, \mathrm{F} = 1\right\rangle \rightarrow \left|5^2\mathrm{P}_{3/2}, \mathrm{F}' = 2\right\rangle$ transition. Outside the cell we have a pair of solenoid electromagnets in the anti-Helmholtz configuration. They consist of 7 layers of 8 wire winding loops per coil, with a circulating current of 7 A. This current creates a magnetic field gradient in the central position of 20 G/cm

in the axial axis and 10 G/cm in the radial axes. Further details of the experimental apparatus are given in the thesis of Boris Albrecht [95].

In our experiments we need to perform the light-matter interface operations when the atoms are cold. This allows us to have a long coherence time of the atomic quantum states. However these operations cannot be done simultaneously to the cooling stage, since the Doppler cooling process modifies the electronic state of the atoms. Therefore we alternate cooling and trapping stages (around 17 ms) with the light-matter interface operation stage (which can typically last 1-1.5 ms). The cooling stage of 17 ms includes 15 ms of magneto-optical trap operation followed by around 2 ms of optical molasses without the magnetic trap [91].

2.3 Single photon filtering and detection

One very important issue that has to be considered when detecting single photons, is that a small amount of any other light that reaches the detector will affect the signal. Therefore, filtering techniques that transmit the studied single photons but block any other light are very important. In the frame of the DLCZ scheme it is specially important to filter the write (read) photons from the write (read) pulses light (see Fig. 1.4). There are 3 methods that we use to achieve this filtering:

Spatial filtering: in our experiments, the write (read) photon modes are not collinear with the write (read) pulses modes. Having an angle between the two arms allows us to suppress a lot the amount of light from the pulses that is coupled into the photons fibres. However, as explained in Appendix D.2 a bigger angle implies a shorter coherence time of the quantum states that we generate in the atomic ensemble. Therefore in our

experiments this angle is small ranging around $1^\circ - 3^\circ$ and we use other filtering methods.

Polarization filtering: in our experiments the write (read) photons have polarizations that are orthogonal from the ones of the write (read) pulses. This allow us to perform polarization filtering. This is done by inserting polarizing beam splitters (PBSs) in the path of the write and read photon modes before they are coupled into the fibres. Our PBSs show an polarization extinction ratio around $R_{\text{ext}} \approx 10^{-4}$ for the transmitted beam. For the experiments in which the photons are not emitted with horizontal polarization, we use a combination of half-wave and quarter-wave plates to ensure that they are transmitted though the PBS.

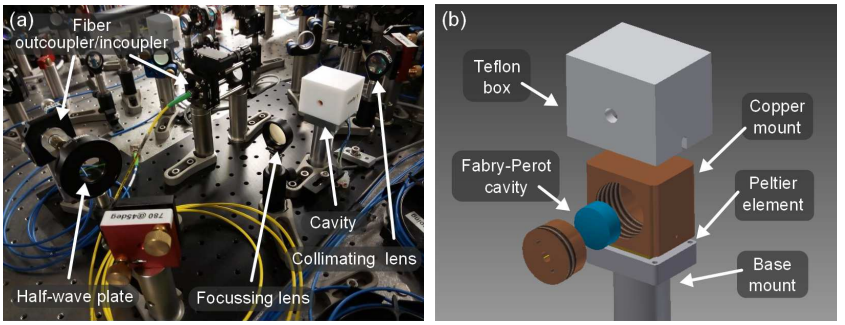

FIGURE 2.4: (a) Picture showing the Fabry-Perot cavity setup, where one can see fiber in- and out-couplers, a waveplate, mirrors, focussing and collimating lenses, and the cavity covered by a Teflon white box. (b) Drawing showing the monolithic cavity, the copper holder, the Teflon box and the Peltier device.

Frequency filtering: in some experiments we use optical Fabry-Perot cavities to filter our generated single photons. These cavities have a free spectral range of FSR=13.4 GHz such that light from only one of the two transitions ($|g\rangle \leftrightarrow |e\rangle$ or $|s\rangle \leftrightarrow |e\rangle$) is transmitted. These cavities help us in suppressing mainly two kinds of noise. First, they contribute to suppress unwanted light from the write and read pulses that is coupled in the write and read photon fibres. Secondly they block any photon

emitted by the atoms in the "wrong" transitions (i.e. photons emitted during the write process on the $|g\rangle \leftrightarrow |e\rangle$ transition and photons emitted during the read process on the $|s\rangle \leftrightarrow |e\rangle$ transition). These cavities consist of a plano-convex shaped monolithic glass with mirror coated surfaces. The transmission peaks have a spectral line-width of $\Delta\nu_{\mathrm{FWHM}} = 53\,\mathrm{MHz}$ with a maximum transmission of 53%. The transmission frequency can be adjusted by controlling the temperature of the cavity. For this purpose, the cavity is held by a copper mount that is in contact with a temperature sensor and a Peltier thermoelectric device.

2.3.1 Characterization of the filtering optical cavities

In order to characterize our Fabry-Perot cavities we used light from one of our lasers. Scanning linearly in time the frequency of the laser allows us to see the transmission peak frequency profile of our cavity. This is what we see in the blue trace of Fig. 2.5a. For a quantitative measurement of the cavity parameters, we compare the cavity transmission signal with the laser lock error signal (green trace). As mentioned in section 2.1 this error signal is obtained by performing saturated absorption spectroscopy in a vapour cell with ^{87}Rb atoms. The zero-crossing that appears more to the right corresponds to the $|F = 1\rangle \leftrightarrow |F' = 2\rangle$ transition and the neighbouring one on the left corresponds to the crossover between the $|F = 1\rangle \leftrightarrow |F' = 1\rangle$ and the $|F = 1\rangle \leftrightarrow |F' = 2\rangle$ transitions [91]. We can use this information to obtain the light frequency separation between these two zero-crossings, which should be 78.5 MHz (cf. Fig. 2.3b). This is the value that we use for the time-to frequency calibration, in order to obtain the cavity linewidth value of $\Delta\nu_{\mathrm{FWHM}} = 53\,\mathrm{MHz}$, which we quote in the previous section.

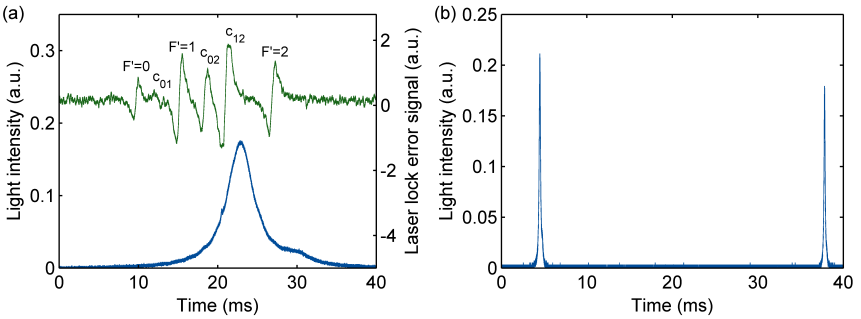

FIGURE 2.5: (a) Temporal traces obtained when scanning linearly the frequency of a laser. The blue trace shows the transmission profile of the Fabry-Perot cavity, and the green trace shows the laser lock error signal. The labels in the lock error signal indicate the excited state F' involved in each transition peak. Labels c_{ij} denote crossovers between two transitions that involve excited states F'=i and F'=j. (b) Transmission profile of the cavity when scanning the laser frequency by more that one cavity FSR.

In Fig. 2.5b we increase the frequency scanning range of the laser so that we can see a full FSR of the cavity. From this measurement we can directly quantify the finesse of our cavity ($\mathcal{F} \approx 250$). This value can then be used to quantify the free spectral range FSR = 13.4GHz and to calculate the extinction ratio of light with a frequency FSR/2 away from a transmission peak ($R_{\text{ext}} \approx 4 \cdot 10^{-5}$) [96].

2.4 Quantum frequency conversion device

In two of the experiments described in this thesis (described in chapter 3 and chapter 6), the wavelength of the photons emitted by our atomic cloud is translated from 780nm to 1552nm. This is done by a setup that we call the Quantum Frequency Converter Device (QFCD) [97]. The central part of this setup is a nonlinear crystal where the nonlinear process difference frequency generation (DFG) takes place [98]. We combine in the nonlinear crystal, single photon fields with $\lambda_{\text{i}} = 780\,\text{nm}$ together with a strong

"pump" laser beam with $\lambda_P = 1569\,\text{nm}$. Throught the process of DFG the frequency of the photons is translated to $\lambda_o = 1552\,\text{nm}$, which is given by the energy conservation of the process ($E_o = E_i - E_P \rightarrow \lambda_o^{-1} = \lambda_i^{-1} - \lambda_P^{-1}$).

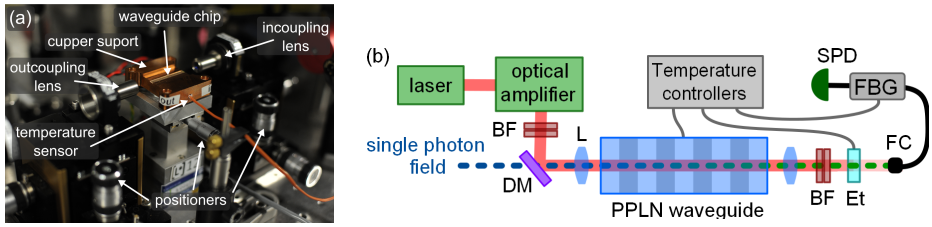

FIGURE 2.6: (a) Picture of the central part of the QFCD. It shows the chip with the nonlinear waveguide, its copper support, the lenses to couple the light on it, and the positioners. (b) Schematic description of the full QFCD. DM, dichroic mirror, L, lens; BF, bandpass optical filter; Et, etalon; FBG, fiber Bragg grating filter; SPD, single photon detector.

As it is shown in Fig 2.6 the single photon field is overlapped in a dichroic mirror with the pump laser beam. This pump beam is generated by an external-cavity diode laser (ECDL) and amplified by an erbium-doped fiber amplifier. The ouput of the amplifier is spectrally cleaned by two bandpass filters (Semrock NIR1, center wavelength 1570 nm, transmission bandwidth 8.9 nm), leading to an ASE suppression of more than 100 dB at 1552 nm. Both single photon and pump fields are later strongly focussed by an aspheric lens with $f = 15.9\,\text{mm}$ to be efficiently coupled to the non-linear crystal, which takes the form of a 3 cm long waveguide (HC Photonics). Using a waveguide allows to have a strong confinement of the light along the entire length of the medium, leading to a higher efficiency of the non-linear process. Our nonlinear waveguide is manufacutred with the proton exchange method and consists of a periodically poled lithium niobate crystal. This periodic poling allows for frequency conversion with the quasi-phase matching technique, which offers the advantage of wavelength flexibility. In our experiment we can slightly tune the poling period of our crystal by adjusting its temperature, which gives us an output wavelength

tunability of few nm around $\lambda_o = 1552\,\text{nm}$. Detecting the frequency converted single photon requires a lot of frequency filtering, specially because of their required overlap with the pump beam which needs a high power for an efficient conversion ($P_P \approx 300\,\text{mW}$ in our case). For this reason we use two bandpass filters (Semrock NIR01-1550/3-25) that are centered at 1552 nm with a bandwidth of 7 nm, which remove most of the pump light (OD ≈ 11 at 1569 nm). However, in this situation there is still a significant amount of noise that prevents us from detecting a clear signal. We believe that this noise comes from a Raman emission process induced by the pump light inside the waveguide. This process generates light within a very broad frequency spectrum together with cystal phonons. This light is broadband, and to remove the most of it we use narrow bandpass filters with a center transmission peak at the photons frequency. In our experiment we use two of these filters: a fiber bragg grating (FBG) with a tranmission peak width of $\Delta\nu = 2.5\,\text{GHz}$ and a Fabry-Perot etalon with $\Delta\nu = 210\,\text{MHz}$ and $\text{FSR} = 4\,\text{GHz}$. The transmission spectrum of both filters can be tuned by changing their temperature. The total extinction ratio of the whole filtering stage for the pump radiation at 1569 nm is $> 150\,\text{dB}$ (100 dB for the two bandpass filters, 44 dB for the FBG and 11 dB for the etalon). And the undesired attenuation that these filtering elements induce to the converted single photon field leads to an imperfect transmission of $\eta_{\text{filter}} = 36\%$ (86 % from the two bandpass filters, 70 % from the FBG and 60 % from the etalon). To study the frequency converted photons we detect them with InGaAs single photon detectors (SPDs).

2.5 Mach-Zehnder interferometers

In chapter 5 we describe an experiment where we study the generation of entanglement between a photonic time-bin qubit and an atomic excitation. Photonic time-bin qubits are single photons which are delocalized over two temporal windows (commonly denoted early $|\mathrm{E}\rangle$ and late $|\mathrm{L}\rangle$ time-bins). In order to verify and analyze these superposition states, one can use a stable Mach-Zehnder interferometer that overlaps the two time-bins. This overlap is obtained when the optical path delay of the interferometer is equal to the time separation between the two time-bins. In this situation the interferometer can act as a projective measurement device, projecting the state in any basis that lies within the equator of the Bloch sphere $(|\mathrm{E}\rangle + e^{i\phi}|\mathrm{L}\rangle)/\sqrt{2}$ [99, 100]. The phase ϕ corresponds to the phase delay between the two interferometer arms.

In order to have a good phase stability and control, the interferometer optical path delay has to be controllable with a precision much smaller than the light wavelength. In our experiments the separation between time-bins is 175ns corresponding to a fiber optical path delay around 40 m. Having such a big delay that remains stable within the few nanometres range was one of the challenges of the experiment.

A schematic representation of our fiber Mach-Zehnder interferometer can be seen in Fig. 2.7a and a picture of it is shown in (b). In one arm of the interferometer there is a polarization controller used to maintain the polarization overlap at the output fiber beam-splitter. In the other arm there is a piezo-electric ceramic cylinder that has a section of the fiber rolled around it. Applying a voltage to the piezo cylinder changes the stress that is induced to the fiber, which affects the interferometer optical path delay.

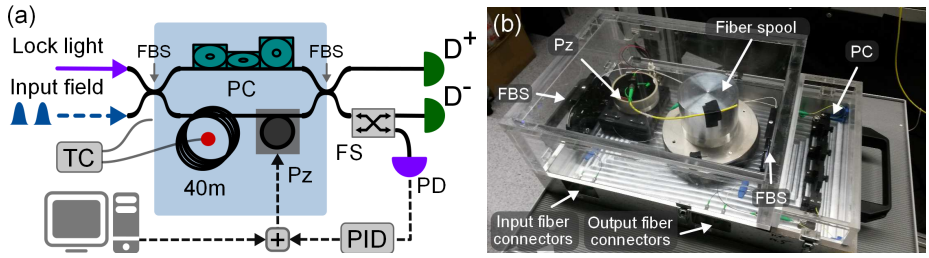

FIGURE 2.7: (a) Scheme depicting the components present in our Mach-Zehnder interferometer setups. FBS, fiber beam splitter with 50/50 split ratio; TC, temperature controller connected to a temperature sensor (red dot) and a heat pad; PC, polarization controller, Pz, piezo-electric fiber stretcher; FS, fiber switch; PD, photodiode; PID, proportiona-integral-derivative controller. Detectors D^+ and D^- represent the SPDs that are used to detect each of the two outputs of the interferometer. (b) Picture of the box with the optical Mach-Zehnder interferometer inside.

This allows us to compensate the interferometer delay fluctuations and also to adjust it to the desired value.

We use a laser beam as a reference for the stabilization of the interferometer. This lock laser light enters the interferometer through one of the two input fibers and is detected by a photodiode (PD) in one of the interferometer outputs. The signal of this photodiode is given to a PID module, which generates a correction voltage that is applied to the piezo-electric cylinder in order to keep the photodiode signal at a certain locking value. Since we do not want the lock light to be mixed with the single photons, the interferometer is typically operated in two alternating stages. We perform repeatedly 13.3 ms of interferometer active stabilization, followed by 1.4 ms of single photon analysis. A fiber switch directs alternately one of the interferometer outputs to the lock light photodiode and the single photon detector.

To improve the stability of the interferometer we also accurately stabilize its temperature. For this purpose, the interferometer is placed inside a box that has an aluminium base in contact with a heating pad. We use this

heating pad together with a temperature sensor and a PID controller in order to actively stabilize the temperature inside the interferometer box. We can do this with a temperature precision of around 0.01°C.

2.5.1 Characterization

In order to characterize the Mach-Zehnder interferometers we used light pulses with similar characteristics as the time-bin qubits that we wanted to analyse. The temporal profile of the pulses at the output of the interferometer is shown in the insets of Fig. 2.8. For both insets, the first peak corresponds to light from the early pulse bin that passes through the short interferometer arm. The third peak corresponds to light from the late bin that passes through the long interferometer arm. The central peak corresponds to an overlap of light from the early bin that passes through the long interferometer arm or light from the late bin that passes through the short interferometer arm. These two light paths interfere, and the two insets correspond to two different values of the phase difference between the two input light bins. The light intensity in the central peak can be mathematically described in the monochromatic case as $I = I_1 + I_2 + 2\sqrt{I_1 I_2}\cos\phi$ [96], where I_1 and I_2 are the intensities at the ouput of each short and long interferometer arms, and ϕ is the phase difference between the two light fields. The blue points in Fig. 2.8 show the total energy of the central output peak as a function of the phase difference between the two input light bins. The oscillation shows a visibility of $V = 95\%$. In Appendix E we discuss the impact on the visibility of two effects: unbalanced intensities and the linewidth of the two lasers used for the pulses and the interferometer lock light. This impact can be mathematically described as

$$V = \frac{2\sqrt{I_1 I_2}}{I_1 + I_2} e^{-2(\pi \Delta t \sigma_\nu)^2} \tag{2.1}$$

where σ_ν is the frequency width of the global laser spectrum and Δt is the interferometer temporal delay. Assuming that all the visibility loss is due to the linewidth effect, we can use the previous equation to obtain an upper bound for the global laser linewidth: $\sigma_\nu \approx 290\,\text{kHz}$.

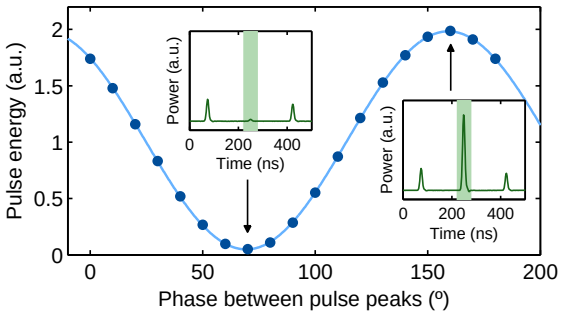

FIGURE 2.8: Interferometer characterization with bright pulses mimicking the photonic time-bin qubits analysed in the experiment. The insets show the temporal profile of the light fields at the output of the interferometer. The blue points show the output energy of the central bin (highlighted with a green area in the inset).

As mentioned in the previous section, in order to adjust the interferometer phase we can apply a voltage to the piezo-electric fiber stretcher. It is therefore important to have a good calibration that relates these two quantities. This can be seen in Fig. 2.9, which shows the phase of the interference fringe in Fig. 2.8 for different voltages applied to the piezo-electric fiber stretcher. We built two interferometers in order to analyse both the write and read photons generated in our DLCZ scheme. The blue dots represent the data obtained from the write photon interferometer, while the green open circles are obtained from the read photon interferometer. The linear fits of the calibration data give a relation of $-335.4°/\text{V}$ and

$-384.4°/\mathrm{V}$ for the write and read interferometers, respectively. These calibration values were used in order to obtain the voltages that we needed to apply when we wanted to perform qubit projection measurements with a certain phase.

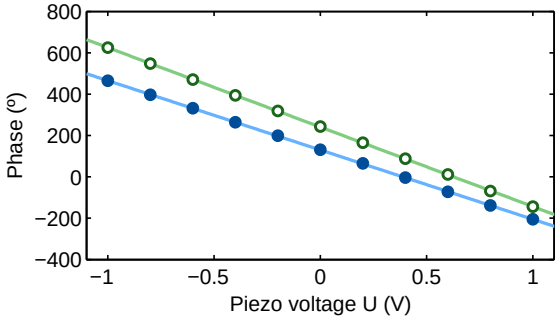

FIGURE 2.9: Phase of the interference fringe shown in Fig. 2.8 as a function of the voltage applied to the piezo fiber stretcher. The blue dots correspond to data of the write interferometer and the green open circles correspond to the read interferometer.

2.5.2 Performance progress

The design and characterisation of the Mach-Zehnder interferometers shown in the last paragraphs corresponds to the final situation after several improvements from the initial design. In this section we characterize some of the progress that we made towards having the interferometer stability that we required.

Interferometer delay

The original length of the fiber in the long interferometer arm was around 80 m. This was giving an optical path delay around $\Delta t = 390\,\mathrm{ns}$. The reason behind choosing this delay is a trade-off between two effects. The first effect is that shorter interferometers show less visibility loss given by the laser linewidth, as shown in Eq. (2.1). The second effect is that having a

shorter interferometer delay requires having a shorter separation between the qubit time bins that one wants to analyse with it. As explained in chapter 5 if the temporal separation between the qubit time bins is short compared to their width this leads to an imperfect dephasing and rephasing of the spin-wave component of the entangled state, which affects the quality of the entanglement.

In this experiment, the shortest possible duration of our photons was around 20-30 ns, limited by the switching time of our AOMs. Therefore we started with a separation between time-bins around 10-20 times longer (corresponding to the mentioned interferometer delay of $\Delta t = 390\,\text{ns}$). In this configuration we measured a interference visibility of around $V \approx 0.78$, compatible with eq. 2.1. This visibility value became eventually a limitation for our entanglement experiment, and therefore, we decided to shorten the fiber in the long arm of the interferometer from around 80 m to around 40 m. This new length gave a interferometer delay of $\Delta t = 175\,\text{ns}$. With this shorter delay we obtained the visibility value of $V = 95\%$ shown in Fig. 2.8, which significantly improved the data of the entanglement experiment.

Interferometer polarization stability

As mentioned before, it is important to have a good polarization overlap at the output beamsplitter of the interferometer, in order to obtain a high visibility of the interference. This can be adjusted using the polarization controller shown in Fig. 2.7. However, it can happen that the polarization controller also modifies the interferometer phase delay. Since we do not want this to happen while we are acquiring data, we can only use the polarization controller before starting our measurements.

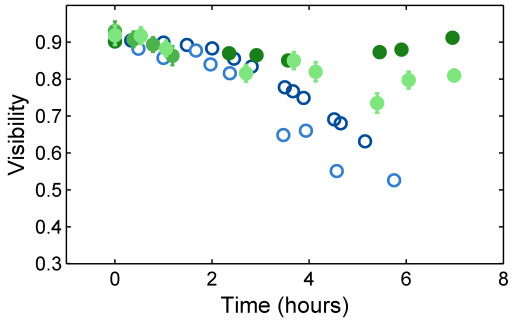

FIGURE 2.10: Optical interference visibility of the Mach-Zehnder interferometer measured different times after optimizing the polarization overlap. Each colour denotes an independent data trace. The traces with blue open circles were taken with no active temperature stabilization. For the data shown as green dots, we used a temperature controller in combination of a temperature sensor and a heat pad, to actively stabilize the temperature inside the interferometer box. This data corresponds to one of the two interferometers that we built. The improvement with active temperature stabilization was not that clear in the other interferometer, which could be due to the differences in the isolation box.

In Fig. 2.10 we show the long term visibility stability, which is limited by the drift of the light polarization. One possible explanation for this drift can be temperature instability. Temperature changes inside the interferometer box can lead to a modification of the stress experienced by the section of fiber that is rolled around the piezoelectric fiber stretcher or the spool, through thermal expansion of these elements. This stress change can modify of the birefringence of the fiber and degrade the light polarization overlap at the interferometer output. We believe this effect was one of the limitations for the long term stability of our interferometers and we therefore implemented the active temperature stabilization system shown in Fig. 2.7. The traces below with blue open circles were taken without any active temperature stabilization, while the green dots were taken after stabilizing the interferometer box temperature with a heat pad.

Chapter 3

Telecom quantum frequency conversion of single photons correlated with atomic spin excitations

The results presented in this chapter have been published in [101], and the text is mostly adapted from the publication. This experiment was done in collaboration with PhD student Nicolas Maring, who was in charge of the quantum frequency conversion device.

3.1 Introduction

As mentioned in subsection 1.2.3, the essential building block of most quantum repeater achitectures is a photonic quantum memory (QM) which provides an interface between stationary quantum bits (encoded in atom-like

systems) and flying quantum bits (encoded in photons) [7]. Heralded entanglement between remote QMs can be achieved by quantum interference of photonic modes that are correlated to the QMs at a central measurement station [24, 25, 33–35]. To achieve long distance entanglement, it is essential that the heralding photon is at telecom wavelength, in order to minimize loss in optical fibers. A crucial enabling step is therefore the ability to obtain quantum correlation between a telecom photon (preferably in the C band where the loss is minimal) and a long-lived atomic state in a quantum memory.

The best current QMs operate with photons in the visible or near infrared regime [7, 9, 13, 102–104], which strongly limits the possibilities of long distance transmission. Although progress is being made towards quantum memories functioning directly at telecom wavelengths [52, 53, 105, 106], the current demonstrations in the quantum regime still suffer from short coherence times (ns time-scale) and low efficiencies. There are basically two different approaches to connect visible QMs to telecom wavelengths. The first one is to use photon pair sources intrinsically emitting entangled photon pairs with one photon at telecom wavelength and the other one in the visible or near infrared regime to be memory compatible. This photon then can be stored in a write-read QM where the photon is mapped onto an atomic state and can be retrieved back on demand [19, 20, 107–112]. The second possibility is to use read-only QMs emitting photons entangled with the atoms, and to convert the emitted photons to telecom wavelengths. Significant efforts have been devoted to quantum frequency conversion (QFC) of single photons towards the telecom band [54–57, 113–118], although only very few examples are compatible with quantum memories [54, 55, 57, 117]. Ref. [57] demonstrated the quantum frequency conversion to the C-band of a single read-out photon emitted by a Rb-based quantum memory with

an efficiency of 30 %, using an integrated waveguide approach. However, in that experiment there was no correlation left between the converted photon and the quantum memory. The conversion of the heralding photon from a QM was so far only realized in a single experiment in which photons were converted from 795 nm to 1367 nm (E-band) via four wave mixing (FWM) in a cold and dense ensemble of rubidium atoms [54, 55]. In contrast to the conversion of the read-out photon, the heralding write photon conversion is much more challenging in terms of noise suppression, because the emission probability of the write photon needs to be low (typ. $< 1\,\%$) to avoid multiple spin-wave-excitations in the same mode leading to uncorrelated photons emitted in that mode. Hence, a constant background-noise due to the conversion process has a much higher impact on the signal-to-noise ratio (SNR) of the heralding write photons than of the heralded read photons. In order to reach a high heralding efficiency after conversion, the background noise must therefore be very low.

In this experiment, we demonstrated low-noise quantum frequency conversion of the initial heralding write photon from our cold rubidium QM to 1552 nm via difference frequency generation in an integrated non-linear waveguide. The QM is implemented in a cold ensemble of ^{87}Rb atoms following the DLCZ scheme (c.f. subsection 1.2.4) and we use a periodically poled Lithium Niobate (PPLN) waveguide for conversion. In contrast to the FWM approach in cold atoms, QFC via solid-state waveguides offers major advantages such as wavelength flexibility, robustness, relative simplicity, and excellent prospects for on-chip-integration. By combining high QFC efficiency and ultra-narrowband filtering, we demonstrate that with the presented approach a high degree of non-classical correlations between an atomic spin-wave stored in the QM and a flying telecom photon can be

achieved, as well as high SNR for the detection of the converted heralding photon, leading to a high spin-wave heralding efficiency.

3.2 Experiment description and setup

The experimental setup is depicted in Fig. 3.1a and basically consists of two parts – the atomic QM and the quantum frequency conversion device (QFCD). After cooling the ^{87}Rb atoms in the magneto optical trap (MOT) they are prepared in the ground state $|g\rangle = |5^2S_{1/2}, F = 2, m_F = 2\rangle$ by optical pumping (cf. Fig. 3.1b). This is done by applying repumping light (resonant with the $|F = 1\rangle \rightarrow |F' = 2\rangle$ transition) and σ^+ polarized optical pumping (OP) light on the $|F = 2\rangle \rightarrow |F' = 2\rangle$ transition (the two beams come from two independent lasers as mentioned in section 2.1). This OP light beam is detuned by 10 MHz from the transition resonance in order to avoid problems related to the formation of dark states. After optically pumping the atoms in $|g\rangle$, a weak Gaussian-shaped write pulse (FWHM duration $\tau_W = 20$ ns), 40 MHz red-detuned from the $|g\rangle \leftrightarrow |e\rangle = |5^2P_{3/2}, F' = 2, m_F = 1\rangle$ transition, probabilistically creates a single collective spin excitation (spin-wave) between the two ground states $|g\rangle$ and $|s\rangle = |5^2S_{1/2}, F = 1, m_F = 0\rangle$. The spin-wave can be stored for a programmable time in the QM and is heralded by a Raman scattered write photon ($\tau_w = 22$ ns). The write photon is circularly polarized with respect to the experiments' quantization axis, set by a weak homogeneous static magnetic field applied over the whole cloud. We couple a small fraction of the isotropically emitted write photons under an angle of 3° with respect to the write pulse axis into a single mode fiber (coupling efficiency approx. 60%). Besides that spatial filtering, we also perform polarization filtering

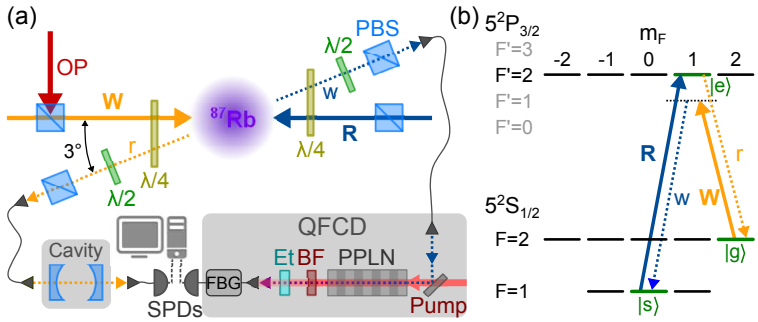

FIGURE 3.1: (a) Experimental setup. Write pulse (W) and Read pulse (R) are sent counter-propagating into the atomic cloud. Write and read photonic modes are denoted by w and r. The QFCD consists of the PPLN waveguide, a bandpass filter (BF), a narrowband etalon (Et), and a fiber bragg grating (FBG). (b) Energy levels and coupling scheme for the DLCZ experiment.

of the write photon using a combination of quarter- and half-wave plates, as well as a polarization beam splitter as described in section 2.3.

The afterwards linearly polarized write photon is sent to the QFCD (cf. section 2.4). First it is overlapped on a dichroic mirror with the spatial mode of the pump laser at 1569 nm. A combination of lenses (not shown in Fig. 3.1a) ensures optimal focussing and mode matching of the beams into the temperature stabilized PPLN waveguide in which the conversion of the write photon from 780 nm to 1552 nm takes place. Afterwards, the pump radiation is blocked by a combination of two bandpass filters each with a transmission bandwidth of 7 nm around 1552 nm. However, further filtering is required to detect the converted write photon at the single photon level because of noise generated by spontaneous Raman scattering of the pump beam which leads to a broad background around the target wavelength. In contrast to former work [57, 97], we apply a two-stage additional filtering consisting of an etalon with a bandwidth of 210 MHz and a free spectral range of 4 GHz and a fiber Bragg grating (FBG) of 2.5 GHz bandwidth. This allowed us to achieve high values of SNRs at low

photon number, which is necessary for the quantum frequency conversion of the heralding write single photons. The converted write photons are finally detected by an InGaAs single photon detector (SPD) (ID Quantique ID230) with a detection efficiency of $\eta_{\mathrm{d},1552} = 10\%$.

3.3 Results

3.3.1 The quantum frequency conversion device

The development and characterization of the QFCD was not part of this PhD thesis. I nevertheless include its description here to help the reader understand the full experiment.

The characterization of the QFCD is shown in Fig. 3.2. We couple 1.2 mW of continuous wave input light at 780 nm to measure the total conversion efficiency and single photon level coherent input pulses of 16 ns duration with a mean photon number per pulse of $\mu_{\mathrm{in}} = 0.16$ to measure the SNR versus the coupled pump power (measured behind the waveguide). The plotted internal efficiency η_{int} excludes all optical losses, e.g. due to initial coupling in the waveguide ($\eta_{\mathrm{cpl}} \approx 74\%$), all subsequent filtering stages ($\eta_{\mathrm{filter}} \approx 36\%$), all optical surfaces including one optical isolator ($\eta_{\mathrm{surf}} \approx 70\%$) and the final fiber coupling ($\eta_{\mathrm{fiber}} \approx 75\%$). The data are fitted with the models described in [57, 97] and we retrieve a normalized conversion efficiency of $\eta_n = 61\,\%/\mathrm{W/cm^2}$ and a maximum internal efficiency of $\eta_{\mathrm{int}}^{\mathrm{max}} = 72\%$ which corresponds to a maximum total device efficiency of $\eta_{\mathrm{dev}}^{\mathrm{max}} \approx 10\%$ with $\eta_{\mathrm{dev}} = \eta_{\mathrm{int}}\eta_{\mathrm{loss}}$, and $\eta_{\mathrm{loss}} = 14\%$. The SNR is defined as the ratio of detections due to converted single photons and detections due to other causes. It follows the expected behaviour (blue line) showing a drop for low pump powers due to the dark counts of our

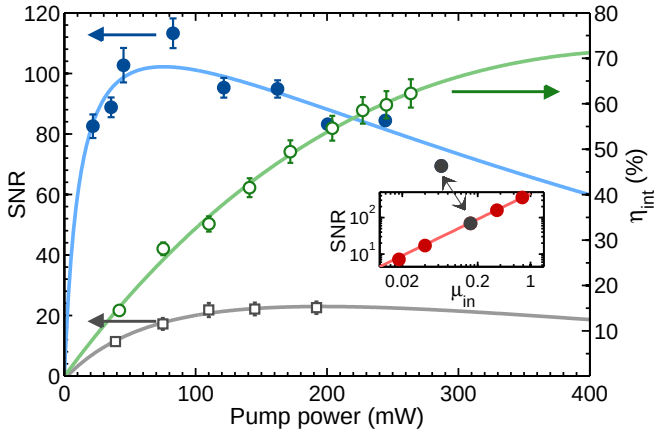

FIGURE 3.2: QFCD characterization. Signal to noise ratio SNR (blue dots for full filtering, grey squares without etalon, left axis) measured with a mean input photon number per pulse of $\mu_{\text{in}} = 0.16$ and internal efficiency η_{int} of the QFCD (green circles, right axis) measured with classical input light vs. pump power measured after the waveguide. The data are fitted by functions, modeling the expected behavior (solid lines). The inset shows the SNR vs. μ_{in} for a fixed pump power of $P_{\text{pump}} = 287\,\text{mW}$. Error bars correspond to ± 1 standard deviations of the photon counting statistics.

detector ($\text{DC}_{1552} = 10\,\text{Hz}$) as well as a decrease for very high pump powers due to the non-linear dependence of η_{int} on P_{pump}. For comparison we also included a trace of the SNR measured without the etalon (grey squares) which shows significantly worse filtering. The inset shows the SNR depending on the mean input photon number μ_{in} for full filtering (including the etalon) for a fixed pump power of $P_{\text{pump}} = 287\,\text{mW}$. We observe the expected linear dependence $\text{SNR} = \text{SNR}_{\text{max}} \times \mu_{\text{in}}$ with $\text{SNR}_{\text{max}} = 452$ for a single photon input (i.e. $\mu_{\text{in}} = 1$).

3.3.2 Frequency conversion of photons paired with spin-waves

The next step was to combine the QFCD with the cold atomic QM to convert the write photons from 780 nm to 1552 nm and investigate the joint

properties of the telecom photons and the atomic spin-waves stored in the QM. We created the spin-waves with weak Gaussian shaped write pulses of $\tau_W = 20\,\text{ns}$ duration, and the width of write photon detection gate was set to 40 ns (cf. green area in the inset of Fig. 3.3a). To gain information about the spin-wave, we sent a read pulse ($\tau_R = 35\,\text{ns}$, $P_R = 190\,\mu\text{W}$) resonant to the $|s\rangle \leftrightarrow |e\rangle$ transition to convert the spin-wave back into a single read photon (c.f. subsection 1.2.4). In this experiment, the read photon was then polarization filtered before being sent through the Fabry-Perot cavity described in section 2.3 ($\eta_{cav} \approx 20\%$ total transmission, including cavity transmission and subsequent fiber coupling) for spectral filtering. And finally detected in a window of 100 ns by a silicon SPD (Excelitas SPCM-AQRH-14) with $\eta_{d,780} = 40\%$ efficiency. The read-out efficiency is defined as the probability to map a heralded spin-wave onto a read photon. Its raw value is calculated as $p_{r|cw} = p_{cw,r}/p_{cw}$, where $p_{cw,r}$ is the probability per trial to detect a coincidence between a converted write and a read photon and p_{cw} is the probability per trial to obtain a detection event in the converted write photon detector. The fiber-coupled read-out efficiency $p^{\text{fiber}}_{r|cw} = p_{r|cw}/(\eta_{cav}\eta_{d,780})$ corresponds to the probability of finding a read photon in the optical fiber after the vacuum cell, i.e. corrected for filtering and detector efficiency only.

To demonstrate that the conversion of the write photon preserves its quantum character, we measured the normalized second-order cross-correlation between the converted write photon and the read photon defined as $g^{(2)}_{cw,r} = p_{cw,r}/(p_{cw}p_r)$. For comparison we also took the cross-correlation $g^{(2)}_{w,r}$ without write photon conversion, for which we replaced the QFCD by a Fabry-Perot filtering cavity with similar characteristics as the one used for the read photons but resonant with the write photons. The obtained data are shown in the Fig. 3.3a as blue dots for $g^{(2)}_{cw,r}$ and blue circles for $g^{(2)}_{w,r}$ vs. the

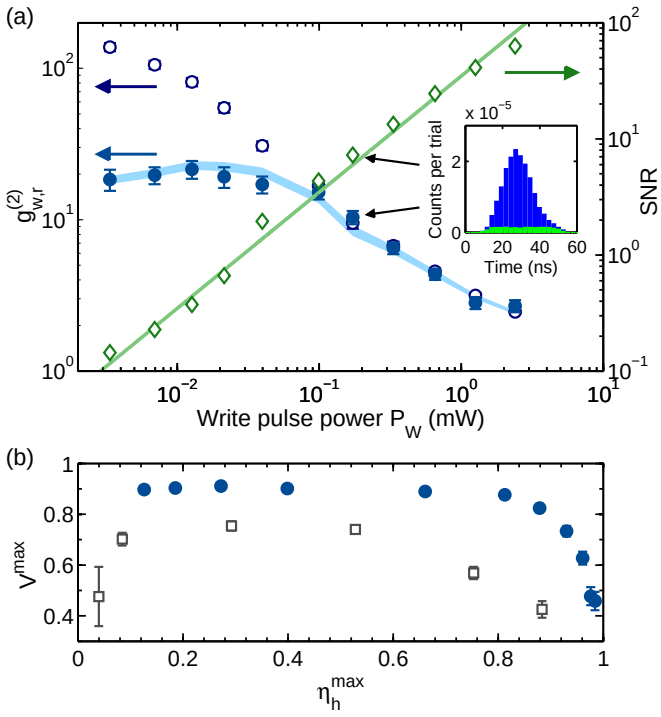

FIGURE 3.3: (a) Normalized cross-correlation of the unconverted write photons (blue circles, left axis) and the converted ones (blue dots) with the read photons and SNR of the converted write photons (green diamonds, right axis, errorbars smaller than symbol size) vs. peak power of the write pulse. The blue shaded area corresponds to the expected $g^{(2)}_{\mathrm{cw,r}}$ as inferred from Eq. (3.1), and the SNR is fitted by a linear regression (green line). The inset shows as an example the detected shape of the converted write photon for $P_{\mathrm{W}} = 333\,\mu\mathrm{W}$. The pump power was fixed at $P_{\mathrm{pump}} = 290\,\mathrm{mW}$. (b) Extrapolated maximal visibility V^{max} for interfering two frequency converted photons from two atomic ensembles depending on the maximal heralding efficiency $\eta_{\mathrm{h}}^{\mathrm{max}}$ (blue dots for full filtering, grey squares without etalon).

applied power of the write pulse. We observe the highest cross-correlation of $g^{(2)}_{\mathrm{cw,r}} \approx 20$ for a write pulse power of $P_{\mathrm{W}} \approx 10\,\mu\mathrm{W}$. For higher P_{W}, $g^{(2)}_{\mathrm{cw,r}}$ decreases, as expected for a DLCZ-type QM (cf. Appendix A.2.1). For lower values of P_{W}, $g^{(2)}_{\mathrm{cw,r}}$ slightly drops due to noise introduced by the QFCD and the dark counts of the SPDs [119]. This also explains the deviation of $g^{(2)}_{\mathrm{cw,r}}$ from $g^{(2)}_{\mathrm{w,r}}$ in the low P_{W} regime. The measured $g^{(2)}_{\mathrm{cw,r}}$ values in Fig. 3.3a are well above the classical limit of 2, assuming thermal

statistics for the write and read beams (see below). This shows that we can operate the combined QM-QFC device for a large range of write pulse powers in a highly non-classical regime. The experimental data follow well the expected behavior taking into account the background noise created by the QFCD pump laser (indicated by the blue shaded area) which can be deduced from

$$g^{(2)}_{\mathrm{cw,r}} = \frac{g^{(2)}_{\mathrm{w,r}} + \mathrm{SNR}^{-1}}{1 + \mathrm{SNR}^{-1}}. \tag{3.1}$$

Here, $g^{(2)}_{\mathrm{w,r}}$ denotes the measured cross-correlation if the write photon is sent through the filtering Fabry-Perot cavity instead of the QFCD and SNR is the signal to noise ratio of the converted write photon. $\mathrm{SNR} = (p_{\mathrm{cw}} - p_{\mathrm{N}})/p_{\mathrm{N}}$, where p_{N} is the probability to have a detection when the write photon is blocked before the QFCD (see also Appendix F). The good agreement between the experimental data and the simple model suggests that the noise generated by the QFCD pump beam is the main limiting factor for the value of $g^{(2)}_{\mathrm{cw,r}}$.

Moreover, we proved unambiguously the high degree non-classical correlations between the converted write photons and the retrieved read photons by violating the Cauchy-Schwarz inequality for classical light, given by

$$R = \frac{\left(g^{(2)}_{\mathrm{cw,r}}\right)^2}{g^{(2)}_{\mathrm{cw,cw}} \cdot g^{(2)}_{\mathrm{r,r}}} \leq 1 \tag{3.2}$$

where $g^{(2)}_{\mathrm{cw,cw}} = \frac{p_{\mathrm{cw,cw}}}{p_{\mathrm{cw}} p_{\mathrm{cw}}}$ ($g^{(2)}_{\mathrm{r,r}} = \frac{p_{\mathrm{r,r}}}{p_{\mathrm{r}} p_{\mathrm{r}}}$) denotes the unheralded auto-correlation function of the converted write (read) photons. The measured correlation values for different write powers and the inferred Cauchy-Schwarz parameter R are given in Table 3.1. Even for relatively high write pulse powers we clearly violate Eq. 3.2. For $P_{\mathrm{W}} = 0.17\,\mathrm{mW}$ we obtain $R = 31$ violating the Cauchy-Schwarz inequality by more than four standard deviations,

TABLE 3.1: Measured values of the coincidence detection probability $p_{\mathrm{cw,r}}$, the cross-correlation $g^{(2)}_{\mathrm{cw,r}}$ and the unheralded auto-correlations $g^{(2)}_{\mathrm{cw,cw}}$ and $g^{(2)}_{\mathrm{r,r}}$ of the converted write photons and read photons for different write pulse powers P_{W}. Errors correspond to ± 1 standard deviation. The Cauchy-Schwarz parameter R is calculated from Eq. 3.2.

P_{W} (mW)	$p_{\mathrm{cw,r}}$ (%)	$g^{(2)}_{\mathrm{cw,r}}$	$g^{(2)}_{\mathrm{cw,cw}}$	$g^{(2)}_{\mathrm{r,r}}$	R
2.39	$4.2 \cdot 10^{-3}$	2.48(6)	2.0(2)	2.16(9)	1.4(2)
0.65	$1.2 \cdot 10^{-3}$	4.49(8)	2.3(3)	2.04(9)	4.4(7)
0.17	$0.3 \cdot 10^{-3}$	9.9(2)	1.6(4)	2.0(1)	31(7)

clearly demonstrating strong non-classical correlations between the converted write photons and the retrieved read photons.

In addition to non-classical correlations, another requirement to build a reliable QR is to achieve a high SNR in the detection of the converted heralding photon. Hence, we investigated the SNR of the frequency converted write photon depending on the write pulse power. The results are shown as green diamonds in Fig. 3.3a. We observe the expected linear increase of the SNR with write pulse power as $\mathrm{SNR} \propto P_{\mathrm{W}}$. For large P_{W} we observe SNRs > 50 while still being in the the non-classical regime.

From the data presented in Fig. 3.3a, we can obtain more insight about the performance of our combined QM-QFC device for quantum information protocols. From the measured $g^{(2)}_{\mathrm{cw,r}}$, we can infer the maximal visibility $V^{\max}$ that could be achieved in a two photon interference experiment. For example if the atomic qubit was entangled with a converted photonic qubit (e.g. in polarization [18] or time-bin [120]) or in a two ensemble entanglement experiment [121] we can infer $V^{\max} = (g^{(2)}_{\mathrm{cw,r}} - 1)/(g^{(2)}_{\mathrm{cw,r}} + 1)$. Here, it is assumed that the QFCD is phase-preserving [97, 116]. Also from the measured SNR, we can infer the maximal heralding efficiency $\eta_{\mathrm{h}}^{\max} = \mathrm{SNR}/(\mathrm{SNR} + 1)$ of the combined QM-QFC device for heralding the presence of a spin-wave in the ensemble. The infered $V^{\max}$ is plotted

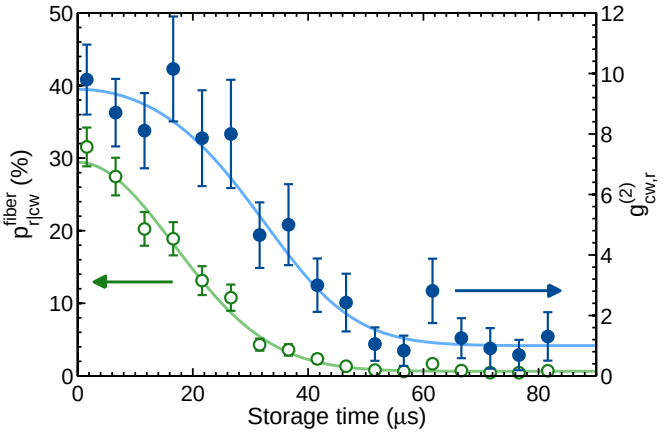

FIGURE 3.4: Spin-wave lifetime characterization. Read-out efficiency (green circles, left axis) and normalized cross-correlation of the converted write photons and read photons (blue dots, right axis) vs. storage time in the QM. The write and pump powers were fixed at $P_{\mathrm{W}} = 0.18\,\mathrm{mW}$ and $P_{\mathrm{pump}} = 290\,\mathrm{mW}$.

as a function of $\eta_{\mathrm{h}}^{\max}$ in Fig. 3.3b. We infer a visibility of $V \approx 90\%$ up to 80% heralding efficiency for full filtering (blue dots). $V^{\max}$ decreases for higher $\eta_{\mathrm{h}}^{\max}$, but we still obtain $V^{\max} > 1/\sqrt{2}$, potentially enabling a violation of the Clauser-Horne-Shimony-Holt (CHSH) type Bell inequality, for $\eta_{\mathrm{h}}^{\max} > 90\%$. This confirms the suitability of the combined QM-QFC device as a elemental building block of a QR for long distance quantum communication. If the etalon is removed, $V^{\max}$ drops significantly (cf. grey squares) clearly demonstrating the importance of ultra-narrowband filtering for the all-solid state based QFC approach. It should be stressed that these values are given only to infer the potential of our device for quantum information experiments, and should be confirmed with further measurements.

Finally, we investigated the capability of the combined QM-QFC device to preserve the non-classical correlations of the converted write photons and the stored spin-wave depending on the storage time in the QM. The

read-out efficiency $p_{\mathrm{r|cw}}$ (green circles in Fig. 3.4) decreases over storage time due to dephasing of the stored spin-wave mainly induced by thermal atomic motion and to a smaller degree by external spurious magnetic field gradients. The decay can be fitted with a theoretical model explained in Appendix D (see green line in Fig. 3.4) giving a decay time of $\tau = 23.6 \pm 0.8\,\mu$s. However, the storage time is not a fundamental limitation here, as it could be increased by orders of magnitude using other techniques (cf. subsection 1.3.1). The normalized cross-correlation $g^{(2)}_{\mathrm{cw,r}}$ between the converted write photons and the retrieved read photons is shown as blue dots in Fig. 3.4 for a write pulse power of $P_{\mathrm{W}} = 0.18\,$mW. We observe the expected decay of $g^{(2)}_{\mathrm{cw,r}}$ and fit the data with the above mentioned model, giving a decay time of $\tau = 25.8 \pm 1.2\,\mu$s which is consistent with the result obtained when fitting $p_{\mathrm{r|cw}}$. Fig. 3.4 shows that we stay in the non-classical regime ($g^{(2)}_{\mathrm{cw,r}} > 2$) up to storage times of about $40\,\mu$s which corresponds to a fiber transmission length of approximately 8 km.

3.4 Discussion and conclusions

The performance of the QFCD is currently mainly limited by technical issues like coupling efficiencies in the PPLN wave-guide and into the final optical fiber as well as transmission efficiencies through the filtering stage and other optical surfaces. However, with the current device conversion efficiency of about 10 % and typical fiber-absorptions of 0.2 dB/km for 1552 nm and 3.5 dB/km for 780 nm, the unconverted photon travelling in a 780 nm fiber would experience a higher loss after around 3 km than a frequency converted photon travelling in a telecom fiber. Hence, even with this seemingly low conversion efficiency, QFC beats direct transmission already after a few km.

In conclusion, in this experiment we demonstrated highly non-classical correlations between a frequency converted telecom C-band photon and a spin-wave stored in our atomic quantum memory. The photon heralding the spin-wave was converted from 780 nm to 1552 nm using an integrated non-linear waveguide. We showed that by improved optical filtering, very high signal to noise ratios up to $\mathrm{SNR}_{\mathrm{max}} = 452$ for a weak coherent input pulse with on average one photon per pulse could be achieved. This was the key to obtain highly non-classical correlations between the converted write and read photons up to $g^{(2)}_{\mathrm{w,r}} \approx 20$ when the QFCD was combined with the QM, as well as high SNRs for the detection of the converted write photon, leading to high spin-wave heralding efficiencies. Moreover, we proved that the quantum character of the converted write photons and read photons are preserved by violating the Cauchy-Schwarz inequality by more than four standard deviations. Finally, we demonstrated that the non-classical correlations between the heralding telecom write photon and the near infrared read photon could be stored in the QM up to 40 μs. This experiment showed that quantum frequency conversion based on integrated non-linear waveguide is a viable approach to create quantum correlation between telecom photons and long-lived spin-waves.

During the publication stage of this work we learned about a similar experiment [122]. More recent related experiments include the frequency conversion of single photons emitted by a single trapped ion [123, 124] or a NV center [60], the telecom frequency conversion of single photons entangled with a trapped ion [58] or an atomic ensemble [125], or the telecom frequency conversion of photons resonant to other matter systems such as doped crystals [61] or trapped ions [59, 126].

Chapter 4

Generation of heralded single photons with highly tunable temporal waveform

The results presented in this chapter have been published in [127], and the text is mostly adapted from the publication. This work has been done in collaboration with a theory group from the University of Basel led by Prof. Nicolas Sangouard.

4.1 Introduction

A vast range of experiments in quantum information science and technology rely on single photons as carriers of information [128]. Single photon sources are thus key components and have been continuously improved over the past years [129]. The spectrum and temporal shape of the emitted photons are important parameters of such sources [130]. The generation of

ultra-long single photons is for example an essential requirement for precise interactions with media exhibiting a sharp energy structure like trapped atoms, ions, or doped solids, which can be used as quantum memories for light [7, 103, 104] and also with cavity opto-mechanical systems [131–135].

Several approaches to achieve narrow linewidth photons have been investigated, including e.g. cavity-enhanced spontaneous parametric down-conversion [136–138], cold atomic ensembles [139–146], single atoms [147, 148], quantum dots [149] or trapped ions [37, 150]. Moreover, significant efforts have been devoted to generate single photons with tunable temporal shapes [72, 144, 150–156] which is important for many applications in quantum information science [157, 158]. However, most of the previous approaches offered only a limited tuning range of the photon duration up to at most one order of magnitude [72, 144, 150].

In this experiment, we demonstrate a single photon source with an unprecedented tuning range of three orders of magnitude, up to single photon durations of 10 μs. To our knowledge, this represents the longest photons generated from an atomic ensemble. Our source is based on a cold atomic ensemble quantum memory (QM) following the DLCZ scheme (cf. subsection 1.2.4) which allows to release the single photons on demand after a programmable delay. This is essential for temporal synchronization tasks as for example needed for quantum repeater architectures [8, 9] or synchronization of photon pair sources [159]. In contrast to most former DLCZ experiments, we apply read-out pulses with very flexible temporal shapes which are accurately controlled over several orders of magnitude in amplitude and time. This enables the generation of ultra-long single photons with very flexible wave shapes and coherence times much longer

than the lifetime of the involved excited state. We characterize the emitted photons by measuring their heralded and unheralded autocorrelation functions, demonstrating a high degree of anti-bunching and purity.

4.2 Experiment description and setup

Our heralded single photon source is based on a laser-cooled ensemble of ^{87}Rb atoms and the DLCZ scheme described in subsection 1.2.4. The Λ-type level scheme that we use consists of a ground state $|g\rangle = |5^2S_{1/2}, F = 2, m_F = 2\rangle$ a storage state $|s\rangle = |5^2S_{1/2}, F = 1, m_F = 0\rangle$ and an excited state $|e\rangle = |5^2P_{3/2}, F = 2, m_F = 1\rangle$ (see Fig. 4.1b). As described in subsection 1.2.4, the detection of a write photon heralds the creation of a spin-wave, which can be later transferred into a single read photon in a well defined spatio-temporal mode. The probability to generate a single read photon once a write photon has been detected is given by the efficiency to retrieve the created spin-wave and map it into a single read photon in a well defined spatial mode. The noise-corrected read-out efficiency is defined as $p_{(\mathrm{r-n})|\mathrm{w}} = (p_{\mathrm{w,r}} - p_{\mathrm{w,nr}})/p_{\mathrm{w}}$, where $p_{\mathrm{w,r}}$ is the probability to detect a coincidence between a write and a read photon, $p_{\mathrm{w,nr}}$ is the probability to detect a coincidence due to background noise and p_{w} is the probability to detect a write photon per trial.

The experimental setup is shown in Fig. 4.1a. To generate the desired laser pulses, the beams are modulated by acousto-optic modulators driven by an arbitrary waveform generator (Signadyne AWG-H3384) with a sampling frequency of 1GS/s and amplifiers (AA Optoelectronic AMPA-B-34). After laser cooling and trapping the atomic cloud, we prepare all the population in the $|g\rangle$ Zeeman sublevel through the optical pumping (OP) process

described in section 3.2. The spin-wave is generated by sending a write pulse of 15 ns duration (full width half maximum FWHM), which is red-detuned by 40 MHz from the $|g\rangle \rightarrow |e\rangle$ transition The heralding write photon is collected at an angle of 1° with respect to the write/read pulse axis. By changing the intensity of the write pulse, we can adjust the probability p_{w} to detect a write photon per trial. For this experiment, p_{w} ranges between 0.25% and 1% depending on the measurement. The read pulse, counterpropagating with the write pulse, is resonant with the $|s\rangle \rightarrow |e\rangle$ transition and its temporal shape can be precisely controlled. The read photon is collected in the same spatial mode but opposite direction of the write photon. By measuring the transmission of classical light sent through the write/read photons axis and by comparison of experimental and theoretical data in Fig. 4.2 and Fig. 4.5, we infer a coupling efficiency of the read photon into the first fiber of $\eta_{\mathrm{fiber}} \approx 60\%$. The polarization of the write and read pulses in the frame of the atoms is σ^- and σ^+ respectively, while the detected write and read photons are σ^+ and σ^- polarized. In order to filter the write and read photons from any noise, we use the polarization and frequency filtering methods described in section 2.3. The filtering cavities have $\eta_{\mathrm{filter}} \approx 20\%$ total transmission (including cavity transmission and subsequent fiber coupling), and we use single photon detectors (SPDs) with $\eta_{\mathrm{det}} = 43\%$ efficiency and a dark count rate of 130 Hz.

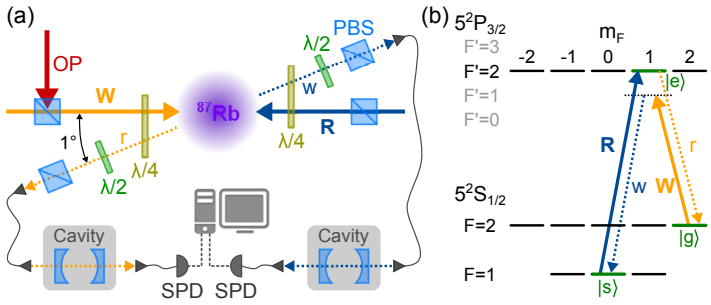

FIGURE 4.1: Experimental setup and level scheme. (a) Experimental setup. Write pulse (W) and Read pulse (R) are sent counter-propagating into the atomic cloud. Write and read photons (denoted by w and r) are sent after polarization filtering via fibers to frequency filtering cavities before being detected by single photon detectors (SPD). (b) Energy levels of the D2 line of ^{87}Rb and coupling scheme for the DLCZ experiment.

4.3 Results

4.3.1 Tunability of the single photon temporal width

In this section, the experimental results are presented and compared to detailed theoretical calculations. To generate read photons of variable length, we change the duration of the Gaussian-shaped read pulse as well as the storage time over several orders of magnitude (see Fig. 4.2). The shortest read pulse duration of approximately 17 ns leads to a read photon of around 23 ns duration. After that initial data point, we observe a quite linear increase of the read photon duration with the read pulse duration up to several tens of microseconds. The lower limit of photon duration is given by the limited optical depth OD = 5.5 in our experiment which leads to limited superradiant emission of the read photon [160]. A further technical limitation is given by the finite bandwidth of the spectral filtering cavity of about 60 MHz which additionally increases the detected duration for short read photons. This effect, together with the deviation from the adiabatic condition, partly explains the slight difference of the

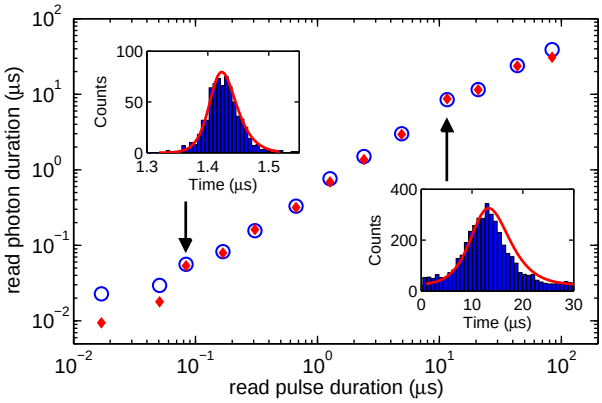

FIGURE 4.2: Temporal duration (FWHM) of the read photon vs the duration of the driving read pulse. Experimental data (blue circles, error bars smaller than symbol size) are compared with numerical simulations (red diamonds). The insets show two examples of the read photon wave shape as reconstructed from the number of counts and arrival times in the SPDs (blue histograms) as well as the simulated wave shapes (red lines) for which we allowed at most 10% adjustment of the input parameters to account for experimental inaccuracies.

first data points in Fig. 4.2 from the theoretical prediction (see below). The upper limit of photon duration is given by the spin-wave linewidth which is mainly determined by thermal atomic motion and spurious external magnetic fields. This currently limits the maximal storage time in the memory to about 60 μs (as shown later in Fig. 4.3b). In addition, the photon duration will also be limited by the coherence time of the read laser which has a specified linewidth of 20 kHz. However, within the above limits we demonstrate that the photon duration is fully tunable and that the Gaussian wave shape of the driving read pulse is preserved in the read-out process (see insets).

The dynamics of the write and read photon pairs is modeled using the Heisenberg-Langevin equations. For slowly varying optical fields propagating in a pencil-shaped atomic ensemble, explicit expressions for both the

write and read photon fields can be obtained in the adiabatic approximation [161]. These field expressions can be subsequently used to reproduce the read photon emissions conditioned on the detection of a write photon from first and second order correlation functions (see Appendix G.1) . The result of these simulations which are based on independent measurements reproduce very well the experimental data presented in Fig. 4.2.

To characterize the read-out efficiency of the photon source, we optimized the intensity of the driving read pulse for each duration (see Appendix G.2). Fig. 4.3a shows the highest achievable fiber-coupled read-out efficiency $p^{\text{fiber}}_{(\text{r}-\text{n})|\text{w}} = p_{(\text{r}-\text{n})|\text{w}} / (\eta_{\text{filter}} \cdot \eta_{\text{det}})$ vs the read photon duration, which corresponds to the probability of finding a read photon in the optical fiber after the vacuum cell (i.e. corrected for filtering and detector efficiencies only). We observe a constant read-out efficiency of about $p^{\text{fiber}}_{(\text{r}-\text{n})|\text{w}} = 20\,\%$ up to a read photon duration of approximately $10\,\mu$s. Our numerical simulations match very well with the experimental data and also show that the efficiency in the constant region is just limited by the finite OD of our atomic cloud. We verify numerically that in the absence of technical noise and considering infinite spin-wave coherence, for OD = 50 an intrinsic read-out efficiency of 80% can be achieved while maintaining control of the photon shape. The decrease of the efficiency at around $10\,\mu$s is due to dephasing of the spin-wave induced by atomic motion, spurious external magnetic field gradients (cf. Appendix D), and the finite read laser coherence time. This dephasing is characterized in Fig. 4.3b, which shows the read-out efficiency as a function of the storage time using short read pulses ($\Delta t_{\text{FWHM}} = 35\,\text{ns}$). Our numerical simulations show clearly that in the absence of technical noise and in the limit of infinite spin coherence, the efficiency is kept constant (see orange diamonds and dashed line in Fig. 4.3a).

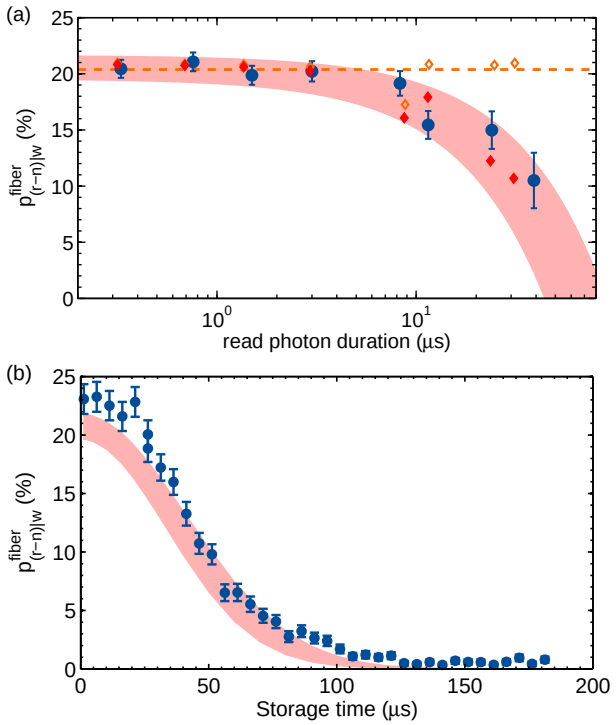

FIGURE 4.3: Readout efficiency. Fiber-coupled readout efficiency $p^{\text{fiber}}_{(\text{r}-\text{n})|\text{w}}$ vs the read photon duration (FWHM) in (a) and the storage time in(b), for $p_{\text{w}} = 0.5\%$. Experimental data (blue dots) are compared with numerical simulations (see Appendix G.1) for realistic (red diamonds) and ideal (orange diamonds) conditions. The red shaded area depicts the expected range if the input parameters of the simulation are varied by ±10%. The data in (b) correspond to a read pulse duration of $\Delta t_{\text{FWHM}} = 35\,\text{ns}$. The error bars (±1 s.d.) correspond to the propagated Poissonian error of the photon counting statistics.

4.3.2 Photon state statistics

Next, we characterized the state of the emitted read photons by measuring their heralded and unheralded second order autocorrelation functions depending on the read photon duration. To perform these measurements, we inserted a balanced fiber-beamsplitter into the read photon arm after the spectral filtering cavity, with both output ports connected to single photon detectors r1 and r2. First, we recorded the autocorrelation function

conditioned on the detection of a write photon, defined as [162]:

$$g^{(2)}_{\mathrm{r1,r2|w}} = \frac{p_{\mathrm{r1,r2|w}}}{p_{\mathrm{r1|w}} \cdot p_{\mathrm{r2|w}}} \tag{4.1}$$

where $p_{\mathrm{r1,r2|w}}$ denotes the probability to measure a coincidence between both read photon detections conditioned on a write photon detection, and $p_{\mathrm{r1|w}}$, $p_{\mathrm{r2|w}}$ are the probabilities to detect a read photon via r1 or r2 conditioned on a write photon detection. The data shown in Fig. 4.4a, clearly demonstrate the non-classicality of the photons (i.e. $g^{(2)}_{\mathrm{r1,r2|w}} < 1$ as explained in Appendix B) up to photon durations of more than 10 μs. However, we don't reach the ideal value of $g^{(2)}_{\mathrm{r1,r2|w}} = 0$ of perfect single photons. For short read photon durations we are still limited by noise due to higher order components of the spin-wave which can be addressed by reducing p_{w} (cf. Appendix B.2). In fact, the observed $g^{(2)}_{\mathrm{r1,r2|w}} \approx 0.4$ is consistent with former measurements at similar values for p_w and read pulse durations [120]. For longer read photon durations we observe an increase of $g^{(2)}_{\mathrm{r1,r2|w}}$ which can be simply explained by a higher number of dark counts of the SPDs for longer read photon detection gates (see upper axis in Fig. 4.4). The solid blue line shows the prediction of a non-perturbative theoretical model accounting for detector imperfections [119]. The agreement between the model and the experimental data is very good. For this data set the photon rates were the following: $\sim 65\,\mathrm{Hz}$ for the detected write photons, $\sim 22\,\mathrm{Hz}$ for the generated heralded read photons (considered right after the atomic cloud), and $\sim 1.1\,\mathrm{Hz}$ for the detected heralded read photons. These rates did not change significantly as a function of the photon's duration thanks to the FPGA-based feedback protocol that we used: the read pulse was sent only after a write photon was detected.

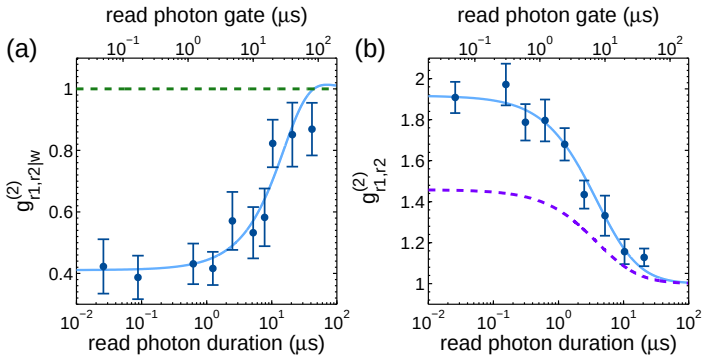

FIGURE 4.4: Measurement of correlation functions. Second order autocorrelation function of the generated read photons, (a) conditioned on the detection of a write photon in the same experimental trial at $p_w = 0.25\%$ and (b) not conditioned on a write photon detection at $p_w = 1\%$. The experimental data (blue dots) are compared with a theoretical model accounting for detector imperfections, i.e. a measured dark count rate of 130 Hz (blue lines). The dashed green line in (a) represents the classical bound of a coherent state and the dashed purple line in (b) shows the expected trace for a photon state with two modes.

The single mode nature of the photon state is characterized by the unconditional autocorrelation function $g^{(2)}_{r,r}$ (see Fig. 4.4b). For an ideal two mode squeezed state, where the write and read photons are each emitted in a single temporal mode, one expects $g^{(2)}_{r,r} = 2$ (cf. Appendix A.2.2) which is quite well fulfilled by the measured data up to a read photon duration of roughly 1 μs. For longer durations, we observe a drop which can be attributed to either an increasing temporal multimodality of the read photon ($g^{(2)}_{r,r}$ scales as $1 + 1/K$ with K denoting the number of photon modes [163]) or to measurement imperfections because of higher dark counts for larger detection gates. The solid blue line shows the theoretical prediction, assuming read photons emitted in a single mode. The excellent agreement between experiment and theory suggests that the read photons are emitted mostly in a single mode. For comparison, we also plotted the expected behaviour for a single photon with $K = 2$ modes (see purple dashed line) which significantly differs from the measured data, therefore confirming

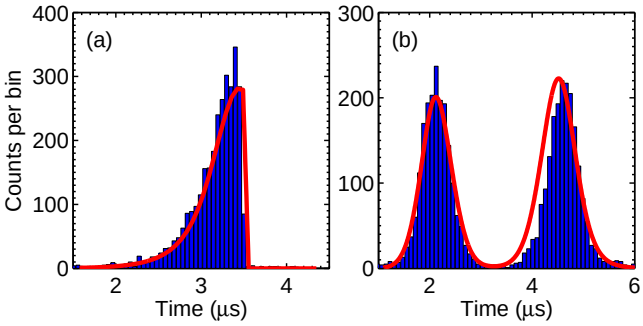

FIGURE 4.5: Single photons with non-standard wave shapes. Temporal wave shape of the read photon for (a) a rising exponential and (b) a doubly peaked read pulse wave shape. Experimental data (blue histograms) are compared with numerical simulations (red line) for which we allowed at most 10% adjustment of the input parameters with respect to the measured data. Both histograms were taken at $p_w = 0.5\%$.

the single mode nature of the emitted read photons. Consequently, the read photons are close to be Fourier transform limited, giving linewidths ranging from around 20 MHz to less than 100 kHz. This, together with the conditional $g^{(2)}_{r1,r2|\omega}$, allows us to conclude that the heralded read emission is close to a pure single photon.

4.3.3 Photons with non-standard waveforms

Finally, we investigate the flexibility of the temporal shape of the generated read photons. Instead of a Gaussian shaped read pulse, we apply read pulses with a rising exponential envelope or a doubly peaked wave shape. These two examples are important for a broad class of applications in quantum information science. Photons with rising exponential wave shape exhibit the highest possible absorbance when interacting with two-level systems [157, 164] and can be very efficiently loaded in optical cavities [158, 165]. The temporal shape of the generated rising exponential read photon is shown in Fig. 4.5a. The driving read pulse had a $1/e$ width of

300 ns. We observe a similar read-out efficiency of $p^{\text{fiber}}_{(\text{r}-\text{n})|\text{w}} = 19.8\%$ as for a standard Gaussian shaped pulse of same duration (cf. Fig. 4.3). The conditioned autocorrelation function of the rising exponential photon is $g^{(2)}_{\text{r1,r2}|\text{w}} = 0.31 \pm 0.14$ (taken at $p_{\text{w}} = 0.25\%$) and $g^{(2)}_{\text{r1,r2}|\text{w}} = 0.73 \pm 0.12$ (taken at $p_{\text{w}} = 0.5\%$) which is clearly in the nonclassical regime.

As a final example, we send a doubly peaked read pulse into the prepared QM. The intensity and duration of the first read-out peak was chosen such that the stored spin-wave is read-out with half of the maximal efficiency and for the second peak the read-out efficiency is maximized. This leads to a read photon with a shape shown in Fig. 4.5b. Photons with such a delocalized shape can be used to create time-bin qubits which have applications in robust long distance quantum communication [99, 166]. The efficiency of the generated double time-bin photon is $p^{\text{fiber}}_{(\text{r}-\text{n})|\text{w}} = 25\%$, comparable to the standard Gaussian shaped photons, and the conditioned autocorrelation function is $g^{(2)}_{\text{r1,r2}|\text{w}} = 0.54 \pm 0.11$ (taken at $p_w = 0.25\%$) and $g^{(2)}_{\text{r1,r2}|\text{w}} = 0.75 \pm 0.08$ (taken at $p_{\text{w}} = 0.5\%$) which is clearly in the nonclassical regime.

4.4 Discussion

We demonstrated a highly flexible heralded single photon source with intrinsic storage capability following the DLCZ scheme in a cold ^{87}Rb ensemble. Compared to other approaches for narrowband single photon generation, such as cavity enhanced spontaneous parametric down conversion [136–138], single atoms and ions in cavities [37, 147, 148, 150] and four-wave mixing in atomic ensembles [144, 146], our single photon source offers an unprecedented photon duration tunability of three orders of magnitude

and the possibility to generate photons of highly flexible wave shape and an efficient emission on a single spatial and temporal mode without the need of a high-finesse cavity.

Another important feature of our approach is that our single photon source has intrinsic storage capability which naturally enables synchronization with other identical sources. In the following, we discuss that possibility with our current setup. A deterministic synchronization of two such sources depends on the average time separation between successful heralding events (write photon detections) and the maximal storage time of the source. The time between heralding events depends on several parameters: First, the power of the write pulse determines the probability p_{w} and hence the detection rate of the Raman scattered write photons. However, one cannot just arbitrarily increase the write power to increase that rate because it would also lead to a degradation of the non-classical correlations between both photons. Second, the various losses from the vacuum cell towards the final detection (mainly fiber-coupling, filtering, and detector efficiencies) decrease the probability and hence the rate to detect an emitted write-photon quite significantly (factor ~ 20). However, these are mainly technical issues which could be improved by better equipment.

In our experiment we typically operate the single photon source with a p_{w} of around 0.5%. Using a heralded sequence (i.e. sending the read pulse only when a write photon was detected) we can generate 500 trials per 1 ms interrogation time for read photon lengths of a few μs, which gives an average time separation between heralding events of 400 μs. This is of course much longer than the current storage time of about 50 μs and would not allow for a deterministic synchronization of two single photon sources with the current status of the experiment.

However, note that, first, it is not necessary to be in the regime where the storage time is longer than the delay between two write photon detection to start gaining with the quantum memory. The important parameter is the number of write attempts that can be done during the storage time [167, 168]. Even with the current setup ($N \approx 25$ trials per 50 μs storage time) we would reduce the synchronization time between two sources by a factor $2N + 1 \approx 50$ compared to single shot attempts [167]. Second, with quite moderate improvements (a storage time of 1 ms [54, 68] and a filtering efficiency of $\eta_{\text{filter}} = 80\%$), the time separation between heralding events would be 100 μs, which would be ten times shorter than the storage time, immediately enabling the deterministic synchronization of several single photon sources.

4.5 Conclusions

In conclusion, we demonstrated a highly flexible single photon source with intrinsic storage capability following the DLCZ scheme [12] in a cold ^{87}Rb ensemble. By varying the temporal width of the driving read pulse, the duration of the read photons could be changed over three orders of magnitude up to several tens of μs. Up to a read photon duration of 10 μs, we obtain a fiber-coupled read-out efficiency of $p^{\text{fiber}}_{(\text{r}-\text{n})|\text{w}} = 20\%$. We simulated numerically that for OD = 50 under ideal conditions, an intrinsic read-out efficiency of 80% can be achieved while maintaining control of the photon shape, but this has still to be measured experimentally. The drop in read-out efficiency at around 10 μs is mainly due to spin-wave dephasing induced by thermal motion, which could be improved by a more sophisticated trapping of the atoms [54, 72]. The generated read photons show a nonclassical behaviour up to durations of more than 10 μs for the

heralded autocorrelation function and up to 1 μs we detect single photons in a pure state, currently just limited by the dark counts of our detectors. Finally, we create single photons with a non-standard envelope like rising exponential or time-bin wave shapes, which have important applications in quantum information science. Our approach allows the generation of ultra-narrow single photons with unprecedented duration tunability and highly flexible wave shape. This will enable the interconnection of our cold atom quantum memory with other physical systems exhibiting sharp resonances, e.g. Rb atoms prepared in a highly excited Rydberg state under the condition of EIT. This particular example is shown in section 6.1. Moreover, combining our approach with the quantum frequency conversion technique explained in chapter 3 paves the way to the optical interconnection of the cold atom quantum memory with different types of quantum systems which typically demand very different photon shapes, like long-lived solid state quantum memories or opto-mechanical systems. Finally, also applying the ability to generate single photons with doubly-peaked wave-shapes (as shown in Fig. 4.5 b), one could demonstrate quantum state transfer via time-bin qubits between different systems, which would be an important step towards the creation of heterogeneous quantum networks [169]. This hybrid quantum state transfer is later shown in section 6.2.

Chapter 5

Entanglement between a photonic time-bin qubit and a collective atomic spin excitation

The results presented in this chapter have been published in [170], and the text is mostly adapted from the publication.

5.1 Introduction

As mentioned in section 1.3, entangled states between light and matter play a central role both for fundamental tests and technological applications of quantum physics [14, 35, 171, 172]. Several degrees of freedom can be used to encode the photonic component of the light-matter entangled

state: polarization [14–18, 21, 77, 172], orbital angular momentum [79], spatial [78] or time-bin encoding [19, 20, 35] being the most prominent examples. For long distance transmission, encoding in the form of photonic time-bin qubits is favourable, since this approach is robust against decoherence in optical fibers. The good performance of time-bin photonic states has been shown in several works including long distance entanglement distribution or teleportation [100, 173–175]. The direct generation of time-bin entanglement between a photonic qubit and a matter system (i.e. without the need of an external quantum light source) has, so far, been shown only in single emitter systems such as nitrogen vacancy centers [35] or quantum dots [23].

In this experiment, we demonstrated the direct generation of entanglement between a photonic time-bin qubit and a collective atomic spin excitation (spin-wave) using an ensemble of laser-cooled atoms. In contrast to former related experiments, in our system, the atomic state can be very efficiently mapped later into a single photon without the need of high finesse cavities [68, 73]. Moreover, the ensemble based approach offers excellent prospects for different multiplexing techniques [9, 80, 85, 86]. The combination of the spin-wave to photon conversion capability together with the time-bin encoding makes our system a source of entangled photonic qubits that are robust and synchronizable. These capabilities provide an interesting resource, for instance, for long distance quantum communication using quantum repeaters [9, 12].

5.2 Experiment description and results

The basic concept of the experiment is as follows (cf. Fig. 5.1). An off-resonant doubly-peaked write laser pulse generates an excitation in our atomic cloud that is entangled with a Raman scattered write photon in the time-bin degree of freedom. In order to generate this entangled state, the atomic excitations generated at the two time bins need to form an orthogonal qubit basis (i.e. they need to be totally distinguishable). This is achieved applying a homogeneous magnetic field that leads to a Zeeman splitting of the atomic energy levels and induces a dephasing and rephasing of the atomic excitation at well defined times after its creation [142] (see Fig. 5.1b and 5.1c). To assess the matter qubit, this is subsequently converted into a photonic time-bin qubit using a resonant read laser pulse, and the two entangled photons are analysed. This analysis is done with Mach-Zehnder interferometers and single photon detectors, which allow projective measurements in any basis on the equator of the Bloch sphere.

5.2.1 Experimental setup and procedure

The experimental setup is shown in Fig. 5.1a. We cool our ensemble of ^{87}Rb atoms in the magneto-optical trap to $T \approx 100\,\mu$K. The atomic levels relevant for the experiment are shown in Fig. 5.1b and consist of two metastable ground states ($|g\rangle = |5^2S_{1/2}, F = 1\rangle$ and $|s\rangle = |5^2S_{1/2}, F = 2\rangle$) and one excited state ($|e\rangle = |5^2P_{3/2}, F = 2\rangle$). A homogeneous magnetic field ($B = 0.67\,$G) perpendicular to the beam propagation axis splits the energy of the Zeeman sublevels, which is essential for the entanglement generation as discussed below. After optically pumping the atoms in state $|g\rangle$, a write pulse drives transition $|g\rangle \rightarrow |e\rangle$ with a red detuning

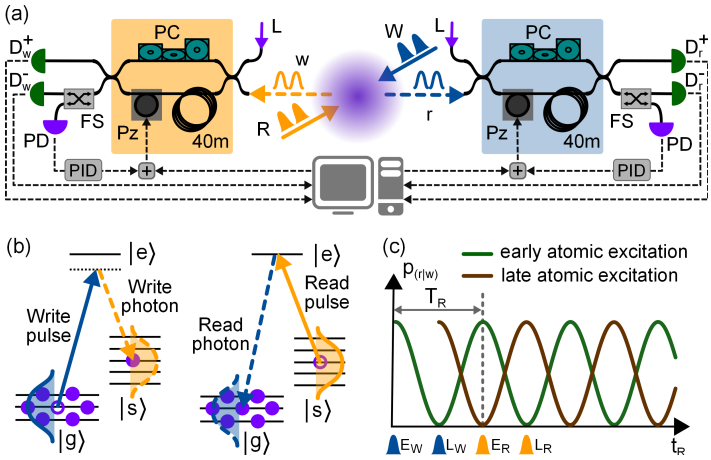

FIGURE 5.1: (a) Schematic overview of the experimental setup. W, write pulse; R, read pulse; w, write photon; r, read photon; L, interferometer lock light; PC, polarization controller; Pz, piezo-electric fiber stretcher; $D^{+(-)}_{w(r)}$, single photon detectors; FS, fiber switch; PD, photodiode; PID, proportional-integral-derivative controller. (b) Energy levels relevant for the photon generation process. (c) Expected behaviour of the read photon transfer efficiency of the early (green) and late (brown) atomic excitations as a function of the read-out time t_R. The blue pulses indicate the times of the early (E_W) and late (L_W) write pulse peaks required to create the light-matter entangled state. The orange pulses indicate the times of the early and late read pulse peaks (E_R and L_R) required to subsequently convert the atomic qubit into a read photon time-bin qubit.

of $\Delta = 40$MHz. This process generates probabilistically write photons on the $|e\rangle \rightarrow |s\rangle$ transition through spontaneous Raman scattering. The write pulse interacts with many atoms at different positions and in different Zeeman sublevels. Hence, the state of the atomic excitation is a collective state given by the superposition of all possible excitations (cf. subsection D.1.2 and [120]). Because of its temporal evolution, the state can be written after a certain time t as

$$|\Psi_a(t)\rangle = \frac{1}{\sqrt{N}} \sum_{j=1}^{N} e^{i(\mathbf{k}_W - \mathbf{k}_w)\mathbf{x}_j + i\Delta w_j t} |g_1 ... s_j ... g_N\rangle \tag{5.1}$$

where N denotes the total number of atoms, $\mathbf{x}_j$ the initial atom position, Δw_j the two photon detuning of the excitation and $\mathbf{k}_{\mathrm{W(w)}}$ the wave vector of the write pulse (photon).

The collective atomic excitation can be converted into a read photon by means of a read pulse resonant to the $|s\rangle \rightarrow |e\rangle$ transition. In the absence of atomic dephasing the transfer will happen with a high efficiency to a particular spatio-temporal mode thanks to collective interference of all contributing atoms. This read-out efficiency can be measured as the probability $p_{\mathrm{r|w}}$ to detect a read photon once a write photon was detected, and is shown in Fig. 5.2a as a function of the read-out time t_{R} if no external magnetic field is applied (green open circles). In the presence of dephasing of the atomic state, the collective interference will be degraded and the photon retrieval efficiency will decrease. In our case, the magnetic field splits the Zeeman sublevels, giving rise to four different excitation paths of the spin-wave with different two-photon detunings $\Delta\omega_j$ (cf. Appendix H.1). According to Eq. (5.1), this leads to a periodic dephasing and rephasing of the atomic excitation that we observe as a beating of the read-out efficiency with a periodicity of $T_{\mathrm{r}} = 344\mathrm{ns}$. This effect is schematically represented in Fig. 5.1c and the measured data are shown in Fig. 5.2a (blue dots). A theoretical model of $p_{\mathrm{r|w}}$ can be developed by computing the overlap between the initial atomic state and the state at the read-out time $p_{\mathrm{r|w}}(t_{\mathrm{R}}) \propto |\langle \Psi_{\mathrm{a}}(t=0)|\Psi_{\mathrm{a}}(t=t_{\mathrm{R}})\rangle|^2$. This expression is used to obtain the equation with which the data in Fig. 5.2a are fitted (cf. Appendix D.1.2 and Appendix H.1).

The way we generate the entanglement with time-bin encoding is as follows. A write pulse with two intensity peaks separated by $T_{\mathrm{r}}/2$ is sent to the atoms, leading to the probabilistic generation of a photon-atomic

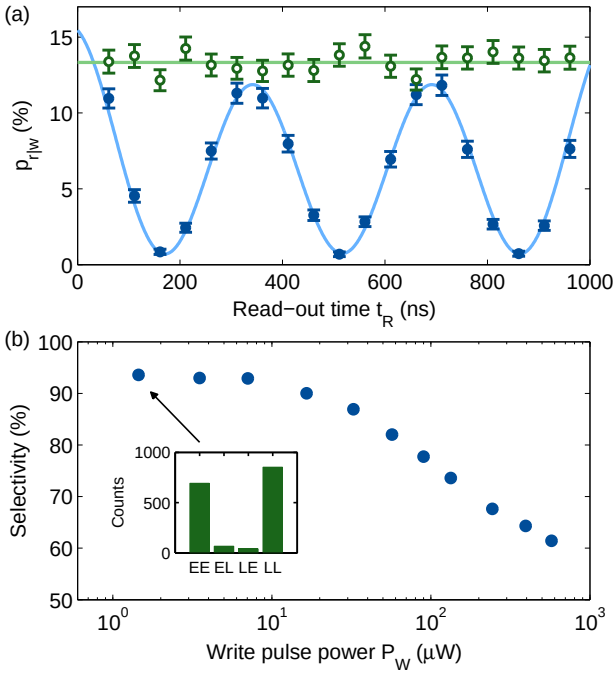

FIGURE 5.2: (a) Measured read photon transfer efficiency of the atomic excitation as a function of the read-out time. The green open circles show the case without magnetic field dephasing, while the blue dots show the case with the magnetic field on. For both traces the write (read) detection gates are 40 ns (60 ns) and the data are only corrected for the SPD detection efficiency. (b) Atomic excitation read-out selectivity as a function of the write pulse power. Here, the write and read detection gates were set to 30 and 40 ns, respectively. The error bars are smaller than the size of the data points. The inset shows the time-bin correlation for one particular write pulse power. Error bars correspond to ± 1 standard deviations of the photon counting statistics.

excitation pair delocalized in two time-bins. This time-bin entangled state can be written as

$$|\Psi_{\mathrm{wa}}\rangle = \frac{1}{\sqrt{2}}\left(|\mathrm{E_wE_a}\rangle + \mathrm{e}^{\mathrm{i}\phi}\,|\mathrm{L_wL_a}\rangle\right) \tag{5.2}$$

where $|\mathrm{E_{w(a)}}\rangle$ and $|\mathrm{L_{w(a)}}\rangle$ denote a write photon (atomic excitation) generated in the early and late bin, respectively. The generation time difference of the atomic states $|\mathrm{E_a}\rangle$ and $|\mathrm{L_a}\rangle$ leads to a different phase evolution of

these two spin-wave modes in such a way that they become distinguishable. The phase ϕ of the entangled state $|\Psi_{\mathrm{wa}}\rangle$ depends on the phase difference between the two write pulse peaks.

5.2.2 Atom-to-photon transfer of the atomic quantum state

Because of the mentioned collective interference, the atomic qubit can be later transferred into a photonic qubit via a resonant read pulse. This pulse needs to have two intensity peaks separated by $T_{\mathrm{r}}/2$ and delayed by a multiple of T_{r} with respect to the early atomic excitation creation time (cf. Fig. 5.1c). In that situation, thanks to the magnetic field dephasing, the early peak of the read pulse will transfer collectively only early atomic excitations into early read photons. In the same way, the late peak of the read pulse will transfer collectively only late atomic excitations into late read photons. One detrimental effect is that the early read pulse also scatters late atomic excitations, which leads to the non-directional emission of photons. For this reason the early read pulse has an area of $\pi/2$, while the area of the late read pulse is π. This intrinsically limits the atom-to-photon state transfer to an efficiency of 50% in the current configuration. This read-out imperfection is equivalent to a loss induced by a beam splitter. This issue could be overcome by an alternative scheme that transfers the early or late atomic excitations back and forth to different ground-state levels, such that during the write and read-out processes just one component of the spin-wave interacts with the optical pulses [176].

To demonstrate that the generated write and read-photons are indeed correctly correlated in the time-bin degree of freedom, we construct the coincidence histograms of detection events, using just one write and one read photon detector after the ensemble. The inset in Fig. 5.2b shows

the number of coincidences between write and read photons in each of the bins $C_{b_\mathrm{w} b_\mathrm{r}}$, where $b_{\mathrm{w(r)}}$ denotes the early or late write (read) photon bin. For low P_W, most of the photons are detected together in either the early or the late time bin. However, for higher write powers, the degree of correlation decreases, due to the creation of multiple spin-wave photon pairs. The green data points show the degree of correlation depending on the the write power — illustrated by the selectivity parameter $\mathrm{SE} = (C_\mathrm{EE} + C_\mathrm{LL}) \,/\, (C_\mathrm{EE} + C_\mathrm{LL} + C_\mathrm{EL} + C_\mathrm{LE})$. One limitation in the upper limit of the measured values of SE is given by the temporal duration of the photons (in our experiment the write and read photons have durations $\Delta t_\mathrm{w} = 20\,\mathrm{ns}$ and $\Delta t_\mathrm{r} = 30\,\mathrm{ns}$ considering the FWHM). If Δt_w and Δt_r are not sufficiently small compared to T_r this can lead to an imperfect dephasing and rephasing of the spin-wave.

5.2.3 Quantum state analysis and entanglement verification

To characterize the generated quantum state and certify the entanglement, we took projective measurements on the equator of the Bloch sphere. This is done by overlapping the early and late bins of both write and read fields using fiber Mach-Zehnder interferometers as shown in Fig. 5.1a. The length difference between the short and long arm of each interferometer is 40 m, corresponding to the temporal separation between the early and late bins. This large imbalance makes it experimentally challenging to maintain a stable phase difference between the two arms of each interferometer during the whole experiment. The details on how this is achieved are mentioned in section 2.5.

Figure 5.3a shows the write and read photon time histograms after passing through the interferometers. For both histograms, the first peak corresponds to photons generated in the early bin that pass through the short interferometer arm. The third peak corresponds to photons generated in the late bin that pass through the long interferometer arm. The central peak corresponds to photons that are either created in the early bin and pass through the long interferometer arm or are created in the late bin and pass through the short interferometer arm. These events correspond to qubit projections into states that lay on the equator of the Bloch sphere expressed as $1/\sqrt{2}(|E\rangle + e^{i\phi}|L\rangle)$ [99, 100] (see Fig. 5.3b). The phase ϕ corresponds to the phase delay between the two interferometer arms, and can be controlled by changing the voltage $U_{\mathrm{w(r)}}$ sent to the write (read) piezoelectric fiber stretcher. In Fig. 5.3c we show the correlation coefficient E as a function of U_{r}, defined as $E = (p_{++} - p_{+-} - p_{-+} + p_{--})/(\sum_{i,j} p_{i,j})$. Here, $p_{i,j}$ correspond to the probabilities of detecting a photon coincidence between detectors $\mathrm{D}^i_{\mathrm{w}}$ and $\mathrm{D}^j_{\mathrm{r}}$ $(i, j = \pm)$, within the central peaks shown in Fig. 5.3a. For two different U_{w}, we measure two-photon interference fringes that are shifted by $82(5)^\circ$ with visibilities of $V_1 = 0.82(0.04)$ and $V_2 = 0.79(0.04)$. These values reveal the presence of entanglement, since they are above the visibility required for a Bell inequality violation $(V > 1/\sqrt{2} \approx 0.707)$.

Besides the two-photon interference shown in Fig. 5.3c, we also observe low visibility single-photon interference of each write and read photon (cf. Appendix H.2). This is due to the emission of photons in other transitions that do not correspond to entangled events, which could be avoided by spectral filtering. However, these uncorrelated write-read photons have a very low impact on $E(U_{\mathrm{w}}, U_{\mathrm{r}})$.

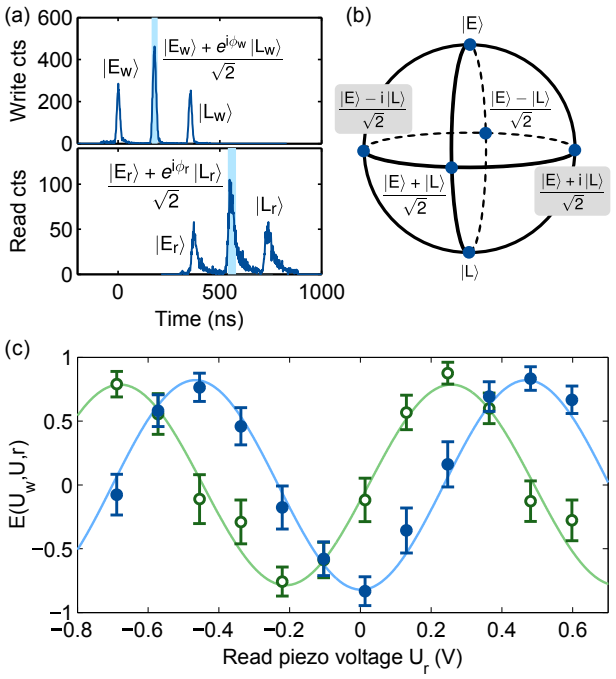

FIGURE 5.3: Quantum state analysis. (a) Write and read photon histograms at the interferometer outputs (photon durations are 20 ns and 30 ns FWHM, respectively). The detection events in each of the bins correspond to a projection to a different state as indicated in the figure. (b) Representation of the different orthogonal time-bin states on the Bloch sphere. (c) Write-read photon correlation coefficients taken at $P_W = 7\,\mu$W. The phase of the read photons interferometer is scanned, while the phase of the write photons interferometer is fixed at two different values ($U_{w1} = 0$ V for the blue dots and $U_{w2} = 0.268$ V for the green open circles). The detection gate widths were set to 30 ns for the write photons and 40 ns for the read photons (cf. blue area in (a)).

The visibility of the two-photon interference fringes (as shown in Fig. 5.3c) is plotted as a function of the write pulse power in Fig. 5.4a. V decreases for high P_W due to the creation of multiple photon-atomic excitation pairs during the write process [18]. This leads to the detection of coincidences coming from photon pairs that are not entangled. The measured data show that we can fulfill the condition of Bell inequality violation ($V > 1/\sqrt{2}$) for $P_W < 15\,\mu$W, reaching a maximum value of $V = 0.93(5)$. To

definitely prove the entanglement we violate a Clauser-Horne-Shimony-Holt (CHSH)-type Bell inequality [177], which reads

$$S = \left|E(\phi_{\mathrm{w}}, \phi_{\mathrm{r}}) + E(\phi_{\mathrm{w}}, \phi'_{\mathrm{r}}) + E(\phi'_{\mathrm{w}}, \phi_{\mathrm{r}}) - E(\phi'_{\mathrm{w}}, \phi'_{\mathrm{r}})\right| \leq 2 \tag{5.3}$$

where $\phi_{\mathrm{w(r)}}$ and $\phi'_{\mathrm{w(r)}}$ are pairs of write (read) photon interferometer phases. In Fig. 5.4b we show the four correlation coefficients taken with the basis that lead to the highest possible value of S. The measurement gives a CHSH Bell parameter of $S = 2.18 \pm 0.09$, violating the Bell inequality by 2 standard deviations. Possible limitations of this value include laser frequency fluctuations (cf. Appendix E), the detection of photons emitted in other transitions (cf. Appendix H.2) and the imperfect spin-wave dephasing due to the non-zero photon temporal widths.

5.3 Bell test with human random numbers

This experiment was also used to participate in a big project called "Big Bell Test" [178]. The main motivation for this project was to use human "free will" to assure unpredictability in the measurement settings of Bell tests. This is very important in loophole-free Bell tests, since it is required to address the freedom-of-choice loophole. Our experiment was one of the 13 experiments that participated in this project. More that 100,000 participants used a on-line video game and produced around 10,000,000 binary choices. These random numbers were then distributed along the different labs and used to decide the measurement settings. Different entangled systems were used for the test, including photon-photon, photon- single atom, transmon qubits, and our photon-atomic ensemble experiment.

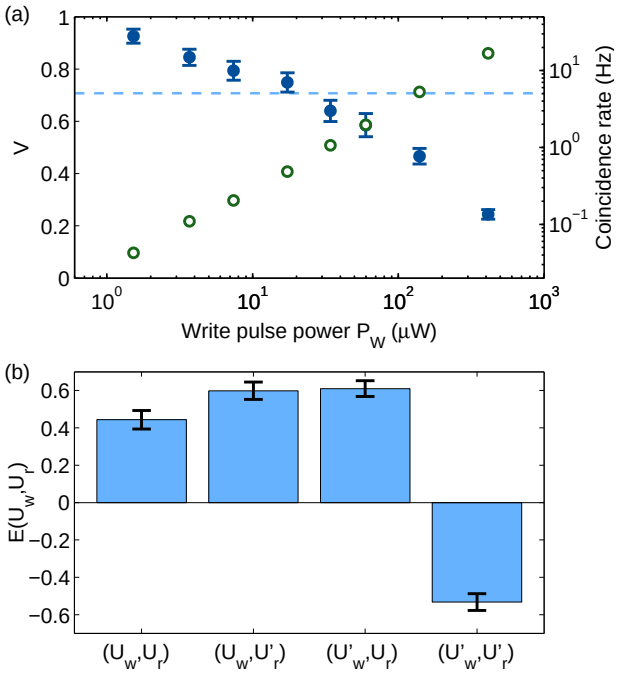

FIGURE 5.4: Entanglement verification. (a) Visibility of the two-photon interference fringes as shown in Fig. 5.3c (blue dots) and detected photon coincidence rate (green open circles) versus write pulse power. The dashed line represents the visibility required to violate a Bell inequality ($V > 1/\sqrt{2}$). (b) Values of the four correlation coefficients taken at $P_{\mathrm{W}} = 3.5\mu\mathrm{W}$ and with the four basis settings ($U_{\mathrm{w}} = 0.268\,\mathrm{V}$, $U'_{\mathrm{w}} = 0\,\mathrm{V}$, $U_{\mathrm{r}} = 0.333\,\mathrm{V}$, and $U'_{\mathrm{r}} = 0.099\,\mathrm{V}$) that are optimal for a Bell inequality violation.

In our experiment, the random numbers generated by the participants of the Big Bell Test were used to decide which voltage is applied to each interferometer, hence controlling the measurement bases. Trapped atom clouds were created at a rate of 59 Hz. For each cloud, we performed 608 entanglement trials. The bases were changed in between each cloud and not between each single trial because of the limited bandwidth of the piezoelectric fiber stretcher. However, the typical write-read photon coincidence detection probability per trial $p(\phi_{\mathrm{w}}, \phi_{\mathrm{r}})$ was between 10^{-6} and 10^{-5}. We can therefore say that for each detected coincidence event, the bases were chosen randomly.

During the time window of the Big Bell Test (on November 30$^{\text{th}}$, 2016) we used the live human random numbers to randomly choose between predefined phases in the two analysing interferometers to take the data shown in Fig. 5.2a. Here, the photon coincidence probability p_{++} is plotted as a function of $U_r \propto \phi_r$ for two different values of $U_{\text{w}} \propto \phi_{\text{w}}$. The two fringes are shifted by 114(9) degrees exhibiting visibilities of $V_1 = 0.72(0.08)$ (blue dots) and $V_2 = 0.63(0.10)$ (green circles). These visibilities are sufficient to prove entanglement between both time-bin qubits, as follows from the Peres separability criterion ($V > 1/3$) under the assumption of equally distributed noise for all possible outcomes [179]. However, the values did not surpass the threshold of $V > 1/\sqrt{2} \approx 0.707$ to guarantee Bell-type non-local correlations. We obtained similar visibilities without the use of human random numbers, which confirmed that the measurements were affected by experimental instabilities during the required relatively long integration times of several hours.

After improving the long-term stability of the experiment, we redid a Bell test at a later stage with human random numbers received and stored during the day of the Big Bell Test. Here, the human random numbers were used to switch randomly between the four settings required for the measurement of the CHSH inequality. The experimental results of that Bell Test are show in Fig. 5.2b. The data acquisition lasted 3 hours and 26 minutes, during which we performed 364800000 experimental trials. In this time we recorded 1100 photon coincidence events which led to a final CHSH Bell parameter of $S = 2.29 \pm 0.10$. This measurement shows a violation of the Bell inequality surpassing the classical regime $S \leq 2$ by approximately three standard deviations.

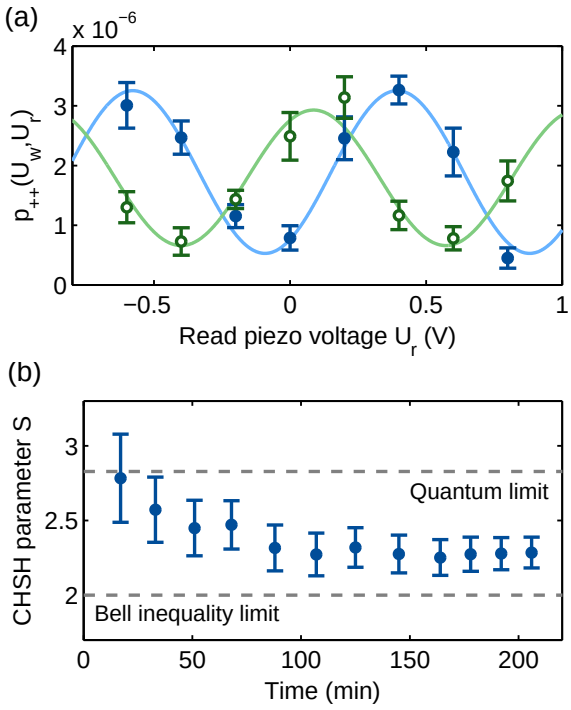

FIGURE 5.5: Bell test data using human random numbers. (a) Photon coincidence detection probability between detectors D_w^+ and D_r^+ as a function of the voltage applied to the piezo of the read photon interferometer. The two different curves correspond to two different voltages applied to the piezo of the write photon interferometer: $U_w = 0\,V$ (blue dots) and $U_w = 0.296\,V$ (green circles). (b) Accumulated CHSH Bell parameter S as a function of data acquisition time for the measurement with stored human random numbers.

5.4 Discussions and conclusions

As can be observed in Fig. 5.3a, the overlap of the early and late photonic modes in the interferometer is limited to a probability of 50%. The events in the first and third peaks in the write and read photon histograms are discarded for our Bell inequality analysis. This limitation is due to the beam splitter at the input of the interferometers, and leads to a Bell inequality loophole that is present in many of the photonic energy-time and time-bin entanglement experiments. In order to avoid it one could either

replace the input beam splitter by an optical switch [180], or change the geometry of the experiment as described in [181, 182].

In conclusion, we presented the direct generation of time-bin entanglement between a photon and a collective atomic spin excitation. After transferring the atomic qubit into a photonic state, the qubits were analyzed with Mach-Zehnder interferometers and we verified the entanglement by violating a CHSH Bell inequality. We also obtained similar results using human random numbers to decide the measurement settings, contributing to test the freedom-of-choice loophole in Bell tests.

Photons with a narrow linewidth as generated with our system are crucial for an optimal interaction with other narrow-band matter quantum systems, like trapped ions, doped crystals, etc. Since photonic time-bin qubits are very suitable for quantum frequency conversion [97, 113], entanglement between hybrid matter systems could be achieved through the frequency conversion and distribution of the write photonic qubit [101, 122, 183].

Chapter 6

Connection with other quantum light-matter interfaces

In chapter 3 and chapter 4 we address two issues that are required in order to transfer photonic quantum states generated by our system to other types of light matter interfaces. In chapter 3 the frequency matching issue is adressed through frequency conversion using a non-linear crystal. In chapter 4 the bandwidth match issue is adressed by studying the photon temporal waveform duration tunability. After successfully accomplishing these projects we were ready to transfer photonic quantum states to other light-matter interfaces based on different types of platforms. We performed two such experiments, with photonic connections to an atomic ensemble with Rydberg atoms and to an ion-doped crystal. The Rydberg platform consists of an ensemble of ^{87}Rb atoms and hence there was no need for frequency conversion. However, the crystal was doped with praseodymium

ions with a strong optical transition at $\lambda = 606\,\text{nm}$, which required the frequency conversion of the photons emitted by our laser-cooled atomic system. For both experiments, the tunability of the temporal waveform of the emitted photons as studied in chapter 4 was crucial.

6.1 Storing synchronizable single photons in a highly excited Rydberg state

Rydberg atoms are atoms in which the electron is excited to a level with a very high principal quantum number. In this situation the electron is very far from the nucleus leading to an extremely large atomic dipole moment between Rydberg states. This means that atoms relatively far apart (few μm scale) exhibit a strong interaction. In the context of quantum nonlinear optics, Rydberg atoms can be used to mediate efficient photon-photon interactions. Typically single photons show a negligible interaction between each other when different modes are overlapped. Therefore mediating the interaction with Rydberg atoms is a very interesting way to study quantum non-linear optics phenomena. Apart from the fundamental interest, the interaction between single photons could also enable some interesting quantum information tools, such as deterministic photonic Bell state measurements through a CNOT gate. Our DLCZ source can be operated as a herladed single photons source of synchronizable single photons, and therefore combining the two systems could lead to the deterministic interaction between two single photons. In this direction we performed a proof of principle experiment in which we studied the storage of single photons emitted by the DLCZ source, as a Rydberg excitations in another atomic system.

The results presented in this section have been published in [184], and the text is mostly adapted from the publication. This experiment was done in collaboration with PhD students Emanuele Distante and Auxiliadora Padrón, who were in charge of the Rydberg experiment setup.

6.1.1 Introduction

Efficient photon-photon interactions require a highly nonlinear medium which strongly couples with a light field, a single-photon source compatible with the medium and the ability to coherently map the photon in and out of the nonlinear medium [6]. In addition, for quantum repeaters applications for long distance quantum communication, the single photon should be part of a correlated photon pair generated by a quantum memory (QM) which allows for synchronization along the communication line [9]. Nonlinearity at the single-photon level has been demonstrated with a variety of systems, including single atoms and atomic ensembles [27, 38, 43, 185–192] as well as nonlinear crystals albeit with small efficiency [193]. However, the coupling of true single photons with a highly nonlinear medium has been demonstrated so far only with single atoms [27, 192]. These systems are inherently nonlinear but suffer from low light-matter coupling in free-space and therefore require experimentally challenging high-finesse cavities.

Using highly excited Rydberg states of atomic ensembles can be a simpler alternative. The atomic ensemble ensures a strong light-matter coupling and the dipole-dipole (DD) interactions between Rydberg states enable strong, tunable nonlinearities. For a sufficiently dense ensemble ($\rho \sim 10^{12}\,\mathrm{cm}^{-3}$) and at sufficiently high quantum number of the Rydberg state ($n \geq 60$), nonlinear response at the single-photon level has been already demonstrated [194–198] and has been exploited to implement a

number of operations with weak coherent states (WCSs) [44, 199–201]. Entanglement between a light field and a highly excited Rydberg state [202] has also been recently demonstrated.

While single-photon nonlinearities have been demonstrated with weak coherent states, efficient quantum information processing using this system require two additional steps. First, a single-photon source that matches the frequency and the sub-MHz spectral bandwidth of the Rydberg excitation, and, second, the ability to store and retrieve the input single photon. The latter is of key importance for implementing high-fidelity photonic quantum operations using excited Rydberg states [201, 203, 204], and, in addition, it has been shown to be beneficial to enhance the nonlinear response of this kind of systems [205]. While storage and retrieval of a single photon transmitted between remote atomic ensembles has been achieved in ground states [26, 206–209] or low-lying Rydberg states [210], storing it in a highly nonlinear Rydberg ensemble presents additional experimental challenges. Some of them include the high sensitivity to stray fields, stronger motional-induced dephasing due to the large wavelength mismatch between the single photon and the coupling laser, weak transition oscillator strength requiring higher intensity of the coupling beam, as well as strong focusing of the single-photon needed to achieve non-linearity at low light power. These challenges make it more difficult to achieve the required signal-to-noise ratio to preserve the quantum character of the stored and retrieved field.

6.1.2 Experiment description and results

In this work we demonstrated the storage and retrieval of a paired and synchronizable single photon in a highly nonlinear medium based on excited Rydberg atomic states of a cold atomic ensemble. We used the photon source characterized in chapter 4 in order to generate pairs of non-classically correlated photons that fulfil the frequency and the narrow bandwidth requirement of the Rydberg medium. In the generation stage (site A in Figure 6.1), after a successful heralding event a single photon is emitted at a programmable delay time t_{A} allowing for potential synchronization between different pair sources. The photon is then collected into an optical fibre and sent to a remote atomic ensemble (site B in Figure 6.1) where it is stored as a collective Rydberg excitation and retrieved after a storage time t_{B}. This is realized by creating in a heralded fashion a single collective spin excitation in the cold atomic ensemble quantum memory, by transfering it determinstically onto a compatible single photon and by mapping this photon into a single collective Rydberg excitation in another cold atomic ensemble. The storage and retrieval in high lying Rydberg states is realized with sufficiently high signal-to-noise ratio (SNR>20) to enable the demonstration of highly non-classical correlations between the heralding photon and the highly excited Rydberg collective excitation, and preservation of the single photon character of the retrieved field. Finally, we also demonstrate the highly nonlinear response of our medium with weak coherent states containing tens of photons. The last result is obtained in a cloud with moderate density ($\rho \sim 10^{10}\,\mathrm{cm}^{-3}$) and can be easily improved to reach single-photon nonlinearity via upgraded well-known techniques of atom trapping.

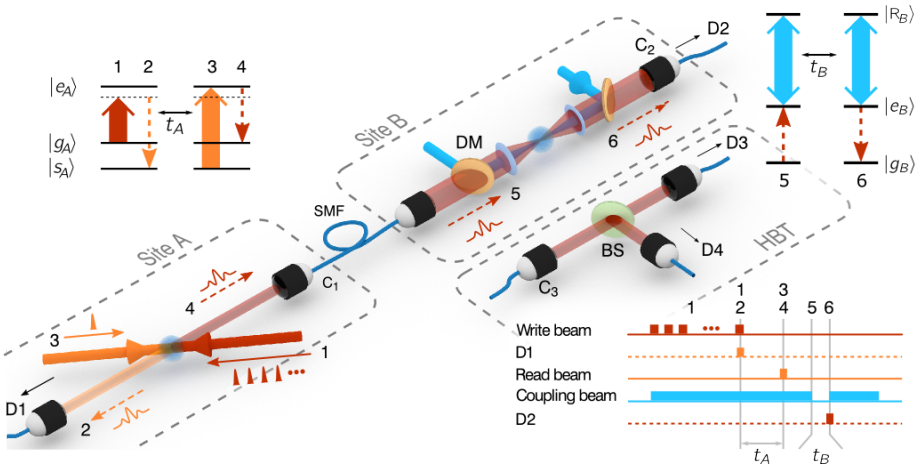

FIGURE 6.1: Experimental setup, relevant atomic transitions and pulse sequence. Following the numbering in the pulse sequence, in site A we (1) send a series of write pulses (red solid arrow), (2) probabilistically detect a write photon (orange dashed line) by single-photon detector (SPD) D1, (3) send a an intense read pulse (orange solid arrow) after a storage time t_A generating deterministically (4) a read photon (red dashed line) which is sent to Site B through a single mode fiber (SMF). In site B, a counter propagating, coupling beam (blue arrow) converts the read photon into a slowly propagating dark-state polariton. Here we (5) switch off the coupling beam, storing the read photon, and (6) switch it on again after a storage time t_B retrieving the photon which is detected by SPD D2. The coupling beam and the read photon are both focused by the same pair of aspheric lenses and are combined and separated by dichroic mirrors (DM). Hanbury Brown-Twiss (HBT) setup is shown in another box. The field to be analyzed emerges from the SMF at position C_3, it is split by a 50:50 beam splitter (BS) and detected by two detectors, D3 and D4 afterwards. To analyze the photon statistics before and after storage in the Rydberg state, we connect the HBT setup either at position C_1 or at C_2.

6.1.2.1 Experimental set-up

A schematic of the experiment is shown in Figure 6.1. In site A, we implement a photon-pair source with controllable delay, using the DLCZ scheme in a laser-cooled atomic ensemble as described in subsection 1.2.4. Atoms initially prepared in the ground state $|g_A\rangle = |5S_{1/2}, F = 2, m_F = 2\rangle$ are illuminated with a series of write pulses at 780 nm red detuned by

$\Delta = 40\,\mathrm{MHz}$ with respect to the $|g_\mathrm{A}\rangle \rightarrow |e_\mathrm{A}\rangle = |5P_{3/2}, F = 2, m_F = 1\rangle$ transition so that a write photon is probabilistically created via Raman scattering and detected on the single-photon detector (SPD) D1. This heralds a single collective excitation in the state $|s_\mathrm{A}\rangle = |5S_{1/2}, F = 1, m_\mathrm{F} = 0\rangle$ (see subsection 1.2.4). The excitation can be deterministically read-out after a controllable storage time t_A by means of a strong, counterpropagating read pulse on resonance with the $|s_\mathrm{A}\rangle \rightarrow |e_\mathrm{A}\rangle$ transition. The read pulse creates a 350 ns long (FWHM) read photon in a well defined spatio-temporal mode resonant with the $|g_\mathrm{A}\rangle \rightarrow |e_\mathrm{A}\rangle$ transition. The read photon is collected and sent through a 10 m single-mode fiber (SMF) to site B, where a separate ensemble of cold ^{87}Rb atoms is prepared in the state $|g_\mathrm{B}\rangle = |5S_{1/2}, F = 2\rangle$. We estimate that the probability to obtain a single photon in front of ensemble B conditioned on the detection of a write photon (the heralding efficiency) is $\eta_H = 0.27$. At site B, a coupling beam at 480 nm resonant with the $|e_\mathrm{B}\rangle \rightarrow |R_\mathrm{B}\rangle$, transition creates the condition for electromagnetically induced transparency (EIT) [211–213], where $|e_\mathrm{B}\rangle = |5P_{3/2}, F = 2\rangle$ and $|R_\mathrm{B}\rangle = |60S_{1/2}\rangle$. This converts the read photon into a slow-propagating Rydberg *dark-state polariton* (DSP). By adiabatically switching off the coupling beam, the read photon is stored as single collective Rydberg atomic excitation [214] and the state of the ensemble reads:

$$|\psi_\mathrm{B}\rangle = \frac{1}{\sqrt{N_\mathrm{B}}} \sum_{j=1}^{N_\mathrm{B}} e^{-i(\mathbf{k}_\mathrm{p}+\mathbf{k}_\mathrm{c})\cdot\mathbf{r}_j} \, |g_{\mathrm{B}_1} ... R_{\mathrm{B}_j} ... g_{\mathrm{B}_{N_\mathrm{B}}}\rangle \,, \tag{6.1}$$

where N_B is the number of atoms in the interaction region and $\mathbf{k}_\mathrm{p}$ and $\mathbf{k}_\mathrm{c}$ the wavevector of the single photon and of the coupling beam respectively. The stored excitation is retrieved after a storage time t_B by switching the coupling beam back on and detected by a SPD D2. As mentioned

in chapter 4 the read photon waveform in ensemble A can be tailored by shaping the read pulse. This is used in order to maximize the signal-to-noise ratio of the storage in site B. In order to match the frequency of the single photon emitted at site A, we have to employ at site B the $|5P_{3/2}, F = 2\rangle \rightarrow |nS_{1/2}\rangle$ transition instead of the most commonly used and stronger $|5P_{3/2}, F = 3\rangle \rightarrow |nS_{1/2}\rangle$ transition [44, 194, 197, 198, 201]. This makes it more challenging to reach high storage efficiency of the single photon into the collective Rydberg state.

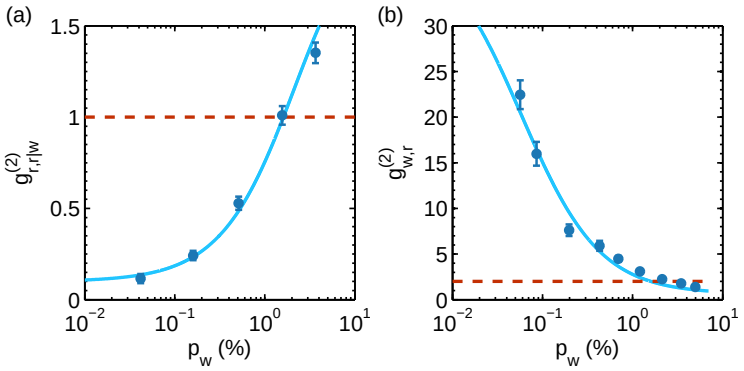

FIGURE 6.2: (a) Anti-bunching parameter $g^{(2)}_{\mathrm{r,r|w}}$ measured before site B and (b) cross-correlation function $g^{(2)}_{\mathrm{w,r}}$ measured after site B without loading the atomic ensemble. Data are taken at $t_{\mathrm{A}} \sim 1\mu$s. For low p_{w} high quality heralded single photons in the read mode as well as non-classical correlations are created, beating the classical bounds (indicated by the dashed line). The solid lines are fits with the model described in Appendix B.2 and Appendix D.3. The error bars are the propagated Poissonian error of the photon counting probabilities.

6.1.2.2 The DLCZ source characterization

First, at fixed $t_{\mathrm{A}} \sim 1\,\mu$s we characterize the DLCZ memory in site A as a source of high-quality synchronizable single photons when no storage in site B is performed, as shown in Fig. 6.2. The read single photon quality is inferred by measuring its heralded anti-bunching parameter

$g^{(2)}_{\mathrm{r,r|w}} = p_{\mathrm{r_3,r_4|w}}/p_{\mathrm{r_3|w}}p_{\mathrm{r_4|w}}$ via Hanbury Brown-Twiss (HBT) measurement before the 10 m SMF. We also measure the second-order, cross-correlation function $g^{(2)}_{\mathrm{w,r}} = p^0_{\mathrm{w,r_2}}/p_{\mathrm{w}}p^0_{\mathrm{r_2}}$ of the paired write and read photons without loading the atoms in site B. Here p_{w} (p_{r_i}) is the probability to detect a write (read) photon by SPD D1 (Di, with $i = 1, 2, 3$), while $p_{x,y}$ is the probability of coincident detection event x and y and $p_{x|y}$ is the conditional probability of event x conditioned on y. The superscript 0 indicates that no atoms are loaded in site B. At low p_{w}, a successful detection of a write photon projects the read mode into a single-photon state, with measured values as low as $g^{(2)}_{\mathrm{r,r|w}} = 0.11 \pm 0.02$ at $p_{\mathrm{w}} = 0.04\,\%$, shown in Figure 6.2a. In the same condition strong non-classical correlations are found, $g^{(2)}_{\mathrm{w,r}}$ being well above the classical bound of 2 for a state emitted by a DLCZ QM (assuming thermal statistics for the write and read fields, see Appendix A). At higher p_{w}, multiple excitations are created in the atomic ensemble and the classical bounds for $g^{(2)}_{\mathrm{r,r|w}}$ and for $g^{(2)}_{\mathrm{w,r}}$ are recovered (see Appendix A and Appendix B).

6.1.2.3 Storage in the Rydberg ensemble

We then store the emitted single photon as a collective high-lying Rydberg atomic excitation (see Fig. 6.3a). Keeping a fixed $t_{\mathrm{A}} \sim 1\,\mu$s, we load the atoms in site B and we store the read photon as atomic coherence between states $|g_{\mathrm{B}}\rangle$ and $|R_{\mathrm{B}}\rangle$ by switching off the coupling beam while the photon is propagating through the ensemble. After a storage time t_{B}, we retrieve the stored excitation by switching the coupling beam back on. At $t_{\mathrm{B}} = 500$ ns, we achieve a storage and retrieval efficiency of $\eta_{\mathrm{B}} = 3.4 \pm 0.4\%$ where η_{B} is defined as $\eta_{\mathrm{B}} = p_{\mathrm{r_2|w}}/p^0_{\mathrm{r_2|w}}$. We also measure $g^{(2)}_{\mathrm{w,r}} = p_{\mathrm{w,r_2}}/p_{\mathrm{w}}p_{\mathrm{r_2}}$ after storage and retrieval (see Fig. 6.3b). Our data show that $g^{(2)}_{\mathrm{w,r}} \gg 2$ for low

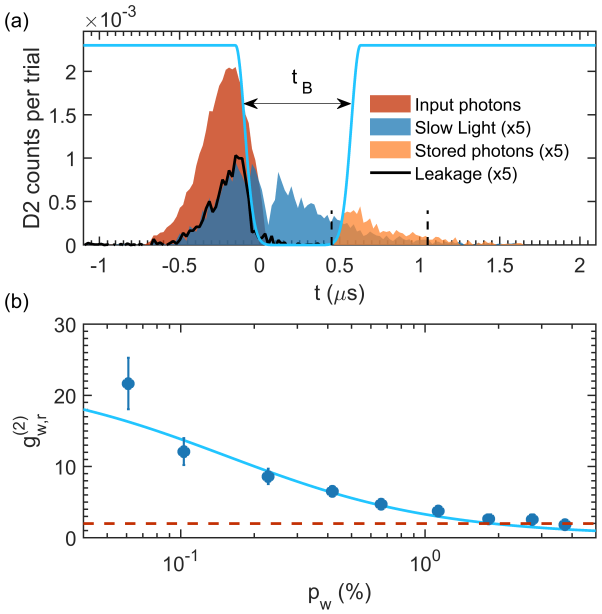

FIGURE 6.3: Single-photon storage sample and cross-correlation (a) Example of single-photon storage for $t_A \sim 1\,\mu$s and $p_w = 2.7\,\%$. Detected counts of single-photon detector D2 per trial and per temporal bin, conditioned on a detection of a write photon, as a function of the detection time t when no atoms are loaded in site B (red trace), when the read photon is slowed by the presence of the coupling beam (i.e. when the coupling beam is kept on, blue trace) and when the read photon is stored and retrieved for $t_B = 500$ ns (orange trace). We attribute the dip at $t \sim 0\,\mu$s observable in the slow light pulse (blue trace) to the fast switch-off of the trailing edge of the input read photon (see [215, 216]). The solid black line represents a leakage of the slowed read photon due to low optical depth of the ensemble in site B. The solid light blue line is a pictorial representation of the coupling beam power. The vertical dashed lines shows the 600 ns temporal window chosen for measuring p_{w,r_2}. In this example the storage efficiency is $\eta_B = 3.4\,\%$. (b) $g^{(2)}_{w,r}$ as a function of p_w after storage and retrieval of the read photon for $t_B = 500$ ns. The solid line is a fit with a model given in section D.3 from which we extract the intrinsic read-out efficiency of the DLCZ source $p^{int}_{r|w} = 38.5\,\%$. The dashed horizontal line represents the classical bound $g^{(2)}_{w,r} \leq 2$.

p_w demonstrating the persistence of non-classical correlations between the write photon and the collective Rydberg atomic excitation after storage. At $t_B = 500$ ns, we explicitly violate the Cauchy-Schwarz (CS) inequality by three to four standard deviations (see Tab. 6.1), which states that a pair

of independent light fields must satisfy $R = \left[g^{(2)}_{\mathrm{w,r}}\right]^2 / \left[g^{(2)}_{\mathrm{w,w}}\, g^{(2)}_{\mathrm{r,r}}\right] \leq 1$, where $g^{(2)}_{\mathrm{w,w}}$ and $g^{(2)}_{\mathrm{r,r}}$ are the unheralded second order autocorrelation functions of the write and read photon (see Appendix A). For the same storage time we also measured the anti-bunching parameter $g^{(2)}_{\mathrm{r,r|w}}(\mathrm{B})$ of the stored and retrieved read photon by a HBT measurement after site B and we found $g^{(2)}_{\mathrm{r,r|w}}(\mathrm{B}) = 1.2 \pm 0.2$ at $p_{\mathrm{w}} = 3.98\,\%$ and $g^{(2)}_{\mathrm{r,r|w}}(\mathrm{B}) = 0.0 \pm 0.35$ at $p_{\mathrm{w}} = 0.59\,\%$, the latter confirming that the single-photon statistics are preserved after storage and retrieval.

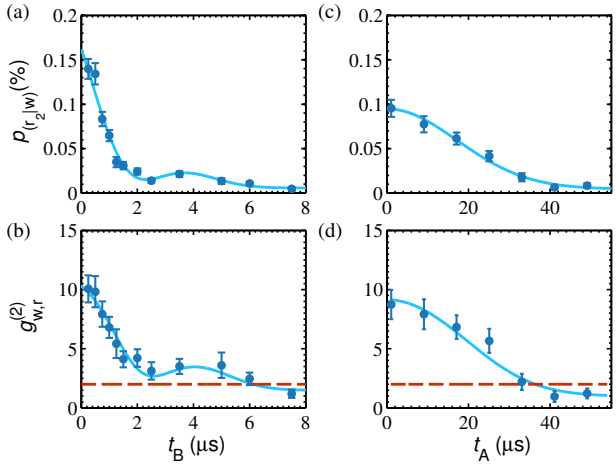

FIGURE 6.4: Coincidence detection probability $p_{\mathrm{r_2|w}}$ and $g^{(2)}_{\mathrm{w,r}}$ as function of t_{B} for $t_{\mathrm{A}} \sim 1\,\mu$s (panel (a) and (b)) and as a function of t_{A} for $t_{\mathrm{B}} = 500$ ns (panel (c) and (d)). In (a) the measured $p_{r_2|w}$ at $t_{\mathrm{B}} = 500$ ns corresponds to a storage and retrieval efficiency $\eta_{\mathrm{B}} = 3.8 \pm 0.4\%$. The solid lines are fits to the experimental data, as described in the text.

$p_{\mathrm{w}}(\%)$	$g^{(2)}_{\mathrm{w,r}}$	$g^{(2)}_{\mathrm{w,w}}$	$g^{(2)}_{\mathrm{r,r}}$	R
3.7	1.8 ± 0.2	1.90 ± 0.02	1.5 ± 0.3	1.2 ± 0.3
1.13	3.7 ± 0.3	1.97 ± 0.03	1.6 ± 0.3	4.4 ± 1.0
0.66	4.7 ± 0.5	2.00 ± 0.06	1.5 ± 0.5	7.7 ± 2.6

TABLE 6.1: Reported value of the R parameter for the Cauchy-Schwarz inequality. Data are taken for $t_{\mathrm{A}} = 1\,\mu$s and $t_{\mathrm{B}} = 500$ ns. For low p_{w}, the CS inequality is explicitly violated.

The memory capabilities of the Rydberg ensemble and of the DLCZ QM are studied in Fig. 6.4 for $p_{\mathrm{w}} = 0.16 \pm 0.02\,\%$. First we show $p_{\mathrm{r_2|w}}$ and $g^{(2)}_{\mathrm{w,r}}$ as a function of t_{B} (see Fig. 6.4(a,b)) keeping a fixed $t_{\mathrm{A}} \sim 1\mu$s. $p_{\mathrm{r_2|w}}$, along with $g^{(2)}_{\mathrm{w,r}}$, decreases when increasing the storage time, due to atomic motion and external residual fields which dephase the collective Rydberg state of Eq. (6.1). We also observe a oscillatory revival which we attribute to the hyperfine splitting ΔF of the Rydberg state $|R_{\mathrm{B}}\rangle$ resulting in a beating of $p_{\mathrm{r_2|w}}$ with a period $T = 1/\Delta F$. The non-classical correlations between a photon and a stored Rydberg excitation are preserved up to around $t_{\mathrm{B}} \sim 6\mu s$. Fitting $p_{\mathrm{r_2|w}}$ and $g^{(2)}_{\mathrm{w,r}}$ with a model shown in Appendix D, we extract the $1/e$ decay time of the storage efficiency, $\tau_{\mathrm{R}} = 3.3 \pm 0.3\,\mu$s as well as $\Delta F = 170 \pm 16$ kHz, the latter being compatible with the theoretical value of $\Delta F_{\mathrm{theo}} = 182.3$ kHz.

We also verify that we can generate the write and the read photon with long, controllable delay in site A, maintaining the non-classical correlation between them after storage and retrieval in site B. This result is shown in Fig. 6.4(c,d) where we change the read-out time t_{B} of the stored ground-state spin-wave while keeping a fixed $t_{\mathrm{B}} = 500$ ns. Here, the ground state storage ensures a storage time longer than in the Rydberg state. In this case the $1/e$ decay time is $\tau_{\mathrm{DLCZ}} = 24 \pm 2\,\mu$s and we observe non-classical correlations between the write and the stored and retrieved read photon in site B up to $t_{\mathrm{A}} \sim 30\,\mu$s.

6.1.2.4 Nonlinear response of the Rydberg ensemble

Finally we prove the highly nonlinear response of the Rydberg ensemble. This is demonstrated by storing for $4\,\mu$s weak coherent states with varying mean number of input photon N_{in} and measuring the mean number

of photons in the retrieved pulse after storage N_{out}, in a way presented in [205]. For a linear medium $N_{\text{out}} = TN_{\text{in}}$ where T is the storage efficiency, while here we show (Fig. 6.5) strong nonlinear dependence. DD interactions prevent many excitations to be stored and retrieved in the medium, which can therefore sustain no more than N_{max} photons. As a consequence N_{out} becomes $N_{\text{out}} = N_{\text{max}}T(1 - e^{-N_{\text{in}}/N_{\text{max}}})$ [200]. Our result shows $N_{\text{max}} = 68 \pm 8$ although the nonlinear dependence of N_{out} with respect to N_{in} appears at a lower number of photons. It should be noted that this result is obtained with a standard magneto-optical trap with a moderate atomic density. As demonstrated in [194, 197, 198], increasing the density of atomic ensemble with known atomic trapping techniques will allow us to achieve nonlinearity at the single-photon level, as required for applications in quantum information science.

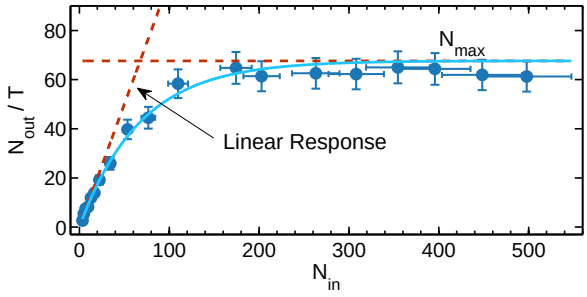

FIGURE 6.5: Nonlinear response of the Rydberg blockaded ensemble in site B. We store weak coherent states with a varying mean number of photon N_{in} into the Rydberg state $|R_{\text{B}}\rangle$ for a storage time $t_A = 4\,\mu$s and we measure the mean number of output photons N_{out}. We plot N_{out} normalized by the storage efficiency at low number of photons T as a function of N_{in}. Due to Rydberg induced photon blockade, the medium can stand a maximum of $N_{\text{max}} = 68 \pm 8$. In this example $T = 0.44 \pm 0.02\,\%$.

6.1.3 Discussions

In this work we demonstrated for the first time storage and retrieval of a paired single photon on a highly nonlinear medium based on an atomic ensemble. The nonlinearity relies on highly excited Rydberg states where the capability of successfully storing a single photon is of particular importance for implementing high fidelity quantum gates. Connecting our photon source with a highly nonlinear medium represents a building block for quantum networks where the entanglement can be deterministically shared over long distance by deterministic Bell state measurements.

6.2 Photonic quantum state transfer between a cold gas and a crystal

As mentioned in subsection 1.3.1 there have been several experiments involving the photonic quantum state transfer between long lived matter systems. However, in all these experiments the same atomic species was used for both systems. The main motivation of this experiment was to demonstrate the photonic quantum state transfer between two very different systems (in our case a gas of rubidium atoms and a crystal doped with praseodymium ions). Apart from the fundamental interest of the experiment, it also opens the way to the hybrid quantum photonic interconnection that combines advantages of different matter systems. For this specific connection the advantages of both systems would be the following. Laser-cooled gasses of alkali atoms can be operated as excellent single photon or entangled photon-pair sources, and can provide quantum processing through Rydberg excitations. Rare-earth-doped crystals have shown to provide excellent properties for long-term quantum state storage

and multiplexing. The method that we employed could in principle also be used to connect other different types of quantum light-matter interfaces.

The results presented in this section have been published in [183], and the text is mostly adapted from the publication. This experiment was done in collaboration with PhD students Nicolas Maring and Kutlu Kutluer, who were in charge of the quantum frequency conversion device and the doped crystal setup, respectively.

6.2.1 Introduction

A hybrid quantum network, which benefits from the strengths of different platforms, could offer more capabilities than a network consisting of identical quantum systems. Although significant efforts have been devoted to build hybrid quantum systems e.g. devices combining different quantum systems on a single chip [217], or different species of closely spaced trapped ions [218, 219], interactions between these systems are typically mediated by microwave photons or Coulomb interactions, which are not favorable for long distance quantum communication.

Instead, photonic interconnections between different quantum systems have so far been realized only in very few experiments [220–223], however neither demonstrating quantum state transfer nor interfacing two different long-lived quantum memory (QM) systems, which are both crucial requirements for quantum networks applications. A photonic quantum interconnection between different platforms was demonstrated in Ref. [26], using a single atomic species. The main challenge to efficiently interface two different quantum systems via a photonic link, is to obtain strong light-matter interaction between a single mediating photon and both matter systems, whose atomic transitions can differ significantly in wavelength and linewidth.

In this work, we demonstrated quantum state transfer between two fundamentally different quantum memory systems via a single photon at telecom wavelength. On the one hand, we use a laser cooled ensemble of ^{87}Rb atoms, which, besides being an excellent quantum memory and single photon source [9], also gives access to tunable non-linear interactions enabling quantum processing via Rydberg excitations [224]. On the other hand, we use a rare earth ion doped crystal (Pr^{3+}: Y_2SiO_5) exhibiting outstanding properties for multiplexed long-lived quantum state storage [85, 225–227]. To overcome the wavelength gap between both systems, we use quantum frequency conversion techniques to convert photons emitted by the ^{87}Rb QM from 780 nm to the telecom C-band at 1552 nm and then back to 606 nm to resonantly interact with the Pr^{3+}: Y_2SiO_5 crystal. We show that a single collective spin excitation (spin-wave) stored in the cold atomic QM can be optically transferred onto a long-lived collective optical excitation inside the crystal. By transmitting correlated single photons and qubits, we demonstrated quantum correlation preserving and coherent quantum state transfer between the disparate quantum nodes.

6.2.2 Experiment description and results

6.2.2.1 Experimental setup

The basic concept of our experiment can be understood along the schematic depicted in Fig. 6.6 which is separated into two main sites A and B (more details can be found in the Methods section in [183]. At site A, we operate the ^{87}Rb MOT to generate synchronizable single photons of controllable bandwidth and temporal shape as described in chapter 4. These photons are later frequency converted from 780 nm to 1552 nm in a quantum

frequency conversion device (QFCD) similar as the one described in chapter 3. Following the DLCZ scheme (subsection 1.2.4) we send a series of classical write pulses onto the Rb atoms to create Raman-scattered write photons with intrinsic excitation probability p_e per optical mode and trial. A single optical mode of the isotropically emitted write photons is collected and sent to single photon detector (SPD) D1. A detection event at D1 heralds the generation of a spin-wave involving long-lived ground states of the ^{87}Rb ensemble. After a programmable storage time, we apply a read pulse, to deterministically read-out the spin-wave and generate a read photon in a well defined spatio-temporal mode, with a fiber-coupled read-out efficiency of $p^{A}_{r|w} \approx 30\%$. Depending on the temporal shape of the read pulse, we generate single read photons with Gaussian envelope or double time-bin envelope exhibiting a sub-natural linewidth of about 2 MHz (cf. chapter 4). The read single photon is then sent to the first QFCD, which converts it from 780 nm to 1552 nm via difference frequency generation (DFG) with an internal conversion efficiency of $\eta_{int}^{QFCD1} = 56\%$ (cf. chapter 3). After noise filtering, the converted photon is then coupled into a 10 m telecom fiber and sent to site B in another laboratory.

At site B, the telecom read photon is first back-converted to 606 nm ($\eta_{int}^{QFCD2} = 60\%$) via sum frequency generation (SFG) in QFCD2. After noise filtering the single photon is sent to the Pr^{3+}: Y_2SiO_5 crystal inside a cryostat at a temperature of 3.5 K. We use the atomic frequency comb (AFC) scheme [89] to store, analyze, and retrieve the converted single photon. We create an AFC of 4 MHz width with absorption peaks spaced by $\Delta = 400$ kHz on the optical transition of Pr^{3+} at 606 nm. Then, the converted single photon is stored by the AFC and collectively re-emitted with an efficiency of $\eta^B = 30\%$ after a pre-defined storage time of $\tau_B = 1/\Delta = 2.5\,\mu$s before being detected by SPD D2. The probability to obtain an emitted,

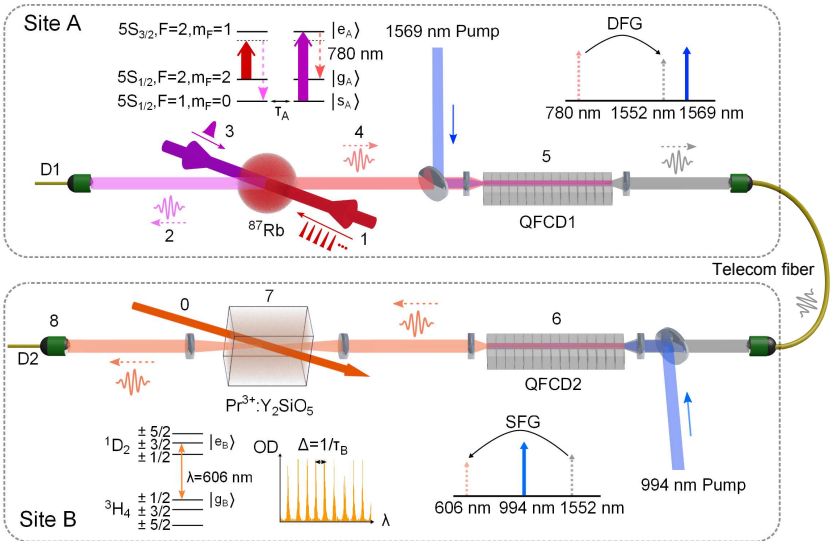

FIGURE 6.6: Schematic setup and relevant level schemes. At site A a cold cloud of ^{87}Rb atoms is held inside a MOT. Following the DLCZ scheme, non-classically correlated photon pairs are produced by first sending classical write pulses (1) generating a spin-wave inside the atomic cloud heralded by a write photon (2) which is spectrally filtered by a monolithic Fabry-Perot cavity (not shown). Upon a write photon detection at D1, the spin-wave is read-out by sending a classical read pulse (3) generating the read photon (4). QFCD1 consists of a periodically poled lithium niobate (PPLN) crystal with an integrated waveguide continuously pumped by a strong pump laser at 1569 nm. It converts the read photon from 780 nm to 1552 nm (5). The converted photon is then separated from the strong pump light via dielectric band pass filters (not shown) before it is sent via a telecom fiber to site B where QFCD2 (consisting of a PPLN ridge waveguide pumped by strong 994 nm laser radiation) converts it to 606 nm via SFG (6) before the photon is again spectrally filtered by several elements (not shown). The Pr^{3+}: Y_2SiO_5 crystal was initially prepared with an AFC (0) using a strong preparation beam at 606 nm, to store the converted read photon (7). After retrieval it is finally detected at D2 (8).

converted, stored and retrieved photon after the crystal, conditioned on a write photon detection at D1, is approximately 10^{-3}. This includes 1.2% total conversion efficiency (with all optical losses) from 780 nm to 606 nm.

An important experimental requirement is to precisely match the central frequencies of the converted read photon and the prepared AFC, and to minimize the linewidths of all the lasers involved to ensure efficient storage and stable interference conditions for the qubit analysis. We estimate that the frequency stability of the converted photon needs to be significantly better than 1 MHz. This is done by active frequency stabilization and a chopped beat-note lock between classical 780 nm light converted in the QFCDs and the 606 nm preparation laser as reference.

6.2.2.2 Photon transfer

Before interfacing both quantum systems, we characterize the read photons generated at site A. Tuning the waveshape of the read pulse as studied in chapter 4 we can set the waveform of the read photons for an optimal interaction with the crystal (see Fig. 6.7a). In addition we can also generate read photons delocalized in two temporal bins, representing a photonic time-bin qubit (see Fig. 6.7b). Fig. 6.7c shows the heralded autocorrelation function $g^{(2)}_{\mathrm{r_A,r_A|w}}$ for different p_e measured via a Hanbury Brown - Twiss setup inserted directly after the MOT. We obtain strongly anti-bunched read photons in the single photon regime ($g^{(2)}_{\mathrm{r,r|w}} < 0.5$) for low $p_\mathrm{e} \lesssim 11\%$, in the non-classical regime ($g^{(2)}_{\mathrm{r,r|w}} < 1$) for $p_\mathrm{e} \lesssim 25\%$, before surpassing the classical threshold for higher p_e due to multiple spin-wave excitations. This data was taken using single-peaked Gaussian read photons as shown in Fig. 6.7a. For the doubly-peaked read photons shown in Fig. 6.7b (taken at $p_e = 5\%$) we measured $g^{(2)}_{\mathrm{r_A,r_A|w}} = 0.26 \pm 0.02$.

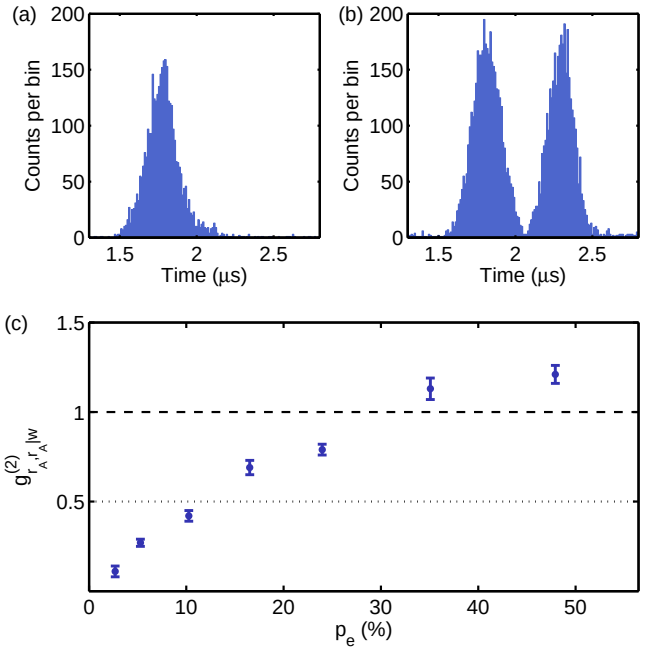

FIGURE 6.7: Photon generation. (a-b) Temporal histograms of the heralded read photons measured after the MOT at site A taken at $p_e = 5\%$. The photons in (a) are generated with a Gaussian-shaped read pulse, while the photons in (b) are generated with a doubly-peacked Gaussian read pulse. (c) Anti-bunching parameter of the read photon after the MOT vs p_e. The dashed line indicates the threshold for classical states ($g^{(2)}_{r,r|w} \geq 1$) and the dotted line the value for a two-photon Fock state ($g^{(2)}_{r,r|w} = 0.5$). Error bars correspond to ± 1 s.d. of the photon counting statistics.

We then present photon generation, conversion, and storage involving the whole experimental setup. We first verify that photons emitted by the atomic QM can be successfully converted and stored in the crystal. We create at site A a heralded 200 ns long (FWHM) Gaussian read photons at $p_e \approx 35\%$ (see Fig. 6.7a). Fig. 6.8b shows the histogram of detection events at D2. The photons arrive at the crystal at $t = 0\,\mu$s, however, no leakage is visible here, as they are buried in the noise generated by the QFCDs. The noise is suppressed at $t = 1.2\,\mu$s by gating off the pump of QFCD2. At $t = 2.5\,\mu$s we detect a pronounced echo signature from the retrieved

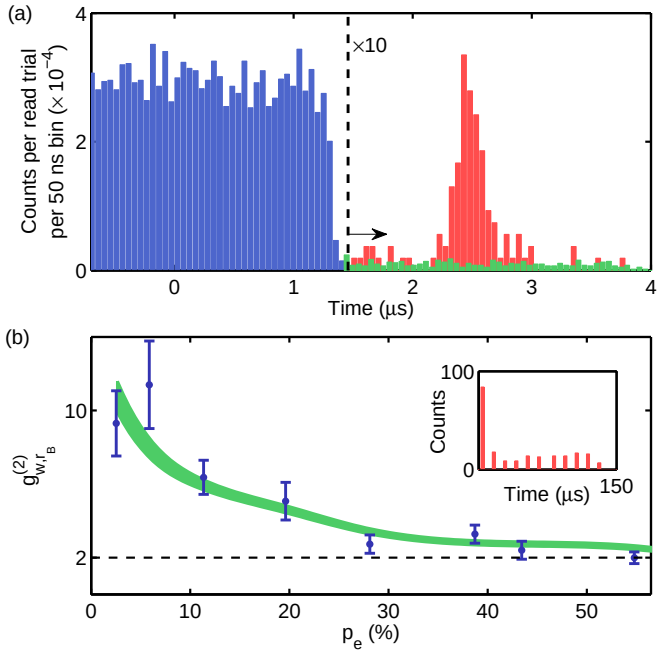

FIGURE 6.8: Photon conversion and storage. (a) Time histogram of detections at D2 if the spin-wave (excitation probability $p_e \approx 35\%$) is read-out from the cold atomic Rb QM, the photons are frequency converted in the QFCDs, and stored at $t = 0$ in the crystal. During storage (at $t = 1.2\,\mu$s), the pump of QFCD2 is gated off, and the re-emitted photons are detected as a pronounced AFC echo at $t = 2.5\,\mu$s (red trace, detected coincidence rate ~ 90 /h in a 400 ns window around the echo). The green trace corresponds to the noise level, i.e. if no read photon is sent. (b) Normalized cross-correlation $g^{(2)}_{\mathrm{w,r_B}}$ between the write photons from the cold atomic QM and the converted, stored and retrieved read photons from the crystal for different p_e. The green area corresponds to the expected $g^{(2)}_{\mathrm{w,r_B}}$ as deduced from a similar model as in [57]. The dashed line represents the classical upper bound $g^{(2)}_{\mathrm{w,r_B}} \leq 2$. The inset shows a typical $g^{(2)}$ histogram of coincidence detections for several read-out trials separated by the trial period of $\sim 13\,\mu$s obtained at $p_e \approx 11\%$.

read photons with a Signal to Noise Ratio SNR $= 17 \pm 2$, mostly limited by the dark counts of D2. The echo shows the same Gaussian temporal shape as the initial read photons with a FWHM of 200 ns.

6.2.2.3 Photonic quantum state transfer

To investigate the non-classicality of the state transfer, we measured the normalized cross-correlation function $g^{(2)}_{\mathrm{w,r_B}}$ of the converted, stored and retrieved photons with the initial write photons for different p_e by comparing coincidences in different storage trials (see Fig. 6.8b). At $p_\mathrm{e} \approx 5\%$ (with a coincidence rate of approximately 20 counts per hour) we obtain $g^{(2)}_{\mathrm{w,r_B}} = 11.4 \pm 2.4$, demonstrating quantum-correlation preserving state-transfer, as the $g^{(2)}_{\mathrm{w,r_B}}$ value stays well above the classical bound of $g^{(2)} = 2$ assuming thermal statistics for the write and read photons (cf. Appendix A). The experimental data in Fig. 6.8b match well with the expected behavior (green area) calculated via a simple model taking into account the measured cross-correlation $g^{(2)}_{\mathrm{w,r_A}}$ after the MOT and the total SNR of the read photon after conversion and storage [57].

Next, we studied the coherence properties of the state transfer between the two different quantum systems. If a heralding write photon is detected at D1, we shape the read pulse in a way that the spin-wave stored in the Rb QM is mapped onto a photonic time-bin qubit as shown in Fig. 6.7b. The state of this qubit can be represented as $|\Psi\rangle_A = c_1|e\rangle + c_2 e^{i\varphi}|l\rangle$, where $|e\rangle$ and $|l\rangle$ represent early and late time-bin, φ is their relative phase, controlled by the phase of the second read pulse, and $c_1^2 + c_2^2 = 1$. To store the photonic time-bin qubit, we take advantage of the intrinsic temporal multimodality of the AFC scheme [89].

Figure 6.9a shows the time histogram of detection events at D2 of the early and late time-bins (created at $p_\mathrm{e} \approx 35\%$) sent through the QFCDs, and stored and retrieved from the crystal prepared with a single AFC of $\tau_B = 2.5\,\mu$s storage time. The two echoes represent the polar states of a time-bin qubit and exhibit an average SNR above 19 ± 2. If a delocalized

time-bin photon ($c_1 = c_2 = \frac{1}{\sqrt{2}}$) is created in the Rb QM, converted in the QFCDs and stored in the crystal for either $\tau_{B_1} = 2\,\mu$s or $\tau_{B_2} = 2.5\,\mu$s, we detect the histograms shown in Fig. 6.9b. In order to analyze the qubit, we use the crystal as an interferometer by preparing two overlapped AFCs with storage times τ_{B_1} and τ_{B_2} ($\eta^{\mathrm{B}} = 10\%$ each) [89]. In that case, we obtain the histograms shown in the right panels of Fig. 6.9c. These two histograms were recorded with a phase shift of $\varphi = 0°$ (top) and $\varphi = 180°$ (bottom) between the early and late time-bin. Strong interference between the two temporal modes can be seen in the central region where the time-bins overlap. Measuring the coincidences in that time window vs. φ gives the interference fringe depicted in Fig. 6.9c with a fitted visibility of $V = 60 \pm 9.9\%$, confirming the high degree of coherence preservation between the two disparate quantum systems.

Finally, to demonstrate qubit transfer between the cold atomic cloud and the crystal via telecom photons, we decreased p_{e} to 5% generating true single time-bin read photons at site A with an anti-bunching parameter of $g^{(2)}_{\mathrm{r_A,r_A|w}} = 0.26 \pm 0.02$ (cf. Fig. 6.7c). Following the same approach as above, we show in Fig. 6.10a that with converted and stored single time-bin photons, we obtain interference between overlapping bins with visibilities around 70%. Moreover, we show that, by changing the central frequency of the second AFC by 200 kHz, the phase of the interference fringe can be shifted by 180° verifying the intrinsic phase analysing capabilities of the AFC. This capability permits the measurement of time-bin qubits in different bases and hence a full analysis of the stored qubits by quantum state tomography. Figure 6.10b shows the reconstructed density matrices ρ of the retrieved states after the crystal at site B when three orthogonal time-bin qubits ($|E\rangle$=$|e\rangle$, $|+\rangle = 1/\sqrt{2}(|e\rangle + |l\rangle)$, $|R\rangle = 1/\sqrt{2}(|e\rangle + i|l\rangle)$) are generated in the cold atomic QM at site A, afterwards converted in the

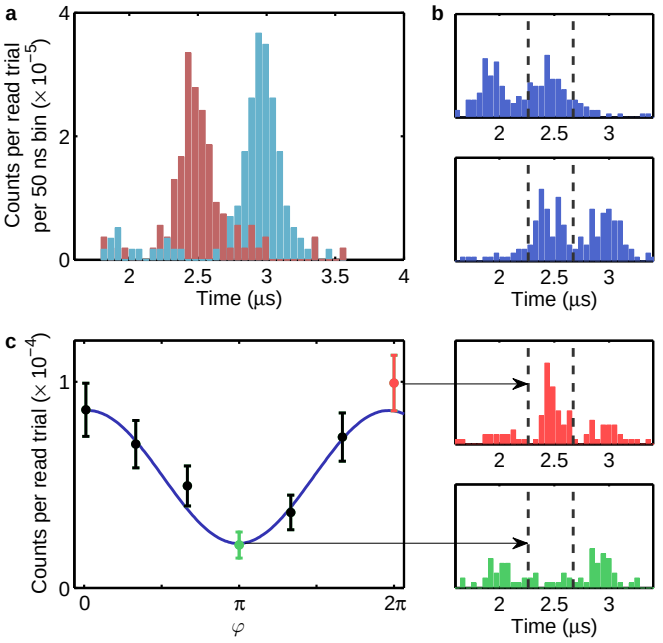

FIGURE 6.9: Coherence Preservation. (a) Detected echo of Gaussian shaped read photons which were created ($p_e \approx 35\%$) at either an early time $t = 0$ (red) or at a later time $t = 0.5\,\mu$s (blue) at site A and stored for $\tau_B = 2.5\,\mu$s at site B. (b) Time-bin photons stored and retrieved after either a short storage time $\tau_{B_1} = 2\,\mu$s (top) or a long one $\tau_{B_2} = 2.5\,\mu$s (bottom). (c) Time-bin interference fringe, i.e. coincidence counts between initial write photon detections at D1 and detection events during the time-bin-overlap at D2 if a time-bin read photon is stored and retrieved from the crystal prepared with two AFCs. Error bars correspond to ± 1 s.d. of the photon counting statistics. On the right two examples of time histograms between detection events at D1 and D2 are shown for $\varphi = 0°$ (top) and $\varphi = 180°$ (bottom). The 400 ns coincidence window where the time-bins overlap is indicated by dashed lines.

QFCDs, and stored at site B. The state reconstruction is based on maximum likelihood estimation. The qubit fidelity conditioned on a successful detection of the photon after the retrieval from the crystal (conditional fidelity) is calculated as $\mathcal{F}^c_{|\psi\rangle} = \langle\psi|\rho|\psi\rangle$ with $|\psi\rangle$ denoting the target state. From Fig. 6.10b it is evident that we obtain a high overlap between the reconstructed qubits and the target states with conditional fidelities of $\mathcal{F}^c_{|+\rangle} = 85.4 \pm 6.6\%$, $\mathcal{F}^c_{|R\rangle} = 78.2 \pm 6.9\%$, and $\mathcal{F}^c_{|E\rangle} = 93.8 \pm 2.8\%$, where

the errors were estimated via Monte Carlo simulations taking into account the uncertainty of the photon counting statistics. Despite the low total efficiency of the state transfer we demonstrate an average conditional fidelity of $\mathcal{F}^{c} = 85.8 \pm 3.3\%$ for the generated and transferred qubit which surpasses the classical threshold of 66.7% by more than 5 standard deviations [228]. Overall, the conditional fidelities are limited by the SNR of the retrieved photons, thus by the efficiencies of all the involved processes. However, for the equatorial states, the main limitation is the finite linewidth of the combined laser system, which we estimate to be around 600 kHz (see Appendix E). This large sensitivity to frequency fluctuations is due to the large separation between the two time-bins (500 ns) imposed by the AFC bandwidth.

6.2.3 Discussions

For potential applications in hybrid quantum networks, the transfer efficiency (currently 10^{-3}) should be greatly increased. The largest part of the inefficiency is due to technical optical loss in the various elements ($\eta_{\text{loss}} = 0.04$). This could be significantly improved, using e.g. fiber pigtailed waveguide converters. The combined quantum memory efficiency ($\eta_{\text{QM}} = 0.09$) could also be largely increased with state of the art techniques [68, 225]. Increased efficiencies would also enable spin-wave storage in the crystal, leading to on-demand read-out and longer storage times [227].

This work represents a demonstration of quantum communication between heterogeneous quantum nodes and opens prospects for combining quantum nodes with different capabilities. Moreover, it gives a perspective on

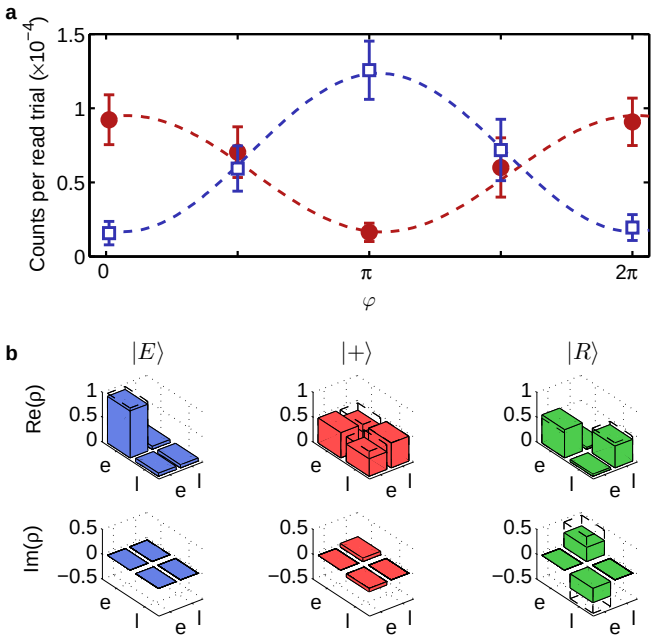

FIGURE 6.10: Single photon qubit transfer. (a) Interference fringes from a single read photon time-bin qubit $|\Psi_{\mathrm{eq}}\rangle = \frac{1}{\sqrt{2}}(|e\rangle + e^{i\varphi}|l\rangle)$ generated at site A ($p_{\mathrm{e}} \approx 5\%$ corresponding to $g^{(2)}_{\mathrm{r_A,r_A|w}} = 0.26$) if the second AFC is prepared with zero detuning (red dots, $V = 70 \pm 6\%$) or shifted by 200 kHz (blue open squares, $V = 76 \pm 3\%$). (b) Real and imaginary parts of the reconstructed density matrices measured after the crystal at site B if the qubits $|E\rangle$, $|+\rangle$, $|R\rangle$ are generated at site A, converted in the QFCDs and stored at B. Open boxes indicate the target state.

how the distance between the nodes can be extended by back- and forth-conversion of photonic qubits into the telecom C-band. Our technique could also be extended to connect other physical platforms, e.g. single ions or NV centers. These results hold promise for the realization of large scale hybrid quantum networks.

6.3 Conclusions

From the perspective of the DLCZ system, these two experiments are examples that take advantage of the photon frequency and temporal waveform tunability. Both Rydberg and doped crystal systems show an optimal storage of photons that have a specific temporal and spectral widths, which can be provided by the DLCZ photon source. Quantum frequency conversion allows one to bridge the wavelength gap between systems consisting of different elements, such as our rubidium laser-cooled gas and the praseodymium doped crystal. The experiments presented in this chapter were proof-of-principle examples of quantum state transfer between hybrid quantum light-matter interfaces. Other capabilities of the DLCZ system such as the possibility to generate photons entangled with the atoms (cf. chapter 5) or the capability to generate multiple-photon states could be a very interesting resource for future hybrid connections.

Chapter 7

Conclusions and future directions

The goal of the thesis was to develop and study a versatile source of atom-photon quantum states able to interconnect with other types of quantum light-matter interfaces. In particular we wanted to transfer the photonic part of the state to other matter systems. In the two first experiments that I have described in this thesis we studied two capabilities needed in order make these hybrid connections possible. In these two works we studied respectively the frequency and temporal waveform tunability of the single photons emitted by our system. The third work describes an experiment were we studied the generation of a light-matter entangled state that is suitable for long distance distribution. Finally, we took advantage of these studied capabilities in order to transfer quantum states from our laser-cooled system to two different types of light-matter interfaces (an atomic system with Rydberg excitations and an ion-doped crystal). The results

obtained in these experiments are summarized below and followed by a discussion on the future directions of the experiment.

7.1 Summary of the results

In chapter 3 we studied the frequency translation of single photons that are correlated with collective atomic spin excitations. The frequency conversion from 780nm to 1552nm takes place in a non-linear crystal that takes the form of a waveguide. The low noise operation of the frequency converting device, enabled a high spin-wave heralding efficiency and the preservation of non-classical correlations between the converted heralding photon and the atomic excitation. The collective excitation could be stored in the system for up to 40 μs.

In chapter 4 we studied the temporal waveform tunability of the heralded single photons generated by our quantum memory. Tuning the waveform of the read pulse allows us to generate single photons with Gaussian temporal envelopes and durations tunable three orders of magnitude up to around 10 μs. The numerical simulations performed by our theory collaborators showed that this upper limit is given by the coherence time of the collective spin excitation. We also showed the generation of single photons with exotic waveshapes like rising exponential or doubly-peaked, which have interesting applications in the field of quantum information.

In chapter 5 we studied the generation of a light-matter quantum state that consists of the entanglement between a time-bin photonic qubit and a collective atomic spin excitation. We generated this state by using a magnetic field that dephases and rephases the excitation, allowing us to have two distinguishable spin-wave temporal modes. In order to analyse

the quantum state we built fiber Mach-Zehnder interferometers with a long delay of around 40 m. We certified the entanglement through the violation of a Bell inequality. The time-bin encoding of the photonic qubit is suitable for long distance transmission and quantum frequency conversion.

Finally in chapter 6 we used the photon tunablitiy capabilities described in chapter 3 and chapter 4 in order to transfer photonic quantum states from our system to two other different ones. In the first experiment of this kind we stored single photons generated by our system into Rydberg atomic excitations in a different atomic cloud. We showed that the quantum statistics of our photons are preserved after the Rydberg storage. The second experiment in this direction involved the qubit transfer from our system to a ion-doped crystal. This experiment represents the first photonic quantum stated transfer between long-lived matter systems with different atomic elements. This experiment required the frequency conversion of the single photons generated by our system from 780nm to 1550nm and later to 606nm to interact with the ions in the crystal. We transferred qubits between the two systems with fidelities exceeding the classical limit.

7.2 Contributions and collaborations

Some of the work described in this thesis was done in collaboration with projects that involved other researchers. The experiments described in chapter 3 and section 6.2 were done in collaboration with Nicolas Maring, who was the main responsible person for the quantum frequency conversion devices. The experiment in section 6.2 involved also the participation of Dr. Kultu Kutluer and Dr. Margherita Mazzera, who were the main responsible people for the ion-doped crystal setup. The connection with

the Rydberg system described in section 6.1 was done together with the people responsible of this setup, that were Dr. Emanuele Distante, Auxi Padrón and Dr. David Paredes. The theoretical simulations in chapter 4 were done by a theory team from the University of Basel formed by Dr. Melvyn Ho, Matías Chávez, Dr. Colin Teo and Prof. Nicolas Sangouard. I also want to mention Dr. Georg Heinze, who was a post-doctoral researcher involved in all the experiments described in this thesis, and Dr. Boris Albrecht and Dr. Matteo Cristiani, with whom I worked at the beginning of the thesis. All the work was conceived and supervised by Prof. Hugues de Riedmatten.

7.3 Future directions

The results presented in this thesis open possibilities for studying new experiments in different directions. These directions are explained in the following paragraphs.

The single photon storage as a Rydberg excitation was a proof of principle experiment that paves the way to study quantum nonlinear optics phenomena. If the Rydberg-induced optical non-linearity is increased and reaches the single photon regime then it would be possible to achieve deterministic interaction between two single photons. This interaction could be further used in order to make photonic two-qubit gates. In the context of quantum repeaters this would be a very interesting capability that could for instance enable deterministic photonic Bell state measurements.

Regarding the quantum state transfer to the doped crystal, this was also a first key step in the direction of hybrid photonic quantum networks. After

the shown qubit transfer, a future direction could be to to study the entanglement between these two long-lived hybrid systems. To achieve this, we could use the entanglement generation capability developed in chapter 5 in order to transfer to the crystal a photonic qubit that is entangled with the atoms in the laser-cooled atomic cloud. Another possibility would be to generate heralded entanglement between the two systems by performing a Bell state measurement on two photonic modes, each one entangled to one of the two systems. In addition, the frequency and bandwidth flexibility of our generated photons could allow us to extend the photonic quantum state transfer to other types of systems.

Finally, another direction would be to manipulate the phases of the collective excitations in order to build a light-matter entanglement source with temporal multiplexing capability. In chapter 5 we already used the magnetic filed dephasing in order to store two distinguishable spin-wave temporal modes forming an atomic time-bin qubit. Inducing a dephasing with a magnetic field gradient as shown in [120] and combining this with a low finesse cavity around the atoms, one could in principle achieve this multiplexing capability as proposed in [103]. This capability could enhance a lot the operation rate of the system in the context of a quantum repeater, which is currently one of the challenges to bring these repeater architectures from a theoretical concept into a working implementation.

In order to accomplish these future projects, it may be required to improve the performance of the DLCZ system. The storage lifetime of the spin-wave could be improved by using a magnetic field insensitive transition and by limiting the motion of the atoms with a optical lattice. With these techniques it has been shown that it is possible to extend the lifetime up to around 0.2 s [68]. In order to improve the read-out efficiency one

can surround the atomic ensemble with and optical cavity that enhances the atom-photon coupling strength. Using this technique several experiments have reached intrinsic read-out efficiencies around 80 % [68, 71, 73], although then one has also to consider the additional photon losses introduced by the cavity.

In conclusion, there is a broad range of possibilities in the future directions of our experiment. Having all these different possibilities highlights the versatility of this source of light-matter quantum states. On the horizon there is the ultimate goal to develop new technologies which take advantage of quantum physics effects, but on the way there is plenty of exciting physical phenomena to be understood.

Appendix A

Cauchy-Schwarz inequality for classical fields

In several of the experiments that are described in this thesis we measure the second order cross-correlation function $g^{(2)}_{\mathrm{a,b}} = \frac{\langle I_{\mathrm{a}}(t_{\mathrm{a}}) I_{\mathrm{b}}(t_{\mathrm{b}})\rangle}{\langle I_{\mathrm{a}}(t_{\mathrm{a}})\rangle\langle I_{\mathrm{b}}(t_{\mathrm{b}})\rangle}$. This quantity is used to asses the intensity (I) correlations between two photonic fields (here denoted a and b), which in our experiments they typically correspond to the write and read photons. In addition, it is also used as a witness that tells the quantum nature of the photon statistics shown by the optical fields that we generate. This is done through the inequality

$$\left[g^{(2)}_{\mathrm{a,b}}\right]^2 \leq g^{(2)}_{\mathrm{a,a}} \cdot g^{(2)}_{\mathrm{b,b}} \tag{A.1}$$

where $g^{(2)}_{\mathrm{a,a(b,b)}}$ corresponds to the autocorrelation of field a (b). This inequality is related to the mathematical Cauchy-Schwarz inequality and should be satisfied by any classical electromagnetic fields. The mathematical proof is explained in the next section following [229].

A.1 Mathematical demonstration

Let's consider $I_{\mathrm{a}}(t_{\mathrm{a}})$ and $I_{\mathrm{b}}(t_{\mathrm{b}})$ to be real-valued optical intensities. The delay between the times corresponding to the two fields ($\tau_{\mathrm{ab}} = t_{\mathrm{b}} - t_{\mathrm{a}}$) can take an arbitrary value. Eq. A.1 can be rewritten in the form

$$\langle I_{\mathrm{a}}(t_{\mathrm{a}}) I_{\mathrm{b}}(t_{\mathrm{b}}) \rangle^2 \leq \langle I_{\mathrm{a}}^2(t_{\mathrm{a}}) \rangle \langle I_{\mathrm{b}}^2(t_{\mathrm{b}}) \rangle \tag{A.2}$$

We can start by writing the average value $\langle I_{\mathrm{a}}^2(t_{\mathrm{a}}) \rangle$ within a given interval of time $t_{\mathrm{a}}^0 \leq t_{\mathrm{a}} \leq t_{\mathrm{a}}^1$. This value can be obtained by averaging over several measurements at different times $t_{\mathrm{a}}^j = t_{\mathrm{a}}^0 + j(t_{\mathrm{a}}^1 - t_{\mathrm{a}}^0)/N$ which are within the mentioned interval.

$$\left\langle I_{\mathrm{a}}^2(t_{\mathrm{a}}) \right\rangle = \frac{1}{N} \sum_{j=1}^{N} I_{\mathrm{a}}^2(t_{\mathrm{a}}^j) \tag{A.3}$$

A similar expression can be used for $\left\langle I_{\mathrm{b}}^2(t_{\mathrm{b}}) \right\rangle$ averaging over several measurements taken at times $t_{\mathrm{b}}^j = t_{\mathrm{a}}^j + \tau_{\mathrm{ab}}$. Using these expressions we can rewrite the right term of inequality (A.2) as

$$\begin{aligned} \langle I_{\mathrm{a}}^2(t_{\mathrm{a}}) \rangle \langle I_{\mathrm{b}}^2(t_{\mathrm{b}}) \rangle &= \frac{1}{N^2} \sum_{j=1}^{N} \sum_{k=1}^{N} I_{\mathrm{a}}^2(t_{\mathrm{a}}^j) I_{\mathrm{b}}^2(t_{\mathrm{b}}^k) = \\ &= \frac{1}{N^2} \sum_{j=1}^{N} \sum_{k=1}^{N} \frac{1}{2} \left[I_{\mathrm{a}}^2(t_{\mathrm{a}}^j) I_{\mathrm{b}}^2(t_{\mathrm{b}}^k) + I_{\mathrm{a}}^2(t_{\mathrm{a}}^k) I_{\mathrm{b}}^2(t_{\mathrm{b}}^j) \right] \end{aligned} \tag{A.4}$$

We can now focus on the left term of the inequality (A.2), which can be rewritten as

$$\begin{aligned}\langle I_{\mathrm{a}}(t_{\mathrm{a}})I_{\mathrm{b}}(t_{\mathrm{b}})\rangle^2 &= \left(\frac{1}{N}\sum_{j=1}^{N} I_{\mathrm{a}}(t_{\mathrm{a}}^j)I_{\mathrm{b}}(t_{\mathrm{b}}^j)\right)^2 = \\ &= \frac{1}{N^2}\sum_{k=1}^{N}\sum_{j=1}^{N} I_{\mathrm{a}}(t_{\mathrm{a}}^j)I_{\mathrm{b}}(t_{\mathrm{b}}^k)I_{\mathrm{a}}(t_{\mathrm{a}}^k)I_{\mathrm{b}}(t_{\mathrm{b}}^j)\end{aligned} \tag{A.5}$$

Now we can use the mathematical Cauchy-Schwarz inequality $x^2 + y^2 \geq 2xy$, which holds for any real numbers x and y. Considering this relation, we get that the expressions obtained in Eqs. (A.4) and (A.5) need to fulfil

$$\frac{1}{2}\left[I_{\mathrm{a}}^2(t_{\mathrm{a}}^j)I_{\mathrm{b}}^2(t_{\mathrm{b}}^k) + I_{\mathrm{a}}^2(t_{\mathrm{a}}^k)I_{\mathrm{b}}^2(t_{\mathrm{b}}^j)\right] \geq I_{\mathrm{a}}(t_{\mathrm{a}}^j)I_{\mathrm{b}}(t_{\mathrm{b}}^k)I_{\mathrm{a}}(t_{\mathrm{a}}^k)I_{\mathrm{b}}(t_{\mathrm{b}}^j) \tag{A.6}$$

Therefore it is straightforward to see that we obtained the result that we wanted to demonstrate, whis is

$$\langle I_{\mathrm{a}}(t_{\mathrm{a}})I_{\mathrm{b}}(t_{\mathrm{b}})\rangle^2 \leq \left\langle I_{\mathrm{a}}^2(t_{\mathrm{a}})\right\rangle \left\langle I_{\mathrm{b}}^2(t_{\mathrm{b}})\right\rangle \tag{A.7}$$

A.2 Photon statistics from the DLCZ scheme

In the quantum mechanical framework, light states can be represented as photon number states. The state of the photons generated by our experiment is introduced in subsection 1.2.4. Considering an ideal situation with perfect read-out efficiency, the write and read photons generated in the DLCZ scheme can be described by the state:

$$|\Psi\rangle = \sqrt{1-|\xi|^2}\left(\sum_{k=0}^{\infty}\xi^k\,|k_{\mathrm{w}}, k_{\mathrm{r}}\rangle\right) \tag{A.8}$$

In this expression, $p = |\xi|^2$ is the probability to create at least one photon pair and k is the number of photons generated in the write (w) and read (r) modes. In this section we want to calculate mathematically the cross-correlation and autocorrelation functions of the photonic modes described by this state, and evaluate them through the Cauchy-Schwarz inequality.

A.2.1 Normalized write-read photon second order cross-correlation function

Since the $g^{(2)}_{\mathrm{w,r}}$ function is normalized and the intensity I of a light field is proportional to the number of photons n, any of the two quantities (I and n) can be used for the calculation of $g^{(2)}_{\mathrm{w,r}}$. The photon number operator is defined in terms of the photon creation ($\hat{a}^\dagger$) and anihilation ($\hat{a}$) operators as $\hat{n} = \hat{a}^\dagger\hat{a}$ [229]. Therefore the second order cross-correlation function between two photonic modes is typically defined in a quantum mechanical framework as

$$g^{(2)}_{\mathrm{w,r}} = \frac{\langle\Psi| : \hat{n}_{\mathrm{w}}\hat{n}_{\mathrm{r}} : |\Psi\rangle}{\langle\Psi| : \hat{n}_{\mathrm{w}} : |\Psi\rangle \langle\Psi| : \hat{n}_{\mathrm{r}} : |\Psi\rangle} = \frac{\langle\Psi|\, \hat{a}^\dagger_{\mathrm{w}}\hat{a}^\dagger_{\mathrm{r}}\hat{a}_{\mathrm{r}}\hat{a}_{\mathrm{w}} \,|\Psi\rangle}{\langle\Psi|\, \hat{a}^\dagger_{\mathrm{w}}\hat{a}_{\mathrm{w}} \,|\Psi\rangle \langle\Psi|\, \hat{a}^\dagger_{\mathrm{r}}\hat{a}_{\mathrm{r}} \,|\Psi\rangle} \tag{A.9}$$

In this expression : : denotes the normal ordering of the photon operators and we have used the fact that photon operators of different modes commute between them. We can start by calculating the mean number of photons in the write mode.

$$\langle\Psi|\, \hat{a}^\dagger_{\mathrm{w}}\hat{a}_{\mathrm{w}} \,|\Psi\rangle = (\hat{a}_{\mathrm{w}} \,|\Psi\rangle)^\dagger\, \hat{a}_{\mathrm{w}} \,|\Psi\rangle = |\hat{a}_{\mathrm{w}} \,|\Psi\rangle|^2 = \frac{p}{1-p} \tag{A.10}$$

Since Eq. (A.8) remains the same when the write and read modes are interchanged, the mean photon number will be the same for the two modes: $\langle\Psi|\,\hat{a}_{\mathrm{r}}^{+}\hat{a}_{\mathrm{r}}\,|\Psi\rangle = {}^{p}/_{(1-p)}$. Now we just need to calculate the mean photon coincidence number

$$\langle\Psi|\,\hat{a}_{\mathrm{w}}^{\dagger}\hat{a}_{\mathrm{r}}^{\dagger}\hat{a}_{\mathrm{r}}\hat{a}_{\mathrm{w}}\,|\Psi\rangle = |\hat{a}_{\mathrm{r}}\hat{a}_{\mathrm{w}}\,|\Psi\rangle|^2 = \frac{p(1+p)}{(1-p)^2} \tag{A.11}$$

And finally we have the three terms that we need to calculate the expression of the second order cross correlation function:

$$g_{\mathrm{w,r}}^{(2)} = \frac{\langle\Psi|\,\hat{a}_{\mathrm{w}}^{\dagger}\hat{a}_{\mathrm{r}}^{\dagger}\hat{a}_{\mathrm{r}}\hat{a}_{\mathrm{w}}\,|\Psi\rangle}{\langle\Psi|\,\hat{a}_{\mathrm{w}}^{\dagger}\hat{a}_{\mathrm{w}}\,|\Psi\rangle\,\langle\Psi|\,\hat{a}_{\mathrm{r}}^{\dagger}\hat{a}_{\mathrm{r}}\,|\Psi\rangle} = 1 + \frac{1}{p} \tag{A.12}$$

A.2.2 Second order autocorrelation function of the write and read photons

Similarly to the cross correlation function, the second order autocorrelation function of a photonic mode can be defined in the quantum mechanical framework as

$$g_{\mathrm{w,w}}^{(2)} = \frac{\langle\Psi|:\hat{n}_{\mathrm{w}}\hat{n}_{\mathrm{w}}:|\Psi\rangle}{\langle\Psi|:\hat{n}_{\mathrm{w}}:|\Psi\rangle^2} = \frac{\langle\Psi|\,a_{\mathrm{w}}^{\dagger}a_{\mathrm{w}}^{\dagger}a_{\mathrm{w}}a_{\mathrm{w}}\,|\Psi\rangle}{\langle\Psi|\,a_{\mathrm{w}}^{\dagger}a_{\mathrm{w}}\,|\Psi\rangle^2} \tag{A.13}$$

The mean photon number was already calculated in the previous section to be $\langle\Psi|\,a_{\mathrm{w}}^{+}a_{\mathrm{w}}\,|\Psi\rangle = {}^{p}/_{(1-p)}$. Now we can calculate the mean two-photon coincidence number

$$\langle\Psi|\,\hat{a}_{\mathrm{w}}^{\dagger}\hat{a}_{\mathrm{w}}^{\dagger}\hat{a}_{\mathrm{w}}\hat{a}_{\mathrm{w}}\,|\Psi\rangle = |\hat{a}_{\mathrm{w}}\hat{a}_{\mathrm{w}}\,|\Psi\rangle|^2 = \frac{2p^2}{(1-p)^2} \tag{A.14}$$

And finally we have all the terms that we need to calculate the expression of the second order autocorrelation function:

$$g^{(2)}_{\mathrm{w,w}} = \frac{\langle\Psi|\,\hat{a}_{\mathrm{w}}^{\dagger}\hat{a}_{\mathrm{w}}^{\dagger}\hat{a}_{\mathrm{w}}\hat{a}_{\mathrm{w}}\,|\Psi\rangle}{\langle\Psi|\,\hat{a}_{\mathrm{w}}^{\dagger}\hat{a}_{\mathrm{w}}\,|\Psi\rangle^2} = 2 \tag{A.15}$$

As mentioned before, Eq. (A.8) is symmetric with respect to the write and read photonic modes. Therefore the autocorrelation function of the read photon mode is also $g^{(2)}_{\mathrm{r,r}} = 2$.

A.2.3 Cauchy-Schwarz inequality

Now we can use the expressions calculated for the correlation functions and evaluate them using inequality (A.1), obtaining that $g^{(2)}_{\mathrm{w,r}} = 1 + 1/p \leq 2$. It is clear that for the state that we considered, the correlation function $g^{(2)}_{\mathrm{w,r}}$ can take values that are much higher than 2. This is incompatible with the inequality, which was derived assuming classical light fields.

Appendix B

Autocorrelation bound for classical fields

In some of the experiments that are described in this thesis we study the statistics of the read photons that are heralded by a write photon detection. In this situation, their state should be similar to a single photon Fock state and one of the ways to analyse it is through the second-order correlation function $g^{(2)} = \langle I^2(t) \rangle / \langle I(t) \rangle^2$. This correlation function has a lower bound for classical light fields which is $g^{(2)} \geq 1$. In this section we derive mathematically this limit following the explanation in [229] and compare it with theoretical calculations of statistics from the photons generated in our experiment.

B.1 Mathematical demonstration

Let's consider $I(t)$ to be a real-valued optical intensity. We can start by writing the average value of the intensity within a given interval of

time $t_0 \leq t \leq t_1$. This value can be obtained by averging over several measurements at different times $t_j = t_0 + j(t_1 - t_0)/N$ which are within the mentioned interval.

$$\langle I(t) \rangle = \frac{1}{N} \sum_{j=1}^{N} I(t_j) \tag{B.1}$$

Now we can use this expression in order to rewrite the two terms in the equation of the autocorrelation function in the following way:

$$\left\langle I^2(t) \right\rangle = \frac{1}{N} \sum_{j=1}^{N} I^2(t_j) = \frac{1}{N^2} \sum_{j=1}^{N} \sum_{k=1}^{N} I^2(t_j) = \frac{1}{2N^2} \sum_{j=1}^{N} \sum_{k=1}^{N} \left[I^2(t_j) + I^2(t_k) \right] \tag{B.2}$$

$$\langle I(t) \rangle^2 = \left(\frac{1}{N} \sum_{j=1}^{N} I(t_j) \right)^2 = \frac{1}{N^2} \sum_{j=1}^{N} \sum_{k=1}^{N} I(t_j) I(t_k) \tag{B.3}$$

These expressions can be compared using the Cauchy-Schwarz inequality $x^2 + y^2 \geq 2xy$, which holds for any real numbers x and y. Applying this inequality to each term of the sums in expressions (B.2) and (B.3) it is straightforward to see that $\left\langle I^2(t) \right\rangle \geq \langle I(t) \rangle^2$. This leads us finally to the bound that we wanted to obtain, which is

$$g^{(2)} = \left\langle I^2(t) \right\rangle / \langle I(t) \rangle^2 \geq 1 \tag{B.4}$$

B.2 Photon statistics from the DLCZ scheme

In our experiment we expect single photon statistics when we measure the read photon autocorrelation function heralded on a write photon detection. This function can be expressed as a function of the photon detection probabilities as $g^{(2)}_{\mathrm{r,r|w}} = p_{\mathrm{r,r|w}}/p^2_{\mathrm{r|w}}$. In order to simplify the calculation we can rewrite the conditional probabilities ($p_{\mathrm{a|b}} = p_{\mathrm{a,b}}/p_{\mathrm{b}}$) and write the autocorrelation function as $g^{(2)}_{\mathrm{r,r|w}} = p_{\mathrm{w,r,r}}p_{\mathrm{w}}/p^2_{\mathrm{w,r}}$. In order to write the autocorrelation function in a quantum mechanical framework we can use the photon number operators. Following a similar argumentation as in subsection A.2.1 we obtain that:

$$g^{(2)}_{\mathrm{r,r|w}} = \frac{\langle\Psi| : \hat{n}_{\mathrm{w}}\hat{n}_{\mathrm{r}}\hat{n}_{\mathrm{r}} : |\Psi\rangle \langle\Psi| : \hat{n}_{\mathrm{w}} : |\Psi\rangle}{\langle\Psi| : \hat{n}_{\mathrm{w}}\hat{n}_{\mathrm{r}} : |\Psi\rangle^2} = \frac{\langle\Psi|\, \hat{a}^\dagger_{\mathrm{w}}\hat{a}^\dagger_{\mathrm{r}}\hat{a}^\dagger_{\mathrm{r}}\hat{a}_{\mathrm{r}}\hat{a}_{\mathrm{r}}\hat{a}_{\mathrm{w}} |\Psi\rangle \langle\Psi|\, \hat{a}^\dagger_{\mathrm{w}}\hat{a}_{\mathrm{w}} |\Psi\rangle}{\langle\Psi|\, \hat{a}^\dagger_{\mathrm{w}}\hat{a}^\dagger_{\mathrm{r}}\hat{a}_{\mathrm{r}}\hat{a}_{\mathrm{w}} |\Psi\rangle^2} \tag{B.5}$$

Now we can evaluate the previous expression with the photon state that is ideally produced by our experiment (cf. subsection 1.2.4 and Eq. (A.8)). In subsection A.2.1 we already mentioned the calculation of the terms $\langle\Psi|\, a^\dagger_{\mathrm{w}}a_{\mathrm{w}} |\Psi\rangle = p/(1-p)$ and $\langle\Psi|\, \hat{a}^\dagger_{\mathrm{w}}\hat{a}^\dagger_{\mathrm{r}}\hat{a}_{\mathrm{r}}\hat{a}_{\mathrm{w}} |\Psi\rangle = p(1+p)/(1-p)^2$. The caluculation to the third missing term gives:

$$\langle\Psi|\, \hat{a}^\dagger_{\mathrm{w}}\hat{a}^\dagger_{\mathrm{r}}\hat{a}^\dagger_{\mathrm{r}}\hat{a}_{\mathrm{r}}\hat{a}_{\mathrm{r}}\hat{a}_{\mathrm{w}} |\Psi\rangle = |\hat{a}_{\mathrm{r}}\hat{a}_{\mathrm{r}}\hat{a}_{\mathrm{w}} |\Psi\rangle|^2 = \frac{2p^2(2+p)}{(1-p)^3} \tag{B.6}$$

And finally we have all the terms that we need to calculate the expression of the heralded second order autocorrelation function:

$$g^{(2)}_{\mathrm{r,r|w}} = \frac{\langle\Psi|\,\hat{a}^\dagger_{\mathrm{w}}\hat{a}^\dagger_{\mathrm{r}}\hat{a}^\dagger_{\mathrm{r}}\hat{a}_{\mathrm{r}}\hat{a}_{\mathrm{r}}\hat{a}_{\mathrm{w}}\,|\Psi\rangle\,\langle\Psi|\,\hat{a}^\dagger_{\mathrm{w}}\hat{a}_{\mathrm{w}}\,|\Psi\rangle}{\langle\Psi|\,\hat{a}^\dagger_{\mathrm{w}}\hat{a}^\dagger_{\mathrm{r}}\hat{a}_{\mathrm{r}}\hat{a}_{\mathrm{w}}\,|\Psi\rangle^2} = \frac{2p(2+p)}{(1+p)^2} \tag{B.7}$$

We can see that when the photon creation probability p decreases, the autocorrelation function $g^{(2)}_{\mathrm{r,r|w}}$ approaches 0. This is incompatible with the inequality for the autocorrelation function given by Eq. (B.4), which was derived assuming classical light fields. It can be easily seen that for the considered state and low values of p the heralded autocorrelation function relates to the cross-correlation function as $g^{(2)}_{\mathrm{r,r|w}} \approx 4/g^{(2)}_{\mathrm{w,r}}$.

Appendix C

The Raman memory

For the optimization of several parameters that have a key role in our experiment, we implement a Raman read-write memory scheme [88]. We use this scheme to coherently transfer back and forth bright light pulses into atomic population in state $|s\rangle$. We can detect the retrieved output light with an avalanche photodiode (APD), which allows us to take experimental data much faster than in the single photon DLCZ experiment. We use the Raman memory signal in order to optimize parameters such as the homogeneous magnetic field, the beam alignment or the power and frequencies of the light beams used to prepare the atomic cloud.

C.1 Implementation and experimental scheme

In order to implement the Raman memory we use the DLCZ photonic fibre couplers, in a slightly different configuration. The Raman memory scheme is schematically represented in Fig. C.1 (a) and (b). We use the DLCZ write photon coupler to send the input light, which is overlapped with a

write coupling beam (sent along the DLCZ read pulse fibre coupler). The input light is mapped into a collective atomic excitations in state $|s\rangle$ via a two-photon transition with the write coupling beam. Both light fields have a red detuning of around 80 MHz with their respective transitions in order to avoid the excitation of state $|e\rangle$. After some time (so-called "storage time") we send a read coupling pulse, with similar parameters as the write coupling pulse. This pulse maps into an output light field the atomic population that was coherently transferred to $|s\rangle$. If the coherence of the atomic excitations is preserved, then the output field has the same frequency and spatial mode as the input light. We detect both input and output fields with an avalanche photodiode.

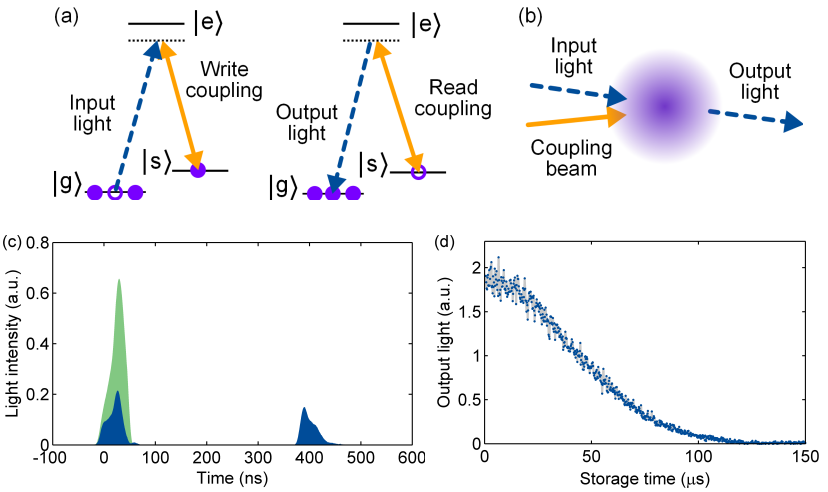

FIGURE C.1: (a) Schmatic drawing of the writing and reading processes in the Raman memory scheme. (b) Spatial distribution of the beams. (c) Input and output light pulse profiles without (green area) and with (blue area) atoms loaded in the MOT. (d) Output light signal as a function of the storage time.

In Fig. C.1c there is represented a typical signal of the probe light that we measure with the APD. The green data represents the situation with no atoms loaded in the MOT and therefore the input light is just transmitted through the setup. For the blue trace the atoms are loaded in the MOT

and we can see how the input probe is partially absorbed. At the time that the read coupling beam is switched on, the output light field is retrieved. The total efficiency of the storage and retrieval processes is 22%.

In Fig. C.1d we can see the amount of retrieved output light as a function of storage time. The Gaussian decay that we observe is due to the decoherence of the atomic excitations during the storage time. This Gaussian decay is similar to the one measured in the DLCZ experiment shown Fig. 4.3b. This trace can be taken in few seconds and we use it to optimize and characterize many parameters of the experiment as explained in the next sections.

C.2 Optimization of the atomic cloud preparation

One utility of the Raman memory configuration is to optimize the preparation of the atomic cloud. As mentioned in section 2.2 we always start our experiments by cooling and trapping ^{87}Rb atoms in a MOT, further cooling them later in an optical molasses stage, and finally performing optical pumping in the desired atomic level. These processes are carried out using different optical beams. The powers, frequencies and durations of these optical beams are optimized in order to trap the highest number of atoms and cool them to the lowest possible temperature. The number of trapped atoms has an impact in the efficiency of the Raman light storage process for a short storage time. The temperature of the atoms affects the storage lifetime τ_s.

As an example, Fig. C.2 shows the the intensity of the retrieved Raman signal at short storage time (green open circles) and the storage lifetime

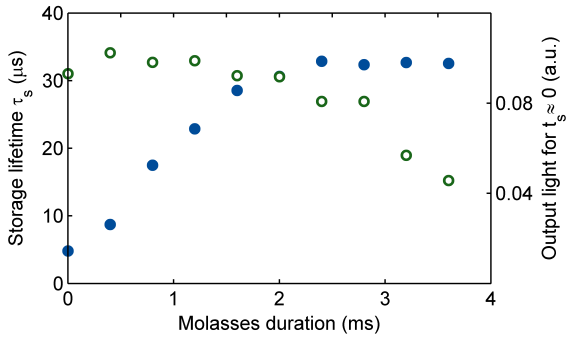

FIGURE C.2: Storage lifetime of the Raman memory (blue dots) and amount of output light retrieved at short storage time (green open circles) as a function of the molasses stage duration.

of the signal (blue dots). These values were obtained by fitting several traces similar as the one shown in Fig. C.1 (d), with different durations of the molasses stage. As it can be seen in the figure, when the duration of the molasses stage is increased τ_s increases as well, since the atoms become colder. However, the number of atoms in the cloud goes down, since during the molasses stage they are not trapped any longer. This affects the intensity of the retrieved signal at short storage times, which goes down when the molasses stage is longer. In our experiments we typically use a molasses stage duration around 1.5-2 ms, which is a time showing a trade-off on the optimization of both parameters shown in Fig. C.2.

C.3 Optimization of the magnetic field

Another remarkable utility of the Raman memory configuration is the optimization of the homogeneous magnetic field. For the correct operation of the experiments described in this thesis it is important to keep the magnetic field to the desired value. For this purpose we have three pairs of

electromagnetic coils in the Helmholtz configuration that can create homogeneous magnetic fields along three perpendicular axes. In most of the experiments described in this thesis we need the magnetic field pointing to a specific direction in order to be able to perform optical pumping in a given m_F Zeeman sublevel. In the photon-atom entanglement experiment we needed a specific orientation and value of the magnetic field in order to control the spin excitation dephasing and rephasing times. The Raman memory configuration turned out to be a very useful tool for the optimization of the magnetic field that we needed in each of the experiments.

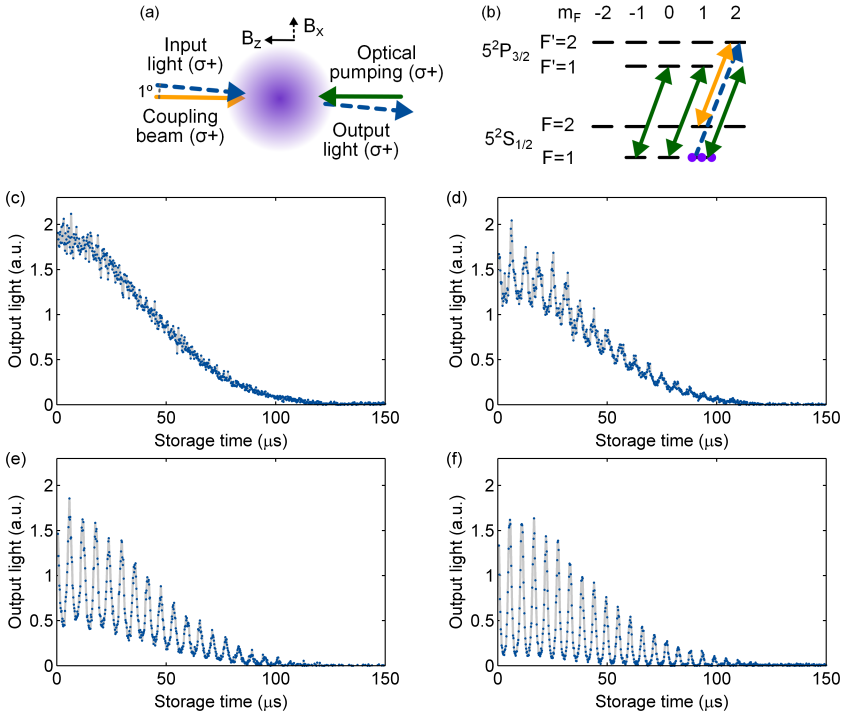

FIGURE C.3: (a) Schematic drawing of a Raman memory configuration with optical pumping in a Zeeman sublevel. σ^+ refers to the polarization of the light beams with respect to a fixed atomic frame. (b) ^{87}Rb atomic transitions coupled by the beams shown in (a) (same colour code) when the magnetic field is correctly aligned ($B_x = 0$). (c-f) Output light as a function of the storage time in four situations with different values for the homogeneous magnetic field B_x.

As an example of this magnetic field optimization we operate the Raman memory in the configuration shown in Figs. C.3(a-b). Figs. C.3(c-f) show the Raman memory signals for different magnetic fields. The points in each of the four plots represent the amount of output light retrieved for different storage times. In this situation we have a strong magnetic field B_z pointing in the same direction as an optical pumping beam that we use to initially prepare the atoms in the Zeeman sublevel $|g\rangle = \left|5^2S_{1/2}, F = 1, m_F = 1\right\rangle$. For the optimum initialization in the mentioned state, the optical pumping beam has to couple only σ^+ atomic transitions, such that atoms in $|g\rangle$ remain in the state. If the magnetic field does not point in the direction of the optical pumping beam then transitions different from the σ^+ ones can be coupled. In this situation the atomic preparation is not perfect and there are initially atoms in other Zeeman sublevels. This is what happens in Fig. C.3(d-f), where we gradually increase the magnetic field along a direction that is perpendicular to the optical pumping beam (B_x). In this situation we have multiple excitation processes taking place that interfere, giving rise to the oscillations that we observe in the the plots (see subsection D.1.2 for a more detailed explanation).

Appendix D

Decoherence mechanisms of collective atomic spin excitations

As shown in several of the experiments described in this thesis, the read-out efficiency decreases when increasing the storage time. This decrease is due to the dephasing of the collective spin excitation. This collective excitation can be mathematically described as

$$|\Psi_a\rangle = \frac{1}{N}\sum_{j=1}^{N} e^{i(\mathbf{k}_{\mathrm{W}}-\mathbf{k}_{\mathrm{w}})\cdot\mathbf{r}_j}\,|\mathrm{g}_1\ldots\mathrm{s}_j\ldots\mathrm{g}_N\rangle \tag{D.1}$$

as it is explained in subsection 1.2.4. If the phase factors are not affected during the storage time, then the excitation can be mapped efficiently into a single read photon. This happens thanks to the constructive interference effect from all the atoms involved in the collective read photon emission, which then happens into a single spatial mode given by

the phase matching condition $\mathbf{k}_\mathrm{r} = \mathbf{k}_\mathrm{W} - \mathbf{k}_\mathrm{w} + \mathbf{k}_\mathrm{R}$. However, if these phase factors are modified, then the read-out efficiency will be affected. There are different phenomena that affect the coherence of these spin-waves, and in this section we want to describe them and derive mathematically their impact on the read-out efficiency. The effect of decoherence on the intrinsic read-out efficiency (the probability to generate a read photon once a write photon was detected) can be computed using the expression $p^{\mathrm{int}}_{\mathrm{r|w}}(t_\mathrm{R}) \propto |\langle\Psi_a(t=0)|\Psi_a(t=t_\mathrm{R})\rangle|^2$. Here $\Psi_a(t=t_\mathrm{R})$ is the state of the dephased spin-wave at the read-out time t_R [67]. In the next section we develop these expressions for different dephasing mechanisms.

D.1 Magnetic field dephasing

Under the presence of a magnetic field, atoms experience a splitting of their spectral lines. This results in the separation of the so-called Zeeman sublevels with an energy detuning $\Delta E = \mu_B B g_F m_F$, where μ_B is the Bohr magneton, B is the magnetic field, g_F is the Landé g-factor and m_F the quantum number corresponding to the z-component of the total angular momentum [91]. This effect is shown in Fig. D.1 for the levels in the D2 line of ^{87}Rb that are involved in the creation of our spin-waves.

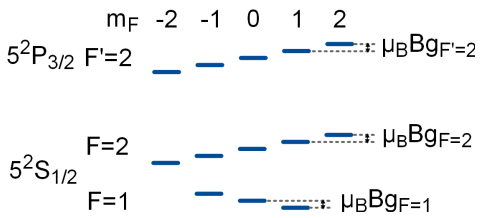

FIGURE D.1: Zeeman splitting of the atomic levels that are involved in the creation of our collective atomic spin excitations.

If the Zeeman shift is not the same for all the atoms that contribute to the spin-wave state, there is a dephasing of the spin-wave. This can be obtained mathematically using the Schrödinger equation to the compute time evolution of the state in Eq. (D.1) under the presence of a magnetic field. The result of this evolution is

$$|\Psi_a(t)\rangle = \frac{1}{\sqrt{N}} \sum_{j=1}^{N} e^{i(\mathbf{k}_W - \mathbf{k}_w)\cdot \mathbf{r}_j + i\int_0^t \Delta w_j(t')dt'} |g_1 ... s_j ... g_N\rangle \tag{D.2}$$

where $\Delta w_j = \mu_B B(g_{Fs} m_{Fs} - g_{Fg} m_{Fg})/\hbar$ is the relative detuning of each of the states $|g_1 ... s_j ... g_N\rangle$ [120]. Fs and Fg denote the total angular momentum of states $|s\rangle$ and $|g\rangle$ respectively. Assuming that the magnetic field is constant during the storage time we can rewrite the equation as

$$|\Psi_a(t)\rangle = \frac{1}{\sqrt{N}} \sum_{j=1}^{N} e^{i(\mathbf{k}_W - \mathbf{k}_w)\cdot \mathbf{r}_j + i\Delta w_j t} |g_1 ... s_j ... g_N\rangle \tag{D.3}$$

At this point we can distinguish two cases, the case where the magnetic field changes over the atomic region and the case that it is homogeneous.

D.1.1 Spatial gradient field

If the magnetic field is not the same for all the atoms, then the different states in the superposition experience a different phase evolution that depends on the position of the atom. In order to describe mathematically this situation we will consider a simplified picture of our experiment. We will consider a single pair of m_{Fg}-m_{Fs} Zeeman sublevels involved in the spin-wave, a one dimension atomic ensemble, and magnetic field changing linearly along this dimension $B(x) = B_g(x - x_0)$. Here B_g is the magnetic

field gradient amplitude and x_0 the position where $B = 0$. In this situation the atomic detunings depend on the position [$\Delta w_j = \Delta w(x_j)$], and we obtain that

$$p_{\mathrm{r|w}}^{\mathrm{int}}(t) \propto \left| \frac{1}{N} \sum_{j=1}^{N} e^{i\Delta w(x_j)t} \right|^2 \tag{D.4}$$

The spatial density of our atomic cloud follows a Gaussian profile, which in the one-dimensional case is expressed as $f(x) = \frac{1}{\sigma\sqrt{2\pi}} e^{-x^2/2\sigma^2}$. In this equation σ is the width of the distribution. We can replace the discrete sum over all the atoms by the spatial integral in the following way

$$p_{\mathrm{r|w}}^{\mathrm{int}}(t) \propto \left| \int_{-\infty}^{+\infty} f(x) e^{i\Delta w_k(x)t} dx \right|^2 \tag{D.5}$$

Now we just need to calculate the integral in order to obtain the final result, which is

$$p_{\mathrm{r|w}}^{\mathrm{int}}(t) \propto \mathrm{e}^{-(t/\tau)^2}, \quad \text{with} \quad \tau = \frac{\hbar}{\mu_B B_{\mathrm{g}} (g_{Fs} m_{Fs} - g_{Fg} m_{Fg}) \sigma} \tag{D.6}$$

D.1.2 Homogeneous field

If the magnetic field is spatially homogeneous over the atomic region and there is only one transition involved in the spin-wave creation, then there is no dephasing. This can be seen looking at Eq. D.3, in this situation the term $\Delta w_j t$ is the same for all the atoms and is just a global phase in the spin-wave equation. However, if there are different transitions involved in the spin-wave creation, then the splitting induced by the magnetic field will induce a different phase evolution for each of these transitions. In this

situation the probability to convert the collective excitation into a single read photon would be

$$p^{\mathrm{int}}_{\mathrm{r|w}}(t) \propto \left| \sum_{k=1}^{n_{\mathrm{p}}} P_k e^{i\Delta w_k t} \right|^2 \quad \text{with} \quad \Delta w_k = \mu_{\mathrm{B}} B (g_{Fs} m^k_{Fs} - g_{Fg} m^k_{Fg})/\hbar \quad \text{(D.7)}$$

where the different values of k represent the n_{p} different spin-wave excitation paths involving the m^k_{Fg} and m^k_{Fs} Zeeman sublevels, and the coefficients P_k correspond to the proportion of atoms that contribut to each path.

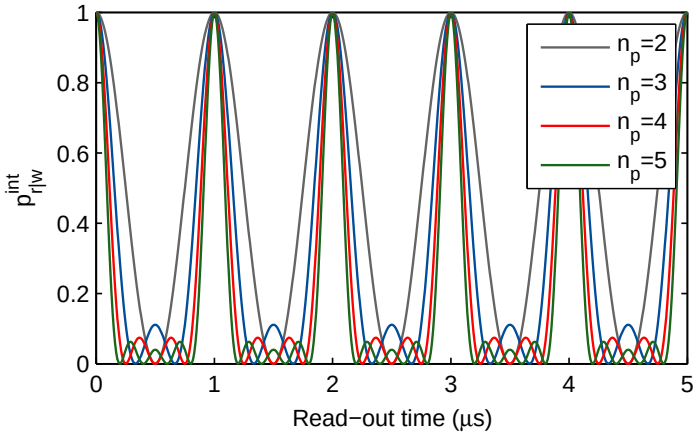

FIGURE D.2: Example calculation of the internal read-out efficiency as a function of the read-out time computed with Eq. D.7. The different curves denote different number of spin-wave excitation paths (n_{p}). More details about the parameters used in these curves are given in the text.

The periodicity in the level structure given by the Zeeman splitting (see Fig. D.1) will lead to periodic dephasing and rephasing of the spin-wave. This can also be seen by computing Eq. (D.7) and leads to a temporal modulation of the read-out efficiency. As an example, in Fig. D.2 we compute Eq. (D.7) considering $\Delta w_k = 2\pi(1\mathrm{MHz})k$ for different number of paths n_{p}. For simplicity we considered a balanced contribution from all the paths

(e.g. $P_k = 1/n_\mathrm{p}$). One experimental example of these collapses and revivals in the read-out efficiency can be seen in Fig. 5.2a.

D.2 Atomic motion dephasing

As it can be seen in Eq. (D.1), during the write process there is a phase pattern that is imprinted to the atoms that contribute to the spin-wave. If the atoms move during the storage time, this phase pattern will get blurred and this will have an impact on the wavefunction of the read photon [66, 67]. In particular, it will affect the constructive interference in the spatial mode $\boldsymbol{k}_\mathrm{r}$. The correct mathematical treatment for this dephasing that happens in the reading time, can be found in [230]. However one can obtain the same result by considering that this dephasing happens to the spin-wave during the storage time as described by the following equation

$$|\Psi_\mathrm{a}(t)\rangle = \frac{1}{\sqrt{N}} \sum_{j=1}^{N} \mathrm{e}^{\mathrm{i}(\mathbf{k}_\mathrm{W}-\mathbf{k}_\mathrm{w})\cdot(\mathbf{r}_j+\mathbf{v}_j t)} \, |g_1 ... s_j ... g_N\rangle \tag{D.8}$$

where $\mathbf{v}_j$ are the velocities of the atoms during the storage time. We can now calculate the impact of this dephasing on the readout efficiency as in the previous sections

$$p^\mathrm{int}_{\mathrm{r|w}}(t) \propto \left| \frac{1}{\sqrt{N}} \sum_j \mathrm{e}^{\mathrm{i}(\mathbf{k}_\mathrm{W}-\mathbf{k}_\mathrm{w})\cdot\mathbf{v}_j t} \right|^2 \tag{D.9}$$

In a gas in thermal equilibrium, the velocity of the atoms can described by the Maxwell-Botzmann distribution for idealized gases. This distribution is mathematically described as $f(\mathbf{v}) = (m/2\pi \mathrm{k_B} T)^{3/2} \, \mathrm{e}^{-m\mathbf{v}^2/2\mathrm{k_B}T}$, where

m is the mass of the atoms, k_{B} is the Boltzmann constant and T is the temperature of the atoms. Now we can replace the discrete sum over all the atoms in Eq. (D.9) by a velocity integral in the following way

$$p_{\mathrm{r|w}}^{\mathrm{int}}(t) \propto \left| \int_{\mathbf{v}} f(\mathbf{v}) \mathrm{e}^{-\mathrm{i}(\mathbf{k}_{\mathrm{W}}-\mathbf{k}_{\mathrm{w}})\cdot\mathbf{v}t} d\mathbf{v} \right|^2 \tag{D.10}$$

Using spherical coordinates one can solve this integral and obtain the final result, which is

$$p_{\mathrm{r|w}}^{\mathrm{int}}(t) \propto \mathrm{e}^{-(t/\tau)^2}, \quad \text{with} \quad \tau = \frac{\lambda}{4\pi \sin(\theta/2)} \sqrt{\frac{m}{\mathrm{k_B}T}} \tag{D.11}$$

In this last expression θ is the angle between the write pulse and write photon spatial modes and we have neglected the wavelength difference between write pulse and photons ($\lambda_{\mathrm{W}} \approx \lambda_{\mathrm{w}} = \lambda$).

D.3 Impact on the measured parameters

As mentioned in several times in this text, in our read-out process there is a collective interference effect such that spin-waves can be converted with a high efficiency into read photons emitted in a particular transition and direction. The ratio between the directional emission and the non-directional emission (e.g. spontaneous emission) depends, among other factors, on the preservation of the spin-wave coherence. In this section we want to describe the effect of this dephasing on two quantities that we typically measure: the read-out efficiency $p_{\mathrm{r|w}}$ and the write-read cross correlation function $g^{(2)}_{\mathrm{w,r}}$.

We can start by writing these quantities as a function of the photon detection probabilities $p_{\mathrm{r|w}} = p_{\mathrm{w,r}}/p_{\mathrm{w}}$ and $g^{(2)}_{\mathrm{w,r}} = p_{\mathrm{w,r}}/(p_{\mathrm{w}}p_{\mathrm{r}})$. Since the ratio between the read photon directional (d) and non-directional (nd) emission will depend on the storage time, we can write $p_{\mathrm{r}}(t) = p^{\mathrm{d}}_{\mathrm{r}}(t) + p^{\mathrm{nd}}_{\mathrm{r}}(t)$ and $p_{\mathrm{w,r}}(t) = p^{\mathrm{d}}_{\mathrm{w,r}}(t) + p_{\mathrm{w}}p^{\mathrm{nd}}_{\mathrm{r}}(t)$. The ratio of directional emission can be characterized by the intrinsic retrieval efficiency $p^{\mathrm{int}}_{\mathrm{r|w}}(t)$, while the non-directional emission is proportional the total number of atoms in the $|s\rangle$ ground state (N_s), the branching ratio of the read photon atomic transition (ξ_g), and the read photon spatial mode solid angle ($\Delta\Omega_{\mathrm{r}}$). Hence, we can write all the photon detection probabilities as:

$$p_{\mathrm{w}} = p\eta_{\mathrm{w}} \tag{D.12}$$

$$p_{\mathrm{r}}(t) = pp^{\mathrm{int}}_{\mathrm{r|w}}(t)\eta_{\mathrm{r}} + N_s[1 - p^{\mathrm{int}}_{\mathrm{r|w}}(t)]\frac{\Delta\Omega_{\mathrm{r}}}{4\pi}\xi_g\eta_{\mathrm{r}} \tag{D.13}$$

$$p_{\mathrm{w,r}}(t) = pp^{\mathrm{int}}_{\mathrm{r|w}}(t)\eta_{\mathrm{w}}\eta_{\mathrm{r}} + p\eta_{\mathrm{w}}N_s[1 - p^{\mathrm{int}}_{\mathrm{r|w}}(t)]\frac{\Delta\Omega_{\mathrm{r}}}{4\pi}\xi_g\eta_{\mathrm{r}} \tag{D.14}$$

where p is the probability to create a spin-wave together with a write photon in a specific spatial mode and $\eta_{\mathrm{w(r)}}$ are the write (read) photon total detection efficiencies. In the previous equations we have taken into account non-unity detection efficiencies, but we have not considered any noise.

Since write photons and excitations in state $|s\rangle$ are created in pairs, N_s can be expressed as a function of p and the write photon spatial mode solid angle $\Delta\Omega_{\mathrm{w}}$, with the expression $N_s = p4\pi/\Delta\Omega_{\mathrm{w}}$. In our experiment the solid angles of the write and read photonic modes are the same ($\Delta\Omega_{\mathrm{w}} = \Delta\Omega_{\mathrm{r}}$). The storage time dependence of the directional emission is

represented by $p^{\text{int}}_{\text{r|w}}(t)$ and will be given by the spin-wave dephasing, as it is mathematically derived in the previous sections. Introducing all the previous expressions in Eqs. (D.12)-(D.14), we can finally write the theoretical formulas that we typically use to fit our data.

$$p_{\text{r|w}}(t) = \eta_{\text{r}} \left[p^{\text{int}}_{\text{r|w}}(t)(1 - p\xi_g) + p\xi_g \right] \tag{D.15}$$

$$g^{(2)}_{\text{w,r}}(t) = 1 + \frac{p^{\text{int}}_{\text{r|w}}(t)(1-p)}{p\left[p^{\text{int}}_{\text{r|w}}(t)(1-\xi_g) + \xi_g \right]} \tag{D.16}$$

Appendix E

Laser linewidth limitation on the interference visiblity

In chapter 5 and section 6.2 we mention that the quality of the time-bin qubits that we measure is affected by the frequency fluctuations of our lasers. Frequency fluctuations of the light leads to fluctuations of the phase between the two time bins. Since our single photon qubit measurements consist of statistical averages over many trials, these phase fluctuations translate into a degradation of the interferometric measurements that we use to characterize the qubits.

To describe this effect we follow the explanation given in [231]. We can start by considering two light fields I_1 and I_2 that interfere giving an output intensity $I = I_1 + I_2 + 2\sqrt{I_1 I_2}\cos\phi$, where $\phi = \phi_2 - \phi_1$ is the phase difference between the two fields. In our experiments the two time bins of the qubit are overlapped by delaying the early bin. Therefore, we can write the phase as $\phi = \phi_0 - 2\pi\nu\Delta t$, where ϕ_0 is the initial phase difference between the two time bins, ν is the light frequency and Δt the temporal

delay applied to the early bin. Here we assume that the initial phase ϕ_0 does not depend on the frequency of the light, which is the case for instance when this is set by an acousto-optic modulator.

Now we can consider that there are fluctuations $\delta\nu$ in the light frequency. In this situation the phase will be given by $\phi(\delta\nu) = \phi_0 - 2\pi\Delta t(\nu + \delta\nu)$. We will also consider that the fluctuations follow a Gaussian probability distribution $\rho(\delta\nu) = \frac{1}{\sigma_\nu\sqrt{2\pi}} e^{-\delta\nu^2/2\sigma_\nu^2}$. In our experiment we typically measure intensities that are averaged over the frequency fluctuations that happen in the short time-scale. This average intensity can be mathematically calculated as

$$\langle I(\delta\nu)\rangle = \int_{-\infty}^{+\infty} \rho(\delta\nu) I(\delta\nu) d(\delta\nu) = I_1 + I_2 + 2\sqrt{I_1 I_2} e^{-2(\pi\Delta t\sigma_\nu)^2} \cos\phi \quad \text{(E.1)}$$

From this expression we can obtain the visibility of the interference fringes that we obtain when we interfere the two time bins of a time-bin qubit, which is

$$V = \frac{2\sqrt{I_1 I_2}}{I_1 + I_2} e^{-2(\pi\Delta t\sigma_\nu)^2} \quad \text{(E.2)}$$

Appendix F

Additional material for chapter 3

In this appendix we give more details about the experiment described in chapter 3. In particular we theoretically describe the effect of the quantum frequency conversion on the photon statistics.

F.1 Cross-correlation function after the photon's frequency conversion

During the frequency conversion process described in chapter 3, the write photons experience two kinds of imperfections. The first one is imperfect transmission and the second one is that they are mixed with noise photons (coming mainly from Raman scattering of pump light in the waveguide and detector dark counts). Considering these two effects, we can rewrite the photon detection probabilities as $p_{\mathrm{cw}} = \eta_{\mathrm{QFC}} p_{\mathrm{w}} + p_{\mathrm{N}}$ and $p_{\mathrm{cw,r}} = \eta_{\mathrm{QFC}} p_{\mathrm{w,r}} + p_{\mathrm{N}} p_{\mathrm{r}}$. In these expressions η_{QFC} is the total efficiency of the

quantum frequency conversion device (QFCD), p_{w} is the probability that a write photon arrives at the input of the QFCD and p_{N} is the probability to detect a noise photon. These effects can be included in the expression of the cross-correlation function $g^{(2)}_{\mathrm{cw,r}} = p_{\mathrm{cw,r}}/(p_{\mathrm{cw}}p_{\mathrm{r}})$.

$$g^{(2)}_{\mathrm{cw,r}} = \frac{\eta_{\mathrm{QFC}}p_{\mathrm{w,r}} + p_{\mathrm{N}}p_{\mathrm{r}}}{(\eta_{\mathrm{QFC}}p_{\mathrm{w}} + p_{\mathrm{N}})p_{\mathrm{r}}} = \frac{\frac{p_{\mathrm{w,r}}}{p_{\mathrm{w}}p_{\mathrm{r}}} + \frac{p_{\mathrm{N}}}{\eta_{\mathrm{QFC}}p_{\mathrm{w}}}}{1 + \frac{p_{\mathrm{N}}}{\eta_{\mathrm{QFC}}p_{\mathrm{w}}}} \tag{F.1}$$

From the previous expression we can identify two terms. The first one is the cross-correlation of the fields without any frequency conversion $g^{(2)}_{\mathrm{w,r}} = p_{\mathrm{w,r}}/(p_{\mathrm{w}}p_{\mathrm{r}})$ and the other one is the signal-to-noise-ration of the frequency converted photons $\mathrm{SNR} = (p_{\mathrm{cw}} - p_{\mathrm{N}})/p_{\mathrm{N}} = \eta_{\mathrm{QFC}}p_{\mathrm{w}}/p_{\mathrm{N}}$. Introducing this terms in Eq. (F.1) leads to the expression of Eq. (3.1)

$$g^{(2)}_{\mathrm{cw,r}} = \frac{g^{(2)}_{\mathrm{w,r}} + \mathrm{SNR}^{-1}}{1 + \mathrm{SNR}^{-1}} \tag{F.2}$$

This expression is used to asses how the frequency conversion process affects the cross-correlation function, as shown in Fig. 3.3a.

Appendix G

Additional material for chapter 4

G.1 Theoretical model for the generation of the write-read photon pairs

One important aspect of the experiment described in chapter 4 was to understand the limitations present in the duration tunability of the single photons. In order to understand this, we needed theoretical simulations that describe our system accurately. In particular we needed to describe the dynamics of the photon generation process. This was done by a theory group from the University of Basel led by Prof. Nicolas Sangouard. This section provides a light overview of the theoretical model, following the explanations in [127, 161, 232].

The starting point of the theoretical model are the Heisenberg-Langevin equations of motion for atomic operators and the propagation equation for

quantized fields. Starting from this point one can obtain the equations that describe the dynamics of the spin-wave and write photon fields (denoted respectively $\hat{S}$ and $\hat{\mathcal{E}}_{\mathrm{w}}$) under certain assumptions. These equations are written in [127] and are the following:

$$\begin{aligned} c\partial_{z'}\hat{\mathcal{E}}_{\mathrm{w}} &= i\sqrt{\frac{d_{\mathrm{w}}\gamma_{\mathrm{es}}c}{L}}\frac{\Omega_{\mathrm{W}}(t)}{\Delta}\hat{S}^{\dagger} \\ \partial_{t'}\hat{S}^{\dagger} &= -\left(\gamma_0 + \gamma_{\mathrm{es}}\frac{|\Omega_{\mathrm{W}}(t)|^2}{\Delta^2} - i\frac{|\Omega_{\mathrm{W}}(t)|^2}{\Delta}\right)\hat{S}^{\dagger} - i\sqrt{\frac{d_{\mathrm{w}}\gamma_{\mathrm{es}}c}{L}}\frac{\Omega_{\mathrm{W}}(t)}{\Delta}\hat{\mathcal{E}}_{\mathrm{w}} + \hat{F}_S^{\dagger} \end{aligned} \tag{G.1}$$

where d_{w} is optical depth of the $|e\rangle \rightarrow |s\rangle$ transition, γ_{es} the decay time of its coherence, L is the length of the atomic medium, $\Omega_{\mathrm{W}}(t)$ is the write pulse Rabi frequency and Δ its detuning from the $|g\rangle \rightarrow |e\rangle$ transition, γ_0 describes the decay of the $|g\rangle \rightarrow |s\rangle$ coherence and $\hat{F}_S$ is the Langevin "noise force" operator associated to $\hat{S}$. The coordinates used in these equations are $z' = z$ and $t' = t - z/c$. These equations can be solved as explained in [161] in order to obtain the expressions of $\hat{S}(z,t)$ and $\hat{\mathcal{E}}_{\mathrm{w}}(z,t)$.

The second step is to model the read-out process. The goal is to obtain the expresion for the read photon field $\hat{\mathcal{E}}_{\mathrm{r}}(z,t)$. In this situation again the quantized field propagation equation is used along with the Heisenberg-Langevin equations of motion for the atomic operators to obtain the equations that are written in [232] and are the following:

$$\begin{aligned}
\partial_z \hat{\mathcal{E}}_{\mathrm{r}} &= -i\sqrt{\frac{d_{\mathrm{r}}\gamma_{\mathrm{eg}}}{cL}}\hat{P} \\
\partial_t \hat{P} &= -(\gamma_{\mathrm{eg}} + i\Delta)\hat{P} + i\sqrt{\frac{d_{\mathrm{r}}\gamma_{\mathrm{eg}}c}{L}}\hat{\mathcal{E}} + i\Omega_{\mathrm{R}}(t)\hat{S} + \hat{F}_P \\
\partial_t \hat{S} &= -\gamma_0 \hat{S} + i\Omega_{\mathrm{R}}^*(t)\hat{P} + \hat{F}_S
\end{aligned} \tag{G.2}$$

where d_{r} is optical depth of the $|e\rangle \rightarrow |g\rangle$ transition $\Omega_{\mathrm{R}}(t)$ is the read pulse Rabi frequency, γ_{eg} describes the decay of the $|g\rangle \rightarrow |e\rangle$ coherence, $\hat{P}$ is the atomic operator $\hat{P}(z,t) = \sqrt{N}\sigma_{\mathrm{ge}}(z,t)e^{-iw_{\mathrm{eg}}(L-z)/c}$, $\hat{\sigma}_{\mu\nu} = \sum_j |\mu_j\rangle \langle\nu_j|$ and $\hat{F}_P$ is the Langevin "noise force" operator associated to $\hat{P}$.

After obtaining the expressions for the write and read photon fields, one can compute the heralded read photon flux inside the fiber. This is given by the expression

$$n_{\mathrm{r|w}}(t) = \frac{c}{L}\frac{\int \langle \hat{\mathcal{E}}_{\mathrm{w}}^\dagger(L,t_i)\hat{\mathcal{E}}_{\mathrm{r}}^\dagger(0,t)\hat{\mathcal{E}}_{\mathrm{r}}(0,t)\hat{\mathcal{E}}_{\mathrm{w}}(L,t_i)\rangle dt_i}{\int \langle \mathcal{E}_{\mathrm{w}}^\dagger(L,t_i)\mathcal{E}_{\mathrm{w}}(L,t_i)\rangle dt_i}\eta_{\mathrm{fiber}}. \tag{G.3}$$

where η_{fiber} is the coupling efficiency of the read emission into the first fiber. The obtained calculated values of $n_{\mathrm{r|w}}(t)$ using the parameters measured in our experiment, are the ones used in chapter 4 as theoretical simulation of the experimental results.

G.2 Read pulse adjustment

In order to optimize the read-out efficiency, we scanned the intensity of the driving read pulse for fixed photon durations. For short photon durations,

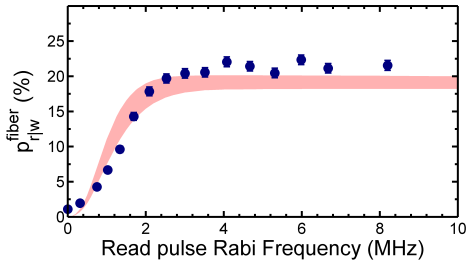

FIGURE G.1: Fiber-coupled conditional read-out efficiency $p_{r|w}^{fiber}$ vs read Rabi frequency Ω_R. Experimental data (blue dots) are compared with numerical simulations (red shaded area). The simulation is performed from Eq. (G.3) and uses the following values of the write pulse: a Rabi frequency of $\Omega_W = 25.1\,\text{MHz}$, a FWHM of 15 ns and a detuning by $-40\,\text{MHz}$ from the $|e\rangle \rightarrow |g\rangle$ transition. The peak Rabi frequency of the read pulse is varied and its FWHM is $1.27\,\mu\text{s}$. It has a delay of $2.16\,\mu\text{s}$ from the write peak. We take $d_w = 4.4$ and $d_r = 2.9$. An error of 10% on the Rabi frequencies, pulse widths, optical depths and spin coherence time was assumed in order to obtain the bounds on the simulation.

we observe the expected Rabi oscillations in the read-out efficiency vs. read pulse power [233]. If we generate photons with durations longer than the natural decay time, the oscillations are damped and the efficiency approaches a constant value for high read pulse intensities. Fig. G.1 shows such an example of the fiber-coupled conditional read-out efficiency as a function of the peak Rabi frequency Ω_R of the driving read pulse.

Appendix H

Additional material for chapter 5

In this appendix we give more details about the experiment described in chapter 5. In particular we describe the spin-wave rephasing process, characterize the single photon interference effect, and derive the CHSH Bell inequality that is used to certify the entanglement.

H.1 Periodic rephasing of the collective atomic excitation

One of the key features to generate the light-matter entangled state in our experiment, is an homogeneous magnetic field B that induces a periodic dephasing and rephasing of the collective atomic excitations. The theoretical description of this dephasing process is explained in subsection D.1.2, and the way this process takes place in our experiment is the following. After optically pumping the atoms in state $|g\rangle = |5^2S_{1/2}, F = 1\rangle$, a write

pulse with linear polarization parallel to the Y axis couples off-resonantly the $|g\rangle \rightarrow |e\rangle = |5^2P_{3/2}, F = 2\rangle$ transition (see Fig. H.1a). This polarization corresponds to a combination of σ^+ and σ^- in our chosen frame of reference and couples the Zeeman sublevels shown in Fig. H.1 b. Using a polarization beam splitter we couple into a single mode fiber write photons that are linearly polarized along the Z axis, which are generated from π atomic transitions. The detection of a write photon heralds the presence of a collective atomic excitation (one atom in $|s\rangle = |5^2S_{1/2}, F = 2\rangle$) described by Eq. D.1. The interference between the different excitation paths, leads to a modulation of the read-out efficiency given by Eq. D.7, which is rewritten here:

$$p_{\mathrm{r|w}}(t) \propto \left| \sum_{k=0}^{3} P_k e^{-i\Delta w_k t} \right|^2 \tag{H.1}$$

As explained in more detail in Appendix D.1.2, $\Delta w_k = \mu_B B(g_{F=2}m_{F=2} - g_{F=1}m_{F=1})/\hbar$, the different values of k represent the four different excitation paths, and the coefficients P_k correspond to the ratio of atoms that contributed to each path. Considering the excitation paths shown in Fig. H.1 b it is important to note that the two paths $|F = 1, m_F = \pm 1\rangle \rightarrow |F = 2, m_F = \pm 2\rangle$ involve transitions with much stronger dipole moments than the ones involved in the two paths $|F = 1, m_F = 0\rangle \rightarrow |F = 2, m_F = \pm 1\rangle$. This is the reason that the blue data in Fig. 5.2a exhibits a temporal dependence very similar to a sinusoidal trace, which is the behaviour expected when there are two spin-wave excitation paths (cf. Appendix D.1.2). The two strong paths also show a 3 times larger difference between the their associated values of Δw_k, in comparison to the weaker paths. This leads to a 3 times faster oscillation of $p_{\mathrm{r|w}}(t)$.

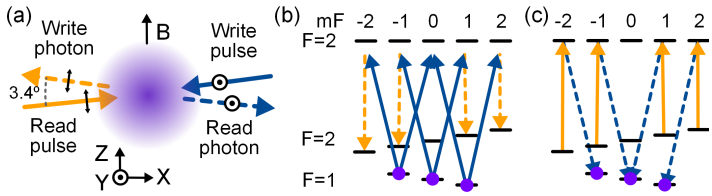

FIGURE H.1: (a) Schematic drawing of the atomic cloud and the four light fields involved in the entanglement generation process. The black arrows and dots above the optical beams represent their polarization. (b-c) Atomic levels with the coupled optical transitions for the write process (b) and the read process (c). The Zeeman splitting of the excited state is not shown in order to avoid any confusion with the optical detunings.

To fit the data in Fig. 5.2a we use Eq. (H.1) multiplied by a proportional factor C_p and with an added offset C_o. The proportional factor C_p accounts for the effects different to spin-wave dephasing that decrease the value of $p_{\mathrm{r|w}}$ in our experiment. This includes the imperfect fiber coupling efficiency or the detection in the write process of photons emitted in the $|e\rangle \rightarrow |g\rangle$ transition leading to wrong heralding events. The offset factor C_o includes detector dark counts and the amount of non-directionally emitted photons that are coupled to the read photon fiber and detected. The expression of coefficients Δw_k is mentioned before and from the values given by the fit we obtain the homogeneous magnetic field value $B = 0.67\,\mathrm{G}$ mentioned in subsection 5.2.1.

H.2 Single photon interference of the write and read photons

As shown in Fig. 5.2b, we observe strong photon correlations between both early and both late write and read photonic bins. This means that by measuring one of the photonic modes (either the write or the read) one could get information about the temporal bin of the other mode. A consequence

is that we should not see single photon interference when the two bins of one mode are overlapped in the interferometer. However, as shown in Fig. H.2 we do observe single photon interference. In this figure we show the number of read photons detected in detectors D_r^+ (blue dots) and D_r^- (green circles) for the measurement shown in Fig. 5.3c. They correspond to all counts in the read photon central bin shown in Fig. 5.3a. They oscillate with a visibility of $V \approx 24\%$ when the read photon interferometer phase is changed by the voltage U_r applied to its piezo fiber stretcher. When scanning the voltage of the write piezo stretcher, we also observe single photon interference in the write mode with a similar visibility ($V \approx 23\%$).

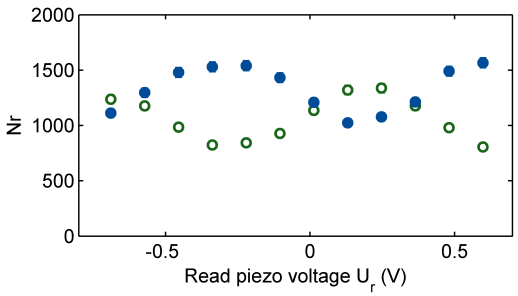

FIGURE H.2: Number of detected read photons (N_r) as a function of the voltage applied to the piezoelectric cylinder in the read interferometer. The blue dots and the green open circles represent the counts detected at each of the two outputs of the read interferometer in detectors D_r^+ and D_r^- (see Fig. 5.1a).

We attribute this effect to write photons that are emitted in the $|e\rangle \rightarrow |g\rangle$ transition and read photons emitted in the $|e\rangle \rightarrow |s\rangle$ transition. These photons are not part of the entangled state that is described in the main text and represent noise that decreases the entanglement fidelity. Nevertheless since these photons do not show write-read photon correlations, their impact in the correlation parameters E (which are calculated from write-read photon coincidence probabilities) is very low. Due to the fact that the frequency of these photons is 6.8 GHz away from the one of the

entangled write and read photons, they could be filtered out by our Fabry-Perot cavities (cf. section 2.3). However, in this experiment we did not use spectral filtering in order to have higher photon detection rates and hence reduce the effect of long term instabilities.

H.3 CHSH Bell Inequality

As mentioned in subsection 5.2.3 the verification of the entanglement is done through the violation of a CHSH Bell inequality [177, 234]. In this section we provide the mathematical derivation of the inequality taking [235] as reference, and explain how it adapts to the conditions of our experiment.

H.3.1 CHSH inequality in a standard Bell test

In a standard Bell test scenario, there are two particles that are measured in two measurement locations (commonly called Alice and Bob). Alice can choose to perform measurement A with two different measurements settings (a or a') and Bob can perform measurement B with settings b or b'. Both measurements A and B can give as a result +1 or -1 (for any measurement settings).

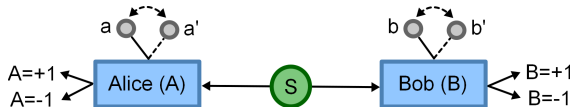

FIGURE H.3: Schematic representation of a standard Bell test. Two particles generated by source S are measured in Alice's and Bob's locations. Two measurements settings can be used in each of the locations: a and a' in Alice's, and b and b' in Bob's. For both measurements the possible outcomes can be +1 or -1.

The CHSH Bell inequality states that

$$E(a,b) + E(a',b) + E(a,b') - E(a',b') \leq 2 \tag{H.2}$$

where $E(x,y)$ is a correlation coefficient that denotes the mean value of the product of measurements A and B, taken respectively with settings x and y. Expressed in mathematical terms $E(x,y) = \langle A(x)B(y)\rangle$.

Quantum theory allows for intrinsic randomness in the outcomes of the measurements. However, if the indeterminacy of quatum theory was due local hidden variables λ then we could write the correlation coefficients as $E(a,b) = \int d\lambda \rho(\lambda) A(a,\lambda)B(b,\lambda)$, where $\rho(\lambda)$ is the probability density associated to λ. There are two aspects that are relevant to point out regarding this expression and the derivation of the Bell inequality. The first one is that locality is imposed by not allowing Alice's measurement A depend on Bob's measurement settings b, and vice-versa. The second one is that the idea of realism is also used by considering that the values of $A(a,\lambda)$ and $A(a',\lambda)$ (and also $B(b,\lambda)$ and $B(b',\lambda)$) can be simultaneously defined. To prove the inequality we proceed as follows

$$\begin{aligned} E(a,b) - E(a',b') &= \int d\lambda \rho(\lambda) \left[A(a,\lambda)B(b,\lambda) - A(a',\lambda)B(b',\lambda)\right] = \\ &= \int d\lambda \rho(\lambda) A(a,\lambda)B(b,\lambda) \left[1 - A(a',\lambda)B(b',\lambda)\right] \\ &\quad - \int d\lambda \rho(\lambda) A(a',\lambda)B(b',\lambda) \left[1 - A(a,\lambda)B(b,\lambda)\right] \end{aligned} \tag{H.3}$$

where we have subtracted the same expression in the two terms of the original sum. The product AB has to take values between -1 and 1 and therefore we can write that

$$\begin{aligned} \left|E(a,b') - E(a',b')\right| \leq & \int d\lambda \rho(\lambda) \left[1 - A(a',\lambda)B(b,\lambda)\right] + \\ & + \int d\lambda \rho(\lambda) \left[1 - A(a,\lambda)B(b,\lambda)\right] = \\ & = 2 - E(a',b) - E(a,b) \end{aligned} \tag{H.4}$$

This equation is the proof that we wanted to reach. Any measurement in a pair of particles that follows the Bell scenario described in Fig. H.3 and local realism, should fullfill the inequality.

Quantum theory tells that for pairs of qubits the correlation coefficients can be calculated as

$$E(a,b) = \langle \Psi | \, \hat{A} \otimes \hat{B} \, | \Psi \rangle \tag{H.5}$$

In this expression $|\Psi\rangle$ describes the state of the two qubits, and the observables can be expressed as $\hat{A} = \vec{a} \cdot \hat{\vec{\sigma}}$ and $\hat{B} = \vec{b} \cdot \hat{\vec{\sigma}}$, where $\hat{\vec{\sigma}}$ is the Pauli vector and $\{\vec{a}, \vec{b}\}$ are unitary vectors that depend on the measurement settings. It can be shown that for a particular combination of measurement settings, some quantum states violate the inequality shown in Eq. (H.2). In particular, maximally entangled quantum states as the one described by Eq. (5.2) can violate the inequality and reach a maximum CHSH Bell parameter of $S = 2\sqrt{2}$. Due to this discrepancy, Bell tests are used to certify the presence of quantum correlations and entanglement, as we use in our experiment.

H.3.2 Bell test in the context of our experiment

The Bell test that we describe in chapter 5 is related to the scenario mentioned in the previous section in the following way. The write and read photons are the two entangled objects that Alice and Bob measure with their respective interferometers. The different measurement settings a, a', b and b' correspond to the different phase delays of the two interferometer ϕ_{w}, ϕ'_{w}, ϕ_{r} and ϕ'_{r}. They are set by applying different voltages to the piezo fiber stretchers of the interferometers. In our situation, a result $A, B = +1(-1)$ represents a photon being detected in detectors $\mathrm{D}^{+(-)}$. In this situation it can be easily seen that the mean value of the product of the two measurements A and B can be calculated as

$$E(a,b) \equiv E(\phi_{\mathrm{w}}, \phi_{\mathrm{r}}) = \frac{p_{++} - p_{+-} - p_{-+} + p_{--}}{p_{++} + p_{+-} + p_{-+} + p_{--}} \tag{H.6}$$

where $p_{i,j}$ correspond to the probability to detect a photon coincidence between Alice's detector $\mathrm{D}^i_{\mathrm{w}}$ and Bob's detector $\mathrm{D}^j_{\mathrm{r}}$ $(i, j = \pm)$. This is the equation that we use in chapter 5 in order to characterize our entangled state and test the Bell inequality.

Bibliography

[1] N. Gisin, G. Ribordy, W. Tittel, and H. Zbinden: *Quantum cryptography*, Reviews of Modern Physics **74**, 145 (2002).

[2] T. D. Ladd, F. Jelezko, R. Laflamme, Y. Nakamura, et al.: *Quantum computers*, Nature **464**, 45 (2010).

[3] I. Buluta and F. Nori: *Quantum Simulators*, Science **326**, 108 (2009).

[4] V. Giovannetti: *Quantum-Enhanced Measurements: Beating the Standard Quantum Limit*, Science **306**, 1330 (2004).

[5] P. Kómár, E. M. Kessler, M. Bishof, L. Jiang, et al.: *A quantum network of clocks*, Nature Physics **10**, 582 (2014).

[6] D. E. Chang, V. Vuletić, and M. D. Lukin: *Quantum nonlinear optics — photon by photon*, Nature Photonics **8**, 685 (2014).

[7] M. Afzelius, N. Gisin, and H. de Riedmatten: *Quantum memory for photons*, Physics Today **68**, 42 (2015).

[8] H.-J. Briegel, W. Dür, J. I. Cirac, and P. Zoller: *Quantum Repeaters: The Role of Imperfect Local Operations in Quantum Communication*, Physical Review Letters **81**, 5932 (1998).

[9] N. Sangouard, C. Simon, H. de Riedmatten, and N. Gisin: *Quantum repeaters based on atomic ensembles and linear optics*, Reviews of Modern Physics **83**, 33 (2011).

[10] B. Korzh, C. C. W. Lim, R. Houlmann, N. Gisin, et al.: *Provably secure and practical quantum key distribution over 307 km of optical fibre*, Nature Photonics **9**, 163 (2015).

[11] J. Yin, Y. Cao, Y.-H. Li, S.-K. Liao, et al.: *Satellite-based entanglement distribution over 1200 kilometers.*, Science (New York, N.Y.) **356**, 1140 (2017).

[12] L.-M. Duan, M. D. Lukin, J. I. Cirac, and P. Zoller: *Long-distance quantum communication with atomic ensembles and linear optics*, Nature **414**, 413 (2001).

[13] K. Hammerer, A. S. Sørensen, and E. S. Polzik: *Quantum interface between light and atomic ensembles*, Reviews of Modern Physics **82**, 1041 (2010).

[14] B. B. Blinov, D. L. Moehring, L.-M. Duan, and C. Monroe: *Observation of entanglement between a single trapped atom and a single photon*, Nature **428**, 153 (2004).

[15] J. Volz, M. Weber, D. Schlenk, W. Rosenfeld, et al.: *Observation of entanglement of a single photon with a trapped atom*, Physical Review Letters **96**, 030404 (2006).

[16] T. Wilk, S. C. Webster, A. Kuhn, and G. Rempe: *Single-Atom Single-Photon Quantum Interface*, Science **317**, 488 LP (2007).

[17] D. N. Matsukevich, T. Chanelière, M. Bhattacharya, S.-Y. Lan, et al.: *Entanglement of a Photon and a Collective Atomic Excitation*, Physical Review Letters **95**, 040405 (2005).

[18] H. de Riedmatten, J. Laurat, C. W. Chou, E. W. Schomburg, et al.: *Direct Measurement of Decoherence for Entanglement between a Photon and Stored Atomic Excitation*, Physical Review Letters **97**, 113603 (2006).

[19] C. Clausen, I. Usmani, F. Bussières, N. Sangouard, et al.: *Quantum storage of photonic entanglement in a crystal*, Nature **469**, 508 (2011).

[20] E. Saglamyurek, N. Sinclair, J. Jin, J. A. Slater, et al.: *Broadband waveguide quantum memory for entangled photons*, Nature **469**, 512 (2011).

[21] E. Togan, Y. Chu, A. S. Trifonov, L. Jiang, et al.: *Quantum entanglement between an optical photon and a solid-state spin qubit*, Nature **466**, 730 (2010).

[22] W. B. Gao, P. Fallahi, E. Togan, J. Miguel-Sanchez, et al.: *Observation of entanglement between a quantum dot spin and a single photon*, Nature **491**, 426 (2012).

[23] K. De Greve, L. Yu, P. L. McMahon, J. S. Pelc, et al.: *Quantum-dot spin–photon entanglement via frequency downconversion to telecom wavelength*, Nature **491**, 421 (2012).

[24] C. W. Chou, H. de Riedmatten, D. Felinto, S. V. Polyakov, et al.: *Measurement-induced entanglement for excitation stored in remote atomic ensembles*, Nature **438**, 828 (2005).

[25] D. L. Moehring, P. Maunz, S. Olmschenk, K. C. Younge, et al.: *Entanglement of single-atom quantum bits at a distance*, Nature **449**, 68 (2007).

[26] M. Lettner, M. Mücke, S. Riedl, C. Vo, et al.: *Remote Entanglement between a Single Atom and a Bose-Einstein Condensate*, Physical Review Letters **106**, 210503 (2011).

[27] S. Ritter, C. Nölleke, C. Hahn, A. Reiserer, et al.: *An elementary quantum network of single atoms in optical cavities*, Nature **484**, 195 (2012).

[28] I. Usmani: *Heralded quantum entanglement between two crystals*, Nat. Photon. **6**, 234 (2012).

[29] R. Riedinger, A. Wallucks, I. Marinković, C. Löschnauer, et al.: *Remote quantum entanglement between two micromechanical oscillators*, Nature **556**, 473 (2018).

[30] S. Olmschenk, D. N. Matsukevich, P. Maunz, D. Hayes, et al.: *Quantum Teleportation Between Distant Matter Qubits*, Science **323**, 486 (2009).

[31] X.-H. Bao, X.-F. Xu, C.-M. Li, Z.-S. Yuan, et al.: *Quantum teleportation between remote atomic-ensemble quantum memories*, Proceedings of the National Academy of Sciences **109**, 20347 (2012).

[32] C. Nölleke, A. Neuzner, A. Reiserer, C. Hahn, et al.: *Efficient teleportation between remote single-atom quantum memories*, Physical Review Letters **110**, 1 (2013).

[33] C.-W. Chou, J. Laurat, H. Deng, K. S. Choi, et al.: *Functional Quantum Nodes for Entanglement Distribution over Scalable Quantum Networks*, Science **316**, 1316 LP (2007).

[34] Z.-S. Yuan, Y.-A. Chen, B. Zhao, S. Chen, et al.: *Experimental demonstration of a BDCZ quantum repeater node*, Nature **454**, 1098 (2008).

[35] B. Hensen, H. Bernien, A. E. Dréau, A. Reiserer, et al.: *Loophole-free Bell inequality violation using electron spins separated by 1.3 kilometres*, Nature **526**, 682 (2015).

[36] W. Rosenfeld, D. Burchardt, R. Garthoff, K. Redeker, et al.: *Event-Ready Bell Test Using Entangled Atoms Simultaneously Closing Detection and Locality Loopholes*, Physical Review Letters **119**, 010402 (2017).

[37] A. Stute, B. Casabone, P. Schindler, T. Monz, et al.: *Tunable ion–photon entanglement in an optical cavity*, Nature **485**, 482 (2012).

[38] T. G. Tiecke, J. D. Thompson, N. P. de Leon, L. R. Liu, et al.: *Nanophotonic quantum phase switch with a single atom*, Nature **508**, 241 (2014).

[39] B. Gouraud, D. Maxein, A. Nicolas, O. Morin, et al.: *Demonstration of a Memory for Tightly Guided Light in an Optical Nanofiber*, Physical Review Letters **114**, 1 (2015).

[40] C. Sayrin, C. Clausen, B. Albrecht, P. Schneeweiss, et al.: *Storage of fiber-guided light in a nanofiber-trapped ensemble of cold atoms*, Optica **2**, 353 (2015).

[41] A. Goban, C.-L. Hung, J. D. Hood, S.-P. Yu, et al.: *Superradiance for Atoms Trapped along a Photonic Crystal Waveguide*, Physical Review Letters **115**, 063601 (2015).

[42] S. Welte, B. Hacker, S. Daiss, S. Ritter, et al.: *Cavity Carving of Atomic Bell States*, Physical Review Letters **118**, 210503 (2017).

[43] B. Hacker, S. Welte, G. Rempe, and S. Ritter: *A photon–photon quantum gate based on a single atom in an optical resonator*, Nature **536**, 193 (2016).

[44] D. Tiarks, S. Schmidt, G. Rempe, and S. Du rr: *Optical phase shift created with a single-photon pulse*, Science Advances **2**, e1600036 (2016).

[45] H. Busche, P. Huillery, S. W. Ball, T. Ilieva, et al.: *Contactless nonlinear optics mediated by long-range Rydberg interactions*, Nature Physics **13**, 655 (2017).

[46] M. Zhong, M. P. Hedges, R. L. Ahlefeldt, J. G. Bartholomew, et al.: *Optically addressable nuclear spins in a solid with a six-hour coherence time*, Nature **517**, 177 (2015).

[47] M. Körber, O. Morin, S. Langenfeld, A. Neuzner, et al.: *Decoherence-protected memory for a single-photon qubit*, Nature Photonics **12**, 18 (2018).

[48] J. Nunn, K. T. Kaczmarek, P. M. Ledingham, B. Brecht, et al.: *QLad: A Noise-Free Quantum Memory for Broadband Light at Room Temperature*, in *Conference on Lasers and Electro-Optics*, FM2E.2, OSA, Washington, D.C. (2017).

[49] J. Wolters, G. Buser, A. Horsley, L. Béguin, et al.: *Simple Atomic Quantum Memory Suitable for Semiconductor Quantum Dot Single Photons*, Physical Review Letters **119**, 060502 (2017).

[50] A. Nicolas, L. Veissier, L. Giner, E. Giacobino, et al.: *A quantum memory for orbital angular momentum photonic qubits*, Nature Photonics **8**, 234 (2014).

[51] V. Parigi, V. D'Ambrosio, C. Arnold, L. Marrucci, et al.: *Storage and retrieval of vector beams of light in a multiple-degree-of-freedom quantum memory*, Nature Communications **6**, 7706 (2015).

[52] E. Saglamyurek, J. Jin, V. B. Verma, M. D. Shaw, et al.: *Quantum storage of entangled telecom-wavelength photons in an erbium-doped optical fibre*, Nature Photonics **9**, 83 (2015).

[53] M. Rančić, M. P. Hedges, R. L. Ahlefeldt, and M. J. Sellars: *Coherence time of over a second in a telecom-compatible quantum memory storage material*, Nature Physics **14**, 50 (2017).

[54] A. G. Radnaev, Y. O. Dudin, R. Zhao, H. H. Jen, et al.: *A quantum memory with telecom-wavelength conversion*, Nature Physics **6**, 894 (2010).

[55] Y. O. Dudin, A. G. Radnaev, R. Zhao, J. Z. Blumoff, et al.: *Entanglement of Light-Shift Compensated Atomic Spin Waves with Telecom Light*, Physical Review Letters **105**, 260502 (2010).

[56] S. Zaske, A. Lenhard, C. A. Keßler, J. Kettler, et al.: *Visible-to-Telecom Quantum Frequency Conversion of Light from a Single Quantum Emitter*, Physical Review Letters **109**, 147404 (2012).

[57] B. Albrecht, P. Farrera, X. Fernandez-Gonzalvo, M. Cristiani, et al.: *A waveguide frequency converter connecting rubidium-based quantum memories to the telecom C-band.*, Nature communications **5**, 3376 (2014).

[58] M. Bock, P. Eich, S. Kucera, M. Kreis, et al.: *High-fidelity entanglement between a trapped ion and a telecom photon via quantum frequency conversion*, Nature Communications **9**, 1998 (2018).

[59] V. Krutyanskiy, M. Meraner, J. Schupp, and B. P. Lanyon: *Polarisation-preserving photon frequency conversion from a trapped-ion-compatible wavelength to the telecom C-band*, Applied Physics B **123**, 228 (2017).

[60] A. Dréau, A. Tcheborateva, A. E. Mahdaoui, C. Bonato, et al.: *Quantum frequency conversion to telecom of single photons from a nitrogen-vacancy center in diamond*, arxiv **1801.03304** (2018).

[61] N. Maring, D. Lago-Rivera, A. Lenhard, G. Heinze, et al.: *Quantum frequency conversion of memory-compatible single photons from 606 nm to the telecom C-band*, Optica **5**, 507 (2018).

[62] A. Kuzmich, W. P. Bowen, A. D. Boozer, A. Boca, et al.: *Generation of nonclassical photon pairs for scalable quantum communication with atomic ensembles*, Nature **423**, 731 (2003).

[63] C. H. van der Wal: *Atomic Memory for Correlated Photon States*, Science **301**, 196 (2003).

[64] S. V. Polyakov, C. W. Chou, D. Felinto, and H. J. Kimble: *Temporal Dynamics of Photon Pairs Generated by an Atomic Ensemble*, Physical Review Letters **93**, 263601 (2004).

[65] D. Felinto, C. W. Chou, H. de Riedmatten, S. V. Polyakov, et al.: *Control of decoherence in the generation of photon pairs from atomic ensembles*, Physical Review A **72**, 053809 (2005).

[66] R. Zhao, Y. O. Dudin, S. D. Jenkins, C. J. Campbell, et al.: *Long-lived quantum memory*, Nature Physics **5**, 100 (2009).

[67] B. Zhao, Y.-A. Chen, X.-H. Bao, T. Strassel, et al.: *A millisecond quantum memory for scalable quantum networks*, Nature Physics **5**, 95 (2009).

[68] S.-J. Yang, X.-J. Wang, X.-H. Bao, and J.-W. Pan: *An efficient quantum light–matter interface with sub-second lifetime*, Nature Photonics **10**, 381 (2016).

[69] G. Heinze, C. Hubrich, and T. Halfmann: *Stopped Light and Image Storage by Electromagnetically Induced Transparency up to the Regime of One Minute*, Physical Review Letters **111**, 033601 (2013).

[70] Y. O. Dudin, L. Li, and A. Kuzmich: *Light storage on the time scale of a minute*, Physical Review A - Atomic, Molecular, and Optical Physics **87**, 1 (2013).

[71] J. Simon, H. Tanji, J. K. Thompson, and V. Vuletić: *Interfacing Collective Atomic Excitations and Single Photons*, Physical Review Letters **98**, 183601 (2007).

[72] X.-H. Bao, A. Reingruber, P. Dietrich, J. Rui, et al.: *Efficient and long-lived quantum memory with cold atoms inside a ring cavity*, Nature Physics **8**, 517 (2012).

[73] E. Bimbard, R. Boddeda, N. Vitrant, A. Grankin, et al.: *Homodyne Tomography of a Single Photon Retrieved on Demand from a Cavity-Enhanced Cold Atom Memory*, Physical Review Letters **112**, 033601 (2014).

[74] Y.-W. Cho, G. T. Campbell, J. L. Everett, J. Bernu, et al.: *Highly efficient optical quantum memory with long coherence time in cold atoms*, Optica **3**, 100 (2016).

[75] Y.-F. Hsiao, P.-J. Tsai, H.-S. Chen, S.-X. Lin, et al.: *Highly Efficient Coherent Optical Memory Based on Electromagnetically Induced Transparency*, Physical Review Letters **120**, 183602 (2018).

[76] P. Vernaz-Gris, K. Huang, M. Cao, A. S. Sheremet, et al.: *Highly-efficient quantum memory for polarization qubits in a spatially-multiplexed cold atomic ensemble*, Nature Communications **9**, 363 (2018).

[77] S. Chen, Y.-A. Chen, B. Zhao, Z.-S. Yuan, et al.: *Demonstration of a Stable Atom-Photon Entanglement Source for Quantum Repeaters*, Physical Review Letters **99**, 180505 (2007).

[78] M. Dąbrowski, M. Parniak, and W. Wasilewski: *Einstein–Podolsky–Rosen paradox in a hybrid bipartite system*, Optica **4**, 272 (2017).

[79] R. Inoue, N. Kanai, T. Yonehara, Y. Miyamoto, et al.: *Entanglement of orbital angular momentum states between an ensemble of cold atoms and a photon*, Physical Review A **74**, 053809 (2006).

[80] Y.-F. Pu, N. Jiang, W. Chang, H.-X. Yang, et al.: *Experimental realization of a multiplexed quantum memory with 225 individually accessible memory cells*, Nature Communications **8**, 15359 (2017).

[81] M. Parniak, M. Dąbrowski, M. Mazelanik, A. Leszczyński, et al.: *Wavevector multiplexed atomic quantum memory via spatially-resolved single-photon detection*, Nature Communications **8**, 2140 (2017).

[82] L. Tian, Z. Xu, L. Chen, W. Ge, et al.: *Spatial Multiplexing of Atom-Photon Entanglement Sources using Feedforward Control and Switching Networks*, Physical Review Letters **119**, 130505 (2017).

[83] J.-P. Dou, A.-l. Yang, M.-Y. Du, D. Lao, et al.: *A Broadband DLCZ Quantum Memory in Room-Temperature Atoms*, arxiv **1704.06309** (2017).

[84] M. Zugenmaier, K. B. Dideriksen, A. S. Sørensen, B. Albrecht, et al.: *Long-lived non-classical correlations for scalable quantum repeaters at room temperature*, arxiv **1801.03286**, 1 (2018).

[85] K. Kutluer, M. Mazzera, and H. de Riedmatten: *Solid-State Source of Nonclassical Photon Pairs with Embedded Multimode Quantum Memory*, Physical Review Letters **118**, 210502 (2017).

[86] C. Laplane, P. Jobez, J. Etesse, N. Gisin, et al.: *Multimode and Long-Lived Quantum Correlations Between Photons and Spins in a Crystal*, Physical Review Letters **118**, 210501 (2017).

[87] R. Riedinger, S. Hong, R. A. Norte, J. A. Slater, et al.: *Non-classical correlations between single photons and phonons from a mechanical oscillator*, Nature **530**, 313 (2016).

[88] K. F. Reim, J. Nunn, V. O. Lorenz, B. J. Sussman, et al.: *Towards high-speed optical quantum memories*, Nature Photonics **4**, 218 (2010).

[89] H. de Riedmatten, M. Afzelius, M. U. Staudt, C. Simon, et al.: *A solid-state light–matter interface at the single-photon level*, Nature **456**, 773 (2008).

[90] M. Gündoğan, P. M. Ledingham, K. Kutluer, M. Mazzera, et al.: *Solid State Spin-Wave Quantum Memory for Time-Bin Qubits*, Physical Review Letters **114**, 230501 (2015).

[91] C. J. Foot: *Atomic physics*, Oxford master series in physics, Oxford University Press (2005).

[92] S. Chu: *Nobel Lecture: The manipulation of neutral particles*, Reviews of Modern Physics **70**, 685 (1998).

[93] C. N. Cohen-Tannoudji: *Nobel Lecture: Manipulating atoms with photons*, Reviews of Modern Physics **70**, 707 (1998).

[94] W. D. Phillips: *Nobel Lecture: Laser cooling and trapping of neutral atoms*, Reviews of Modern Physics **70**, 721 (1998).

[95] B. Albrecht: *Quantum control of single spin excitations in cold atomic quantum memories*, Ph.D. thesis, UPC - Universitat Politècnica de Catalunya (2015).

[96] B. E. A. Saleh and M. C. Teich: *Fundamentals of Photonics*, Wiley Series in Pure and Applied Optics, John Wiley & Sons, Inc., New York, USA (1991).

[97] X. Fernandez-Gonzalvo, G. Corrielli, B. Albrecht, M. Grimau, et al.: *Quantum frequency conversion of quantum memory compatible photons to telecommunication wavelengths*, Optics Express **21**, 19473 (2013).

[98] R. W. Boyd: *Nonlinear Optics, Third Edition*, Academic Press, 3rd ed. (2008).

[99] J. Brendel, N. Gisin, W. Tittel, and H. Zbinden: *Pulsed energy-time entangled twin-photon source for quantum communication*, Phys. Rev. Lett. **82**, 2594 (1999).

[100] I. Marcikic, H. de Riedmatten, W. Tittel, H. Zbinden, et al.: *Distribution of Time-Bin Entangled Qubits over 50 km of Optical Fiber*, Physical Review Letters **93**, 180502 (2004).

[101] P. Farrera, N. Maring, B. Albrecht, G. Heinze, et al.: *Nonclassical correlations between a C-band telecom photon and a stored spin-wave*, Optica **3**, 1019 (2016).

[102] A. I. Lvovsky, B. C. Sanders, and W. Tittel: *Optical quantum memory*, Nature Photonics **3**, 706 (2009).

[103] C. Simon, M. Afzelius, J. Appel, A. Boyer de la Giroday, et al.: *Quantum memories*, The European Physical Journal D **58**, 1 (2010).

[104] F. Bussières, N. Sangouard, M. Afzelius, H. de Riedmatten, et al.: *Prospective applications of optical quantum memories*, Journal of Modern Optics **60**, 1519 (2013).

[105] B. Lauritzen, J. Minář, H. de Riedmatten, M. Afzelius, et al.: *Telecommunication-Wavelength Solid-State Memory at the Single Photon Level*, Physical Review Letters **104**, 80502 (2010).

[106] J. Dajczgewand, J.-L. Le Gouët, A. Louchet-Chauvet, and T. Chanelière: *Large efficiency at telecom wavelength for optical quantum memories*, Optics Letters **39**, 2711 (2014).

[107] C. Simon, H. de Riedmatten, M. Afzelius, N. Sangouard, et al.: *Quantum Repeaters with Photon Pair Sources and Multimode Memories*, Physical Review Letters **98**, 190503 (2007).

[108] D. Rieländer, K. Kutluer, P. M. Ledingham, M. Gündoğan, et al.: *Quantum Storage of Heralded Single Photons in a Praseodymium-Doped Crystal*, Physical Review Letters **112**, 40504 (2014).

[109] F. Bussières, C. Clausen, A. Tiranov, B. Korzh, et al.: *Quantum teleportation from a telecom-wavelength photon to a solid-state quantum memory*, Nature Photonics **8**, 775 (2014).

[110] A. Lenhard, M. Bock, C. Becher, S. Kucera, et al.: *Telecom-heralded single-photon absorption by a single atom*, Physical Review A **92**, 63827 (2015).

[111] G. Schunk, U. Vogl, D. V. Strekalov, M. Förtsch, et al.: *Interfacing transitions of different alkali atoms and telecom bands using one narrowband photon pair source*, Optica **2**, 773 (2015).

[112] W. Zhang, D.-S. Ding, S. Shi, Y. Li, et al.: *Storing a single photon as a spin wave entangled with a flying photon in the telecommunication bandwidth*, Physical Review A **93**, 22316 (2016).

[113] S. Tanzilli, W. Tittel, M. Halder, O. Alibart, et al.: *A photonic quantum information interface*, Nature **437**, 116 (2005).

[114] R. Ikuta, Y. Kusaka, T. Kitano, H. Kato, et al.: *Wide-band quantum interface for visible-to-telecommunication wavelength conversion*, Nature Communications **2**, 1544 (2011).

[115] S. Ates, I. Agha, A. Gulinatti, I. Rech, et al.: *Two-photon interference using background-free quantum frequency conversion of single photons emitted by an InAs quantum dot*, Physical Review Letters **109**, 1 (2012).

[116] R. Ikuta, H. Kato, Y. Kusaka, S. Miki, et al.: *High-fidelity conversion of photonic quantum information to telecommunication wavelength with superconducting single-photon detectors*, Physical Review A **87**, 010301 (2013).

[117] N. Maring, K. Kutluer, J. Cohen, M. Cristiani, et al.: *Storage of upconverted telecom photons in a doped crystal*, New Journal of Physics **16**, 113021 (2014).

[118] F. Kaiser, A. Issautier, L. A. Ngah, D. Aktas, et al.: *Toward Continuous-Wave Regime Teleportation for Light Matter Quantum Relay Stations*, IEEE Journal of Selected Topics in Quantum Electronics **21**, 69 (2015).

[119] P. Sekatski, N. Sangouard, F. Bussières, C. Clausen, et al.: *Detector imperfections in photon-pair source characterization*, Journal of Physics B: Atomic, Molecular and Optical Physics **45**, 124016 (2012).

[120] B. Albrecht, P. Farrera, G. Heinze, M. Cristiani, et al.: *Controlled Rephasing of Single Collective Spin Excitations in a Cold Atomic Quantum Memory*, Physical Review Letters **115**, 160501 (2015).

[121] J. Laurat, K. S. Choi, H. Deng, C. W. Chou, et al.: *Heralded Entanglement between Atomic Ensembles: Preparation, Decoherence, and Scaling*, Physical Review Letters **99**, 180504 (2007).

[122] R. Ikuta, T. Kobayashi, K. Matsuki, S. Miki, et al.: *Heralded single excitation of atomic ensemble via solid-state-based telecom photon detection*, Optica **3**, 1279 (2016).

[123] J. D. Siverns, J. Hannegan, and Q. Quraishi: *Neutral atom wavelength compatible 780 nm single photons from a trapped ion via quantum frequency conversion*, arxiv **1801.01193**, 1 (2018).

[124] T. Walker, K. Miyanishi, R. Ikuta, H. Takahashi, et al.: *Long-Distance Single Photon Transmission from a Trapped Ion via Quantum Frequency Conversion*, Physical Review Letters **120**, 203601 (2018).

[125] R. Ikuta, T. Kobayashi, T. Kawakami, S. Miki, et al.: *Polarization insensitive frequency conversion for an atom-photon entanglement distribution via a telecom network*, Nature Communications **9**, 1997 (2018).

[126] T. A. Wright, R. J. A. Francis-Jones, C. B. E. Gawith, J. N. Becker, et al.: *A two-way quantum interface for linking Sr+ transition at 422nm to the telecommunications C-band*, arxiv **1802.07947** (2018).

[127] P. Farrera, G. Heinze, B. Albrecht, M. Ho, et al.: *Generation of single photons with highly tunable wave shape from a cold atomic ensemble*, Nature Communications **7**, 13556 (2016).

[128] N. Sangouard and H. Zbinden: *What are single photons good for?*, Journal of Modern Optics **59**, 1458 (2012).

[129] M. D. Eisaman, J. Fan, A. Migdall, and S. V. Polyakov: *Invited Review Article: Single-photon sources and detectors*, Review of Scientific Instruments **82**, 071101 (2011).

[130] M. G. Raymer and K. Srinivasan: *Manipulating the color and shape of single photons*, Physics Today **65**, 32 (2012).

[131] S. Bose, K. Jacobs, and P. L. Knight: *Scheme to probe the decoherence of a macroscopic object*, Physical Review A **59**, 3204 (1999).

[132] W. Marshall, C. Simon, R. Penrose, and D. Bouwmeester: *Towards Quantum Superpositions of a Mirror*, Physical Review Letters **91**, 130401 (2003).

[133] P. Sekatski, M. Aspelmeyer, and N. Sangouard: *Macroscopic Optomechanics from Displaced Single-Photon Entanglement*, Physical Review Letters **112**, 080502 (2014).

[134] R. Ghobadi, S. Kumar, B. Pepper, D. Bouwmeester, et al.: *Optomechanical Micro-Macro Entanglement*, Physical Review Letters **112**, 080503 (2014).

[135] M. Aspelmeyer, T. J. Kippenberg, and F. Marquardt: *Cavity optomechanics*, Reviews of Modern Physics **86**, 1391 (2014).

[136] X. H. Bao, Y. Qian, J. Yang, H. Zhang, et al.: *Generation of narrow-band polarization-entangled photon pairs for atomic quantum memories*, Physical Review Letters **101**, 99 (2008).

[137] A. Haase, N. Piro, J. Eschner, and M. W. Mitchell: *Tunable narrow-band entangled photon pair source for resonant single-photon single-atom interaction*, Optics Letters **34**, 55 (2009).

[138] J. Fekete, D. Rieländer, M. Cristiani, and H. de Riedmatten: *Ultranarrow-Band Photon-Pair Source Compatible with Solid State Quantum Memories and Telecommunication Networks*, Physical Review Letters **110**, 220502 (2013).

[139] C. W. Chou, S. V. Polyakov, A. Kuzmich, and H. J. Kimble: *Single-Photon Generation from Stored Excitation in an Atomic Ensemble*, Physical Review Letters **92**, 213601 (2004).

[140] J. Laurat, H. de Riedmatten, D. Felinto, C.-W. Chou, et al.: *Efficient retrieval of a single excitation stored in an atomic ensemble*, Optics Express **14**, 6912 (2006).

[141] J. K. Thompson, J. Simon, H. Loh, and V. Vuletić: *A High-Brightness Source of Narrowband, Identical-Photon Pairs*, Science **313**, 74 (2006).

[142] D. N. Matsukevich, T. Chanelière, S. D. Jenkins, S.-Y. Lan, et al.: *Deterministic Single Photons via Conditional Quantum Evolution*, Physical Review Letters **97**, 013601 (2006).

[143] S. Chen, Y.-A. Chen, T. Strassel, Z.-S. Yuan, et al.: *Deterministic and Storable Single-Photon Source Based on a Quantum Memory*, Physical Review Letters **97**, 173004 (2006).

[144] S. Du, P. Kolchin, C. Belthangady, G. Y. Yin, et al.: *Subnatural Linewidth Biphotons with Controllable Temporal Length*, Physical Review Letters **100**, 183603 (2008).

[145] B. Srivathsan, G. K. Gulati, B. Chng, G. Maslennikov, et al.: *Narrow Band Source of Transform-Limited Photon Pairs via Four-Wave Mixing in a Cold Atomic Ensemble*, Physical Review Letters **111**, 123602 (2013).

[146] L. Zhao, X. Guo, C. Liu, Y. Sun, et al.: *Photon pairs with coherence time exceeding 1 μs*, Optica **1**, 84 (2014).

[147] J. McKeever, A. Boca, A. D. Boozer, R. Miller, et al.: *Deterministic Generation of Single Photons from One Atom Trapped in a Cavity*, Science **303**, 1992 LP (2004).

[148] M. Hijlkema, B. Weber, H. P. Specht, S. C. Webster, et al.: *A single-photon server with just one atom*, Nature Physics **3**, 253 (2007).

[149] C. Matthiesen, A. N. Vamivakas, and M. Atatüre: *Subnatural Linewidth Single Photons from a Quantum Dot*, Physical Review Letters **108**, 093602 (2012).

[150] M. Almendros, J. Huwer, N. Piro, F. Rohde, et al.: *Bandwidth-Tunable Single-Photon Source in an Ion-Trap Quantum Network*, Physical Review Letters **103**, 213601 (2009).

[151] M. D. Eisaman, L. Childress, A. André, F. Massou, et al.: *Shaping Quantum Pulses of Light Via Coherent Atomic Memory*, Physical Review Letters **93**, 233602 (2004).

[152] M. Keller, B. Lange, K. Hayasaka, W. Lange, et al.: *Continuous generation of single photons with controlled waveform in an ion-trap cavity system*, Nature **431**, 1075 (2004).

[153] V. Balić, D. A. Braje, P. Kolchin, G. Y. Yin, et al.: *Generation of Paired Photons with Controllable Waveforms*, Physical Review Letters **94**, 183601 (2005).

[154] P. B. R. Nisbet-Jones, J. Dilley, D. Ljunggren, and A. Kuhn: *Highly efficient source for indistinguishable single photons of controlled shape*, New Journal of Physics **13**, 103036 (2011).

[155] C. Matthiesen, M. Geller, C. H. H. Schulte, C. Le Gall, et al.: *Phase-locked indistinguishable photons with synthesized waveforms from a solid-state source*, Nature Communications **4**, 1600 (2013).

[156] L. Zhao, X. Guo, Y. Sun, Y. Su, et al.: *Shaping the Biphoton Temporal Waveform with Spatial Light Modulation*, Physical Review Letters **115**, 193601 (2015).

[157] S. A. Aljunid, G. Maslennikov, Y. Wang, H. L. Dao, et al.: *Excitation of a Single Atom with Exponentially Rising Light Pulses*, Physical Review Letters **111**, 103001 (2013).

[158] C. Liu, Y. Sun, L. Zhao, S. Zhang, et al.: *Efficiently Loading a Single Photon into a Single-Sided Fabry-Perot Cavity*, Physical Review Letters **113**, 133601 (2014).

[159] J. Nunn: *Enhancing multiphoton rates with quantum memories*, Phys. Rev. Lett. **110**, 133601 (2013).

[160] R. A. de Oliveira: *Single-photon superradiance in cold atoms*, Phys. Rev. A. **90**, 23848 (2014).

[161] A. André: *No Title*, Nonclassical States Of Light And Atomic Ensembles: Generation And New Applications (2005).

[162] P. Grangier, G. Roger, and A. Aspect: *Experimental Evidence for a Photon Anticorrelation Effect on a Beam Splitter: A New Light on Single-Photon Interferences*, Europhysics Letters (EPL) **1**, 173 (1986).

[163] A. Christ, K. Laiho, A. Eckstein, K. N. Cassemiro, et al.: *Probing multimode squeezing with correlation functions*, New. J. Phys. **13**, 33027 (2011).

[164] M. Stobińska, G. Alber, and G. Leuchs: *Perfect excitation of a matter qubit by a single photon in free space*, Europhys. Lett. **86**, 14007 (2009).

[165] M. Bader, S. Heugel, A. L. Chekhov, M. Sondermann, et al.: *Efficient coupling to an optical resonator by exploiting time-reversal symmetry*, New. J. Phys. **15**, 123008 (2013).

[166] I. Marcikic, H. de Riedmatten, W. Tittel, V. Scarani, et al.: *Time-bin entangled qubits for quantum communication created by femtosecond pulses*, Physical Review A **66**, 62308 (2002).

[167] D. Felinto: *Conditional control of the quantum states of remote atomic memories for quantum networking*, Nat. Phys. **2**, 844 (2006).

[168] Z.-S. Yuan: *Synchronized independent narrow-band single photons and efficient generation of photonic entanglement*, Phys. Rev. Lett. **98**, 180503 (2007).

[169] H. J. Kimble: *The quantum internet*, Nature **453**, 1023 (2008).

[170] P. Farrera, G. Heinze, and H. de Riedmatten: *Entanglement between a Photonic Time-Bin Qubit and a Collective Atomic Spin Excitation*, Physical Review Letters **120**, 100501 (2018).

[171] J. F. Sherson, H. Krauter, R. K. Olsson, B. Julsgaard, et al.: *Quantum teleportation between light and matter*, Nature **443**, 557 (2006).

[172] J. Hofmann: *Heralded entanglement between widely separated atoms*, Science **337**, 72 (2012).

[173] I. Marcikic, H. de Riedmatten, W. Tittel, H. Zbinden, et al.: *Long-distance teleportation of qubits at telecommunication wavelengths*, Nature **421**, 509 (2003).

[174] R. Valivarthi, M. G. Puigibert, Q. Zhou, G. H. Aguilar, et al.: *Quantum teleportation across a metropolitan fibre network*, Nature Photonics **10**, 676 (2016).

[175] Q.-C. Sun, Y.-L. Mao, S.-J. Chen, W. Zhang, et al.: *Quantum teleportation with independent sources and prior entanglement distribution over a network*, Nature Photonics **10**, 671 (2016).

[176] Y. Jiang, J. Rui, X.-H. Bao, and J.-W. Pan: *Dynamical zeroing of spin-wave momentum to suppress motional dephasing in an atomic-ensemble quantum memory*, Physical Review A **93**, 063819 (2016).

[177] J. F. Clauser, M. A. Horne, A. Shimony, and R. A. Holt: *Proposed Experiment to Test Local Hidden-Variable Theories*, Physical Review Letters **23**, 880 (1969).

[178] The BIG Bell Test Collaboration: *Challenging local realism with human choices*, Nature **557**, 212 (2018).

[179] A. Peres: *Separability Criterion for Density Matrices*, Physical Review Letters **77**, 1413 (1996).

[180] F. Vedovato, C. Agnesi, M. Tomasin, M. Avesani, et al.: *Post-selection-loophole-free Bell violation with genuine time-bin entanglement*, arxiv **1804.10150** (2018).

[181] G. Lima, G. Vallone, A. Chiuri, A. Cabello, et al.: *Experimental Bell-inequality violation without the postselection loophole*, Physical Review A **81**, 040101 (2010).

[182] A. Cuevas, G. Carvacho, G. Saavedra, J. Cariñe, et al.: *Long-distance distribution of genuine energy-time entanglement*, Nature Communications **4**, 1 (2013).

[183] N. Maring, P. Farrera, K. Kutluer, M. Mazzera, et al.: *Photonic quantum state transfer between a cold atomic gas and a crystal*, Nature **551**, 485 (2017).

[184] E. Distante, P. Farrera, A. Padrón-Brito, D. Paredes-Barato, et al.: *Storing single photons emitted by a quantum memory on a highly excited Rydberg state*, Nature Communications **8**, 14072 (2017).

[185] B. Dayan: *Regulated by one atom*, Science **319**, 22 (2008).

[186] A. Reiserer, S. Ritter, and G. Rempe: *Nondestructive detection of an optical photon*, Science **342**, 1349 (2013).

[187] A. Reiserer, N. Kalb, G. Rempe, and S. Ritter: *A quantum gate between a flying optical photon and a single trapped atom*, Nature **508**, 237 (2014).

[188] I. Shomroni: *All-optical routing of single photons by a one-atom switch controlled by a single photon*, Science **345**, 903 (2014).

[189] W. Chen: *All-optical switch and transistor gated by one stored photon*, Science **341**, 768 (2013).

[190] I. Fushman: *Controlled phase shifts with a single quantum dot*, Science **320**, 769 (2008).

[191] T. Volz: *Ultrafast all-optical switching by single photons*, Nat. Photon. **6**, 607 (2012).

[192] N. Piro: *Heralded single-photon absorption by a single atom*, Nat. Phys. **7**, 17 (2010).

[193] T. Guerreiro, A. Martin, B. Sanguinetti, J. S. Pelc, et al.: *Nonlinear Interaction between Single Photons*, Physical Review Letters **113**, 173601 (2014).

[194] T. Peyronel: *Quantum nonlinear optics with single photons enabled by strongly interacting atoms*, Nature **488**, 57 (2012).

[195] Y. O. Dudin and A. Kuzmich: *Strongly Interacting Rydberg Excitations of a Cold Atomic Gas*, Science **336**, 887 (2012).

[196] Y. O. Dudin, L. Li, F. Bariani, and A. Kuzmich: *Observation of coherent many-body Rabi oscillations*, Nat. Phys. **8**, 790 (2012).

[197] O. Firstenberg, T. Peyronel, Q.-Y. Liang, A. V. Gorshkov, et al.: *Attractive photons in a quantum nonlinear medium*, Nature **502**, 71 (2013).

[198] D. Maxwell, D. J. Szwer, D. Paredes-Barato, H. Busche, et al.: *Storage and Control of Optical Photons Using Rydberg Polaritons*, Physical Review Letters **110**, 103001 (2013).

[199] D. Tiarks, S. Baur, K. Schneider, S. Dürr, et al.: *Single-Photon Transistor Using a Förster Resonance*, Physical Review Letters **113**, 053602 (2014).

[200] S. Baur, D. Tiarks, G. Rempe, and S. Dürr: *Single-Photon Switch Based on Rydberg Blockade*, Physical Review Letters **112**, 073901 (2014).

[201] H. Gorniaczyk, C. Tresp, J. Schmidt, H. Fedder, et al.: *Single-Photon Transistor Mediated by Interstate Rydberg Interactions*, Physical Review Letters **113**, 053601 (2014).

[202] L. Li, Y. O. Dudin, and A. Kuzmich: *Entanglement between light and an optical atomic excitation*, Nature **498**, 466 (2013).

[203] D. Paredes-Barato and C. S. Adams: *All-optical quantum information processing using rydberg gates*, Phys. Rev. Lett. **112**, 40501 (2014).

[204] M. Khazali, K. Heshami, and C. Simon: *Photon-photon gate via the interaction between two collective Rydberg excitations*, Phys. Rev. A **91**, 30301 (2015).

[205] E. Distante: *Storage and retrieval of a single photon emitted by a quantum memory on a highly excited Rydberg state*, Zenodo, (2016).

[206] T. Chanelière: *Storage and retrieval of single photons transmitted between remote quantum memories*, Nature **438**, 833 (2005).

[207] M. D. Eisaman: *Electromagnetically induced transparency with tunable single-photon pulses*, Nature **438**, 837 (2005).

[208] K. S. Choi: *Mapping photonic entanglement into and out of a quantum memory*, Nature **452**, 67 (2008).

[209] S. Zhou: *Optimal storage and retrieval of single-photon waveforms*, Opt. Express **20**, 24124 (2012).

[210] D. S. Ding, K. Wang, W. Zhang, S. Shi, et al.: *Entanglement between low- and high-lying atomic spin waves*, Physical Review A **94**, 052326 (2016).

[211] M. Fleischhauer and M. D. Lukin: *Dark-state polaritons in electromagnetically induced transparency*, Phys. Rev. Lett. **84**, 5094 (2000).

[212] M. Fleischhauer and M. D. Lukin: *Quantum memory for photons: Dark-state polaritons*, Phys. Rev. A **65**, 22314 (2002).

[213] M. Fleischhauer, A. Imamoglu, and J. P. Marangos: *Electromagnetically induced transparency: Optics in coherent media*, Rev. Mod. Phys. **77**, 633 (2005).

[214] C. Liu, Z. Dutton, C. H. Behroozi, and L. V. Hau: *Observation of coherent optical information storage in an atomic medium using halted light pulses*, Nature **409**, 490 (2001).

[215] D. Wei: *Optical Precursors with Electromagnetically Induced Transparency in Cold Atoms*, Phys. Rev. Lett. **103**, 93602 (2009).

[216] S. Zhang: *Optical precursor of a single photon*, Phys. Rev. Lett. **106**, 243602 (2011).

[217] Z.-L. Xiang, S. Ashhab, J. Q. You, and F. Nori: *Hybrid quantum circuits: Superconducting circuits interacting with other quantum systems*, Reviews of Modern Physics **85**, 623 (2013).

[218] T. R. Tan: *Multi-element logic gates for trapped-ion qubits*, Nature **528**, 380 (2015).

[219] C. J. Ballance: *Hybrid quantum logic and a test of Bell's inequality using two different atomic isotopes*, Nature **528**, 384 (2015).

[220] N. Akopian, L. Wang, A. Rastelli, O. G. Schmidt, et al.: *Hybrid semiconductor-atomic interface: slowing down single photons from a quantum dot*, Nat. Photon. **5**, 230 (2011).

[221] P. Siyushev, G. Stein, J. Wrachtrup, and I. Gerhardt: *Molecular photons interfaced with alkali atoms*, Nature **509**, 66 (2014).

[222] H. M. Meyer: *Direct photonic coupling of a semiconductor quantum dot and a trapped ion*, Phys. Rev. Lett. **114**, 123001 (2015).

[223] J.-S. Tang: *Storage of multiple single-photon pulses emitted from a quantum dot in a solid-state quantum memory*, Nat. Commun. **6**, 8652 (2015).

[224] M. Saffman, T. G. Walker, and K. Mølmer: *Quantum information with Rydberg atoms*, Rev. Mod. Phys. **82**, 2313 (2010).

[225] M. P. Hedges, J. J. Longdell, Y. Li, and M. J. Sellars: *Efficient quantum memory for light*, Nature **465**, 1052 (2010).

[226] K. R. Ferguson, S. E. Beavan, J. J. Longdell, and M. J. Sellars: *Generation of light with multimode time-delayed entanglement using storage in a solid-state spin-wave quantum memory*, Phys. Rev. Lett. **117**, 20501 (2016).

[227] A. Seri, A. Lenhard, D. Rieländer, M. Gündoğan, et al.: *Quantum Correlations between Single Telecom Photons and a Multimode On-Demand Solid-State Quantum Memory*, Physical Review X **7**, 021028 (2017).

[228] S. Massar and S. Popescu: *Optimal extraction of information from finite quantum ensembles*, Phys. Rev. Lett. **74**, 1259 (1995).

[229] R. Loudon: *The quantum theory of light / Rodney Loudon*, Clarendon Press, Oxford (1973).

[230] B. Zhao: *Robust and Efficient Quantum Repeater with Atomic Ensembles and Linear Optics*, Ph.D. thesis, University of Heidelberg (2008).

[231] J. Minář, H. de Riedmatten, C. Simon, H. Zbinden, et al.: *Phase-noise measurements in long-fiber interferometers for quantum-repeater applications*, Physical Review A **77**, 052325 (2008).

[232] M. Ho, C. Teo, H. de Riedmatten, and N. Sangouard: *Optimal Photon Generation from Spontaneous Raman Processes in Cold Atoms*, arxiv **1707.03353** (2017).

[233] M. S. Mendes, P. L. Saldanha, J. W. R. Tabosa, and D. Felinto: *Dynamics of the reading process of a quantum memory*, New Journal of Physics **15**, 075030 (2013).

[234] J. S. Bell: *On the Einstein Podolsky Rosen paradox* (1964).

[235] S. Barnett: *Quantum Information*, Oxford University Press, Inc., New York, NY, USA (2009).